




12-2022

## Natural, Experimental, and Educational Explorations of the Interiors of Terrestrial Planetary Bodies

Nadine L. Grambling

*University of Tennessee, Knoxville, ngrambli@vols.utk.edu*

Follow this and additional works at: [https://trace.tennessee.edu/utk\\_graddiss](https://trace.tennessee.edu/utk_graddiss)

 Part of the [Curriculum and Instruction Commons](#), [Geochemistry Commons](#), [Geology Commons](#), [Mineral Physics Commons](#), [Science and Mathematics Education Commons](#), [Secondary Education Commons](#), [Tectonics and Structure Commons](#), and the [Volcanology Commons](#)

---

### Recommended Citation

Grambling, Nadine L., "Natural, Experimental, and Educational Explorations of the Interiors of Terrestrial Planetary Bodies." PhD diss., University of Tennessee, 2022.  
[https://trace.tennessee.edu/utk\\_graddiss/7708](https://trace.tennessee.edu/utk_graddiss/7708)

This Dissertation is brought to you for free and open access by the Graduate School at TRACE: Tennessee Research and Creative Exchange. It has been accepted for inclusion in Doctoral Dissertations by an authorized administrator of TRACE: Tennessee Research and Creative Exchange. For more information, please contact [trace@utk.edu](mailto:trace@utk.edu).

To the Graduate Council:

I am submitting herewith a dissertation written by Nadine L. Grambling entitled "Natural, Experimental, and Educational Explorations of the Interiors of Terrestrial Planetary Bodies." I have examined the final electronic copy of this dissertation for form and content and recommend that it be accepted in partial fulfillment of the requirements for the degree of Doctor of Philosophy, with a major in Geology.

Nicholas J. Dygert, Major Professor

We have read this dissertation and recommend its acceptance:

Molly C. McCanta, William M. Dunne, Emily J. Chin

Accepted for the Council:

Dixie L. Thompson

Vice Provost and Dean of the Graduate School

(Original signatures are on file with official student records.)

**Natural, Experimental, and Educational Explorations of the Interiors of  
Terrestrial Planetary Bodies**

**A Dissertation Presented for the  
Doctor of Philosophy  
Degree  
The University of Tennessee, Knoxville**

**Nadine Lynne Grambling  
August 2022**

**Copyright © 2022 by Nadine Lynne Grambling  
All rights reserved.**

## **DEDICATION**

This is dedicated to my feline army, Rock, Boston, Mickey, Marshmallow, Linus, Albert, Voltaire and Watson, my brother, Max, my husband, Tyler, and my parents, Jim and Lisa. Thank you all for your love and support.

## ACKNOWLEDGEMENTS

I owe a great deal of gratitude to many members of the geology community outside of my home institution, including Greg Hirth, Yan Liang, Cameron Meyers, Leif Tokle, Eric Burdette, and Ningli Zhao at the Brown University Rock Deformation Lab for assistance with Griggs Apparatus experiments and endless encouragement, good spirits, and conversations on rock mechanics, John Wakabayashi, who provided a wealth of knowledge on ophiolite formation and brewing processes, my science party cohort on the Chikyu D/V during core description and sampling for Chapter 1, Peter Kelemen, who has been instrumental in my work on fast-spreading ridges, Ruth Aronoff, for inspiration and guidance in surviving the process, Karl Karlstrom, my thesis advisor at UNM, for teaching me how to disagree in the sciences through the great battle over the Grand Canyon, and Julio Betancourt, for his support and encouragement of my early scientific research potential.

On the home front I would like to thank my advisor, Nick Dygert for facilitating this work through external funding and grants, my committee members for their insight and guidance, especially Emily Chin for hosting me during my visit to Scripps and assistance collecting EBSD data and Bill Dunne for his flexibility as a late-stage addition to my committee, Micah Jessup, for allowing me to tag along on international field campaigns in the high Andes, and his contributions to my growth as a structural geologist. I have benefited a great deal from the mentorship of two fantastic educators within my department, Stephanie Drumheller and Robert Jacobsen, who have encouraged my development as teacher and human. To the administrative staff of EPS, Diane Pealor, Melody Branch, Teresa Parrott, Marie Ballard and Angie Staley for all of their support and assistance.

And where would I be without my peers during this process? I want to thank Beau Boring for her assistance in collecting microprobe data and helping maintain my sanity throughout my time in Tennessee (and Providence). I would especially like to acknowledge Claire Mondro, Sam Gwizd, Helle Skjetne, Kaitlyn Gauvey and Kristan Watkins for their friendships over the past 4+ years. To Allison Rogers and Rhianna

Moore, thank you for 2 great years of GeoClub e-board. Jesse Scholpp, Megan Mouser, Dian Ji and Mike Lucas have provided great insight as group members of the EMPG.

To the coaches, SAs, and fellow 7:10AM-ers of OTFBearden, I may not have kept my sanity without the orange lights, Satan's Skateboard, and sprints to the finish.

A warm shout out to the Warnekes, née Warnekes, Parras and Gramblings near and far, especially Steven, and Madeline, for providing distraction and a place to stay during multiple deployments to New England. I cannot thank my parents enough for their endless support, even though they had to visit the South, and my brother Max for serving as our ward during the COVID-19 pandemic.

Finally, I would like to thank my husband, Tyler, for his over-confidence in my ability to survive this ordeal, for watching the cats as I spent months traveling domestically and internationally for research, for his acceptance of my "quirks" both diagnosed and otherwise and for dragging me to the home of the Wigsphere to experience 5 years of humidity beyond our wildest imagination.

## ABSTRACT

Planetary interiors are enigmatic, inaccessible, and vital to the processes that have formed the rocks we see on the surface of bodies in the inner Solar System today. Based on geophysical explorations of the Moon and Earth, along with information gleaned from rocks at the surface today, there is understanding of the basic structure and processes at depth. Using a combination of natural samples and experimental studies, we attempt to learn more about the physical conditions beneath the surface, and their effect on material properties and tectonics processes in the mantle.

On Earth, mid-ocean ridge processes have long been debated, and there has been little consensus on the magmatic plumbing and extent of ocean-water circulation at depth, leaving a debate between two end-member models of crustal accretion. Using geothermometry and geospeedometry of lower-crustal and upper-mantle rocks from a paleo-ridge in the Samail Ophiolite, alongside a similar suite of rocks from the actively spreading East Pacific Rise at Hess Deep, we compare the thermal structure of the crust-mantle transition zone and implications for the on-axis processes that form much of the Earth's crust.

Past work has constrained the crystallization sequence of the moon through time and determined one of the last layers to crystallize was highly dense, containing a significant fraction of the mineral ilmenite, and initially formed above the less-dense mantle cumulate pile, composed mainly of mafic minerals. To study the possible interactions of these two layers due to the density instability, I completed shear deformation experiments on ilmenite and olivine aggregates, in equilibrium, to compare to aggregate flow laws proposed for phase mixing and determine the system rheology.

To introduce high school students in East Tennessee to the concept of mantle materials and conditions versus crustal materials and their formation conditions, I have created an activity and corresponding lesson plan for use in secondary school Chemistry classrooms. This activity combines phase diagrams, physical models of chemical bonds, and a comparison of two native minerals with the same chemical formula to help students think about the effects of pressure and temperature on Earth materials.



# TABLE OF CONTENTS

Introduction .....	1
Chapter 1: Thermal history of lithosphere formed beneath fast spreading ridges: Constraints from the Mantle Transition Zone of the East Pacific Rise at Hess Deep and Oman Drilling Project, Wadi Zeeb, Samail ophiolite .....	3
Abstract .....	4
1. Introduction .....	5
1.0.1 Crustal Accretion models .....	8
1.0.2 Results from previous investigations that constrained cooling rate variations in oceanic lithosphere .....	9
1.1 Study Areas.....	11
1.1.1 Wadi Zeeb, Oman ophiolite, as sampled by the Oman Drilling Project .....	12
1.1.2 Hess Deep .....	13
2. Sample Description.....	13
2.1 Samples .....	13
3. Analytical Methods.....	17
3.1 Major Element Analysis.....	17
3.2 Trace Element Analysis .....	18
4. Analytical and Thermometric Results .....	18
4.1 Major elements.....	18
4.1.1 Major element zonation .....	21
4.2 Trace elements .....	22
4.2.2 Trace element zoning.....	24
4.3 Temperatures .....	24
5. Discussion .....	33
5.1 Significance of temperatures.....	33
5.1.1 Hess Deep gabbros may not record meaningful cooling rates.....	34
5.1.2 Some peridotites may not provide a record of cooling from peak temperatures .....	35
5.2 <i>Cooling Rates</i> .....	36
5.2.1 Rates from Ca-in-olivine temperatures.....	37
5.2.2 Rates from REE-in-two-pyroxene temperatures and pyroxene solvus temperatures .....	37
5.2.3 Rates from REE-in-clinopyroxene-plagioclase temperatures and Mg-in- plagioclase temperatures .....	40
5.3 Implications for cooling and crustal accretion mechanisms.....	41
5.4 Comparison with previous thermometric investigations .....	43
6. Summary and Conclusions .....	46
7. Acknowledgments, Samples, and Data .....	48
References .....	49
Appendix.....	61
<i>Appendix 1. Supplemental Figures</i> .....	61
Appendix 1 References .....	64

Chapter 2: Microstructural Investigation of Ilmenite-Olivine Aggregates Deformed in Shear.....	65
Abstract .....	66
1. Introduction.....	66
2. Experimental Design and Methods.....	68
2.1 Starting Materials .....	68
2.2 Experimental Conditions .....	70
3. Analytical Methods.....	70
3.1 Electron Backscatter Diffraction .....	73
4. Mechanical Data and Analytical Results.....	73
4.1 Mechanical Data .....	73
4.1.1 Dormant Rig complications in runs from July 2021 and January 2022.....	75
4.1.2 Correcting for fast run-ins.....	75
4.2 Microstructures.....	75
5. Discussion .....	77
5.1 Flow Law .....	77
5.1.1 Olivine Flow Laws .....	77
5.1.2 Ilmenite Flow Laws.....	80
5.2 Stress and strain comparisons to published flow laws .....	80
5.2.1 Uncertainty in water content of experimental materials.....	82
5.2.2 Anomalous strength/weakness in 25% ilm40:75% SCO samples not reproducible .....	83
5.3 Post-deformation fabrics .....	83
5.3.1 Olivine .....	83
5.3.2 Ilmenite.....	84
6. Summary and Conclusions.....	85
7. Acknowledgments, Samples, and Data .....	86
References .....	87
Appendix.....	91
<i>Appendix 1. Supplemental Figure</i> .....	91
Chapter 3: Building Carbon minerals: Application of geoscience learning materials to the Tennessee Academic Standards for Science for Chemistry I for use in public school classrooms .....	92
Abstract .....	93
1. Introduction.....	93
2. Background .....	94
3. Layering the Earth .....	96
4. Carbon: Phases with Relation to Earth .....	99
5. Hands On: Molecular Models of Solid Phases of Elemental Carbon .....	105
6. Lesson Wrap-Up: Same Element, Same Phase, Different Structure .....	105
References .....	109
Conclusions.....	110
Vita.....	111

## LIST OF TABLES

Table 1.1. Samples and sampling locations. ....	14
Table 1.2. Temperatures. ....	27
Table 2.1 Sample information by experiment in order of first run to last run. ....	71
Table 2.2. Notes on variations in experimental run conditions. ....	72
Table 2.3. Sample results from mechanical data and EBSD analysis data processing. ....	78
Table 3.1. Standards relevant to "Building Carbon Minerals" lesson plan.....	95
Table 3.2. Layers of the Earth, depths from the surface, and their major mineralogy. ...	98
Table 3.3. Pressure and temperature at different locations within the Earth with distance from the center of Earth and distance from the surface of Earth. ....	101
Table 3.4. Possible discussion questions for different portions of classroom activity, with important discussion points listed in the right column. ....	103
Table 3.5. Information on parts per set for group classroom activity based on Indigo Instruments molecular models. ....	106

## LIST OF FIGURES

- Figure 1.1. Schematic illustrating end-member crustal accretion models. (a) The Gabbro Glacier model (e.g. Henstock et al., 1993; Phipps Morgan & Chen, 1993; Quick & Denlinger, 1993; Sinton & Detrick, 1992; Sleep, 1975); (b) the Sheeted Sills model (e.g. Kelemen, Hirth, et al., 1997; Kelemen, Koga, et al., 1997; Korenaga & Kelemen, 1997; VanTongeren et al., 2008, 2015). The Gabbro Glacier model posits that the lower section of crust is formed accretion of by a large zone of crystalline mush, which accumulates beneath an axial magma lens at the base of the upper crustal dikes. In this model, cooling of the entire lower crustal section and underlying mantle is purely conductive, through heat lost to the hydrothermally cooled extrusive section (basalts and dikes). (b) The Sheeted Sills model assumes similar crustal accretion in the extrusive section (basalts and dikes) but diverges from the gabbro glacier model in the lower crust. In this model, the lower crust is formed from the injection of a multitude of magmatic sills at a range of depths beneath an axial magma lens at the base of the extrusive section. Deep and vigorous hydrothermal circulation through the entire crustal section (through networks of fractures) is required to accommodate heat released by solidification of the sills, which necessarily produces fast cooling rates in the entire lower crustal section and uppermost part of the mantle section..... 6
- Figure 1.2. Representative cross polarized light and backscatter electron photomicrographs of samples from Hess Deep and Oman Drilling Project (left and right columns, respectively). (a) is a crustal gabbro from site 1415G, IODP Expedition 345 and (b) and (c) are upper mantle peridotites from hole 895D of ODP Leg 147. (d) is a crustal gabbro from hole CM1 and (e) and (f) are peridotites from the crust-mantle transition of hole CM2. Red spots in (a) correspond to LA-ICP-MS spot numbers shown in Figure 1.5. According to petrographic observation and modal mineralogy (Table 1.3), clinopyroxenes interpreted to be residual are shown in the middle row; the bottom row (c), (f) shows samples with minor clinopyroxene that may have exsolved at subsolidus temperatures, and/or crystallized from melt present during cooling..... 16
- Figure 1.3. Variations in major element compositions of minerals in samples from this study (averages) and the literature. Gabbros are shown in the first row (a, b) and peridotites are shown in the second and third rows (c-f). Samples from this study are shown as orange diamonds (Hess Deep) and purple squares (OmanDP). Ophiolitic gabbros and peridotites from petDB and Dygert et al., 2017, are shown as gray and blue dots, respectively, and abyssal peridotites from Warren, 2016, are shown as gray dots. MgO in plagioclase data shown in (a) and used in thermometric interpretations (this study) were collected by LA-ICP-MS. We note MgO concentrations in the literature data shown in (a) may not have been collected under optimized analytical conditions, perhaps accounting for some of the scatter. .... 19
- Figure 1.4. Chondrite normalized REE+Y abundances in minerals from the crust and mantle sections of Oman Drilling Project (a) and Hess Deep (b). Individual spot analyses are shown in gray in the background, and sample averages are shown as

thicker colored lines, error bars are  $1\sigma$  standard deviations of replicate analyses for each sample. Minerals in crustal samples are green (plagioclase) and red (clinopyroxene), minerals in peridotites are magenta (clinopyroxene) and blue (orthopyroxene)..... 23

Figure 1.5. Ce and Nd concentrations in paired plagioclase and clinopyroxene grains measured by LA-ICP-MS. Analytical uncertainty (relative) is estimated at 10% of the concentration. Trace element abundances vary beyond the analytical uncertainty in the plagioclase grain on the left and in the clinopyroxene. These variations are representative of Hess Deep gabbros in general, and the variations are interpreted to reflect magmatic processes. See Section 5.1.1 and Lissenberg et al., 2013, and Lissenberg & Macleod, 2016. .... 25

Figure 1.6. Temperature comparison for samples from the Oman Drilling Project (a) and Hess Deep (b) above and below the petrologic Moho, which is indicated by the horizontal red line. In order to compare trends between drilling sites, samples are shown in relational depth, not absolute distance, as Hess Deep peridotites and gabbros cannot be directly related in stratigraphic depth owing to uncertainty in the local structure. For all samples, depths within the holes are reported in Table 1.1. Structural depths of the Oman Drilling Project samples are reported in Table 1.1 and are presented graphically in Figures 1.9 & 1.10. Hess Deep samples are schematically plotted relative to the Moho in Figures 1.9 & 1.10..... 28

Figure 1.7. Temperatures obtained in this study compared to other localities in Oman, previous work on Hess Deep and the global distribution of ophiolites and abyssal peridotites. (a)  $T_{REE-in-Plag-Cpx}$  vs.  $T_{Mg-in-Plag}$  (gabbros), (b)  $T_{REE-in-two-Pyroxene}$  vs.  $T_{BKN}$  (peridotites); (c)  $T_{Ca-in-OI}$  vs.  $T_{OI-Sp}$  (peridotites). Temperatures obtained for gabbros are consistent with but at the high temperature end of previous work on Hess Deep (a). Note that samples from this study have high  $T_{REE}$  and  $T_{BKN}$ , consistent with abyssal peridotites and some samples from Oman (b). Peridotite temperatures obtained using fast-resetting thermometers (Ca-in-Olivine and Olivine-Spinel) are at the high end of the global distribution of ophiolites (c), perhaps owing to the close proximity of the samples from this study to the transition zone compared to other ophiolitic peridotites. Data sources are the following: Wadi Tayin, Dygert et al., 2017; Elsewhere Oman (Wadi Fizh, Wadi Thuqbah, Wadi Rajmi, and Wadi Sarami in central and northern Oman; Akizawa et al., 2012, 2016); Other ophiolites, Dygert et al., 2015; Abyssal peridotites, Dygert et al., 2017; Hess Deep, Sun and Lissenberg, 2018..... 30

Figure 1.8. Temperatures for Hess Deep and Oman Drilling Project (OmanDP) peridotites compared to models for closure temperature calculated as a function of cooling rate (grid composed of black and magenta lines). (a) Shows samples from this study with colored symbols are interpreted to have retained residual clinopyroxene throughout partial melting, those with gray symbols are interpreted to have exsolved from orthopyroxene under subsolidus conditions, or crystallized from melt during cooling, and thus may not record cooling rates from peak temperatures. The cooling rate grid was calculated utilizing a modified form of the Dodson equation assuming a radius of 0.5 mm (Ganguly & Tirone, 1999, see Dygert & Liang, 2015, for details). The 1:1 line, shown in blue, represents equal

temperatures for the two thermometers. Initial temperatures ( $T_0$ ) represent the peak temperatures from which samples cooled, the paths samples take in this temperature space are indicated by the magenta lines extending from initial temperatures along the blue 1:1 line. The near-vertical black lines represent cooling rates in °C/year. Assuming an effective grain radius of 0.5 mm, all samples in this study cooled at rates of 0.3°C/year or faster. Cooling rates calculated using the measured, sample specific grain sizes from samples with residual clinopyroxene are reported in Table 1.3 and shown in Figure 1.9 (blue symbols). (b) Shows samples from (a) with residual clinopyroxene from this study, alongside published samples from Dygert et al., 2017, with structural depths of samples beneath the crust-mantle transition indicated (meters). The question mark indicates that the structural depth of Hess Deep peridotites relative to crust-mantle transition is unknown..... 32

Figure 1.9. Comparison between cooling rates obtained from samples in this study (green, magenta and blue diamonds and squares) and modeled conductive cooling rates for three temperature intervals (red, blue and green lines, 1200-900°C, 1000-700°C, and 750-600°C, respectively). Insets show cartoons reflecting the relevant crustal accretion mechanism and cooling regime assumed for each panel. A Gabbro Glacier scenario is shown in (a), with conductive cooling starting at the dike-gabbro transition, beneath which hydrothermal circulation does not extend. A hydrothermal model from Maclennan et al., 2005, is shown for comparison, which assumes a thinner extrusive section and lower thermal diffusivity compared to models from this study. A Sheeted Sills scenario is shown in (b), which assumes convective cooling by hydrothermal circulation throughout the entire crustal column, and conductive cooling beneath the Moho. The sample-based cooling rates obtained in this study are shown at their approximate depths relative to the Moho, and are the same in both panels. Note the sample-based cooling rates obtained from three independent thermometric and geospeedometric methods (Dodson, 1973; Dygert & Liang, 2015; Sun & Lissenberg, 2018a) are in agreement, and that the rates are consistent for samples above and below the Moho at both localities. The rates obtained in this study are significantly higher than rates predicted in a Gabbro Glacier scenario (a), but consistent with deep hydrothermal circulation and convective cooling throughout the gabbroic section, as in a Sheeted Sills scenario (b). A model of hydrothermal cooling of the crust is shown as a vertical purple line in (b) for a reference permeability ( $k_0$ ) of  $2 \times 10^{-14}$  (Cherkaoui et al., 2003), the black arrow indicates that as crustal permeability increases, the cooling rate in the crust would correspondingly increase. Predicted cooling rates from published conductive-hydrothermal hybrid scenarios and a gabbro glacier scenario with concomitant off-axis hydrothermal circulation (blue field, Maclennan et al., 2005) are ~1 order of magnitude slower than rates obtained from our samples, implying that hydrothermal cooling efficiency exceeded ~80 kW/m. .... 38

Figure 1.10. Cooling rates from this study (Hess Deep, diamonds, OmanDP, squares) compared to rates gathered from the literature that were calculated using the methods we employed (Dygert et al., 2017; Sun and Lissenberg, 2018a, VanTongeren et al., 2008), or recalculated using those methods (Coogan et al.,

2002; Coogan et al., 2007; Faak and Gillis, 2016) (smaller symbols), plotted against structural depth. Symbol color corresponds to speedometric method (see legend). Conductive cooling models are also shown (see Section 5.3 and caption to Figure 1.9 for details). All samples originate from oceanic spreading centers or ophiolites with mid-ocean ridge tectonic affinity. Samples from localities with “normal” 6km thick crust are shown in (a), samples with thinner crust are shown in (b). Data from Faak and Gillis (2016) and the Atlantis Bank (Coogan et al., 2007) are placed at an arbitrary depth in the lower crustal section. The observations support hydrothermal cooling of oceanic lower crust at Hess Deep, Wadi Zeeb (OmanDP), Wadi Tayin, and the SWIR (Atlantis Bank). Samples from Wadi Abyad (Coogan et al., 2002) support conductive cooling of the lower oceanic crust. The gray lines in the background correspond to thermal scenarios lacking convective cooling beneath the extrusive section in (a) and with convective cooling extending to the crust-mantle boundary in (b). ..... 45

Figure 2.1. Diagram of components for molten salt cell and Griggs apparatus used in this study. Panel A shows the assembly for the sample in shear. Panel B shows the interior schematic for the force ram portion of the Griggs apparatus and panel C shows the entire Griggs apparatus. Figure modified from Holyoke and Kronenberg, 2010 for Rig 2 at the Brown University Rock Deformation lab..... 69

Figure 2.2. Mechanical data plots for deformed experiments from this study. Samples are color coded based on the spectrum at right, with pink representing ilm40 and green representing SCO. For samples with the same proportions of ilm40:SCO, sample hue is lighter for low total strain and darker for high accumulated strain. Mechanical data are cropped to begin at the hit point as calculated in MATLAB and end at initial pressure decrease at time of thermocouple failure and/or experiment completion..... 74

Figure 2.3. Ilmenite (0001) CPOs and Forsterite (001), (010) and (100) CPOs for samples LMO-001, - 002, -003, -004, & -005, with ilm40:SCO ratios and total accumulated shear strain and axial equivalent strain. All sample MUD scales are set to the color scale at the bottom of the figure. .... 76

Figure 2.4. Histograms of aspect ratio for samples analyzed with EBSD. The top row of histograms show both minerals in aggregate samples, with comparison of total grains. Individual mineral aspect ratio histograms are shown the combined plot for each sample, with pink histogram bars representing ilmenite and green bars representing olivine. Grains were defined using an angle of 10 degrees. .... 79

Figure 2.5. (A) Stress versus strain rate plot of published flow laws for ilm100 (Dyger et al., 2016; Tokle et al., 2021), ilm40 (Tokle et al., 2021) and wet olivine (Hirth & Kohlstedt, 2003), plotted with individual experiment data from past studies and this study. Squares represent data for ilm100 from Dyger et al. (2016), stars are ilm40 data from Tokle et al. (2021) and circles are this study. (B) Percent olivine on the x-axis versus logarithmic scale of viscosity on the y-axis. This plot shows the predicted viscosities for samples of 100% ilm40 on the left and 100% SCO on the right edges of the plot based on published flow laws (Hirth & Kohlstedt, 2003; Tokle et al., 2021). The black line shows the mixing model of the two phases as calculated by Tullis et al. 1991. Any sample data that plots in the pink region of the

graph has a rheology controlled by the weak phase, ilmenite. If data plots in the green region of the graph, its rheology is controlled by the strong phase, olivine. . 81

Figure 3.1. Depth into the Earth in kilometers (km) versus Temperature in Kelvin (A) and Pressure in gigapascals (GPa) (B). The average boundary thickness of the Upper Mantle, Mantle Transition Zone, Lower Mantle, D double prime (D'') layer, Outer Core and Inner Core are shown by dashed lines. .... 97

Figure 3.2. Carbon phase diagram for Earth-relevant conditions. Plot A shows just the phase diagram while plot B has an overlay of the pressure-temperature path through the Earth based on Table 3.1..... 100

Figure 3.3. Based on figure 4.6 from *Deep Carbon* chapter 4 “Carbon-Bearing Phases throughout Earth’s Interior”, showing simplified distribution and forms of carbon inside the Earth. The thickness of the oceanic crust and subducting slab are vertically exaggerated for clarity in comparison to values in Table 3.3..... 104

Figure 3.4. Guidance for building atomic structures of graphite (A) and diamond (B) based on materials from [indigostruments.com](http://indigostruments.com). .... 107



## **List of Attachments**

Attachment Chapter\_1\_Data\_Tables.xlsx contains analytical data related to the contents of Chapter 1 in Tables 1.3 and 1.5 to 1.11.

## Introduction

The interiors of terrestrial planets provide a wealth of opportunities for scientific research, on Earth, satellites, and other planets in the inner Solar System.

Advancements in technology have allowed for refinement of early views, but our inability to retrieve samples directly from the mantles of planetary bodies leads to constraints from geophysical surveying, tectonically exhumed samples, and experimental work on analogs to interior systems. This dissertation will take three separate approaches to our knowledge and understanding of planetary interiors, through natural samples, deformation of analogous materials, and secondary school curriculum integrating state standards for the physical sciences with mineral formation processes.

Chapter 1 focuses on the comparison of lithospheric samples of the crust and mantle from an ophiolite, formed at a fast-spreading ridge then obducted onto the continental crust of what is now Oman, to dredge and core samples from Hess Deep, where the tectonic window formed by a ridge-ridge-ridge triple junction has exhumed lower crustal and upper mantle rocks to surface and near-surface locations in a very short geologic time frame. Through geochemical analysis of minerals and mineral pairs in samples from both location, we have shown similar cooling trends in both localities that suggest the requirement of ocean water circulation to depths at or below the petrologic Moho. This study has not only aided in further constraining the formation conditions of the Samail Ophiolite in Oman, but it has also refined the long-debated models for crustal emplacement at depth along fast-spreading ridge axes.

Chapter 2 uses deformation experiments on a Griggs apparatus to investigate the strength contrast between cumulate mantle-analog rocks, similar to those crystallized early in the Lunar magma ocean sequence, and overlying ilmenite-bearing cumulates, crystallized at the end stages of magma ocean solidification and cooling. Due to the known density contrast between the two layers, it is presumed that Rayleigh-Taylor instabilities formed between the ilmenite-bearing cumulates and the cumulate mantle, leading to the ultimate overturn of the Lunar mantle. To constrain the geometry of these instabilities, the viscosity contrast and aggregate material behavior is needed. Mechanical data interpretations and microstructural analysis from this study provide

insights into properties which could aid in future geodynamic modeling of the lunar interior.

Chapter 3 is an exploration of mineralogy in the context of state science standards set by Tennessee as of 2018. Lack of Earth Science requirements beyond grade 8 means that geoscience-related education as a supplement to Biology, Chemistry or Physics is more likely to reach high school students. This chapter details a lesson on comparing native minerals of carbon, diamond and graphite, with formation conditions and structural properties, through a hands-on activity and pre- and post-activity lessons. This lesson plan was created as part of a grant provided to multiple researchers at the University of Tennessee, to create Lessons-in-a-Box for distribution through the Knox County Library, so that secondary science educators can borrow the materials at no cost for use in their classroom.

**Chapter 1: Thermal history of lithosphere formed beneath fast spreading ridges: Constraints from the Mantle Transition Zone of the East Pacific Rise at Hess Deep and Oman Drilling Project, Wadi Zeeb, Samail ophiolite**

A version of this chapter was originally published by Nadine L. Grambling, Nicholas Dygert, Beau Boring, Marlon M. Jean, and Peter B. Kelemen:

*Grambling, N.L., Dygert, N., Boring, B., Jean, M.M., and Kelemen, P.B. "Thermal history of lithosphere formed beneath fast spreading ridges: Constraints from the Mantle Transition Zone of the East Pacific Rise at Hess Deep and Oman Drilling Project, Wadi Zeeb, Samail ophiolite." JGR Solid Earth (2022): v. 127, no. 1, pp. 1-27.*

Nadine Lynne Grambling led the data analysis, conceptualization, writing, and development of this article and assisted in sample collection and preparation. Nicholas Dygert supervised the direction of the article and led revisions. He also assisted with sample collection. Beau Boring assisted in data collection and with revisions. Marlon M. Jean assisted with sample collection and preparation and revisions. Peter B. Kelemen assisted with sample collection and content revisions.

## **Abstract**

We investigate the cooling histories of peridotites and gabbros from localities that expose oceanic lithosphere formed beneath two fast seafloor spreading centers: Hess Deep as recovered from IODP Expedition 345 and ODP Leg 147, and the Oman Ophiolite as sampled by the Oman Drilling Project, ICDP Expedition 5057 (OmanDP). At these locations, relict crust-mantle transition zones are directly sampled, enabling characterization of the thermal history of the crust-mantle transition, and by inference, the depth extent of hydrothermal circulation beneath spreading centers. We measured major and trace element abundances in crustal gabbros and mantle peridotites from Hess Deep and OmanDP and applied major and trace element-based thermometers. Geospeedometric interpretation of the temperatures suggests similar cooling histories at both locations; cooling rates ranged from 0.02 to 2.6 °C/y from peak temperatures up to 1350°C. The rates are consistent on either side of the paleo-Moho (i.e., in the crust and mantle). Models for conductive cooling of the lower oceanic crust predict rates more than two orders of magnitude slower at the crust-mantle transition zone, while thermal models that invoke deep and efficient hydrothermal circulation throughout the entire

crustal section predict rates consistent with our observations. We infer that hydrothermal cooling extended to or near the petrologic Moho beneath the East Pacific Rise and the OmanDP paleo-spreading center, consistent with the Sheeted Sills model for crustal accretion. Comparison with previously published rates recalculated using the methods we employed suggests the oceanic lower crust is cooled hydrothermally in some places and by conduction at others.

## 1. Introduction

Investigation of the thermal histories of oceanic crust and mantle at ophiolites and samples from abyssal environments have been undertaken to elucidate the geologic mechanisms that form lithosphere beneath spreading centers (e.g., Canil et al., 2019; Coogan et al., 2002, 2007; Dygert et al., 2017; Dygert & Liang, 2015; Faak et al., 2015; Faak & Gillis, 2016; Garrido et al., 2001; Mock et al., 2021; Sun & Lissenberg, 2018a; VanTongeren et al., 2008). These studies have fueled debate over crustal formation mechanisms and the thermal structure of the lower crust and mantle beneath intermediate to fast-spreading centers (Purdy et al., 1992). At the crux of this debate is an argument over mechanisms that form the gabbroic lower crust beneath mid-ocean ridge axes, which is intimately related to thermal structure and thermal evolution beneath spreading centers.

Two end-member models are often invoked to explain the formation of oceanic crust. In the Gabbro Glacier model, crust accretes from solidification of a large axial magma lens which migrates downward and outward from the ridge axis in a "gabbro glacier" as seafloor spreading progresses (Fig. 1.1a). In the Sheeted Sills model, oceanic crust accretes from continuous solidification of sills at a range of depths beneath ridge axes (Fig. 1.1b). These models make fundamentally different predictions for lithospheric cooling: the former invokes conductive (slow) cooling of the crust and underlying mantle, while the latter requires deep and efficient hydrothermal circulation beneath spreading centers to quickly solidify sills shortly after emplacement (see Section 1.0.1 for a more detailed description and evaluation of the evidence for and against the crustal accretion models).

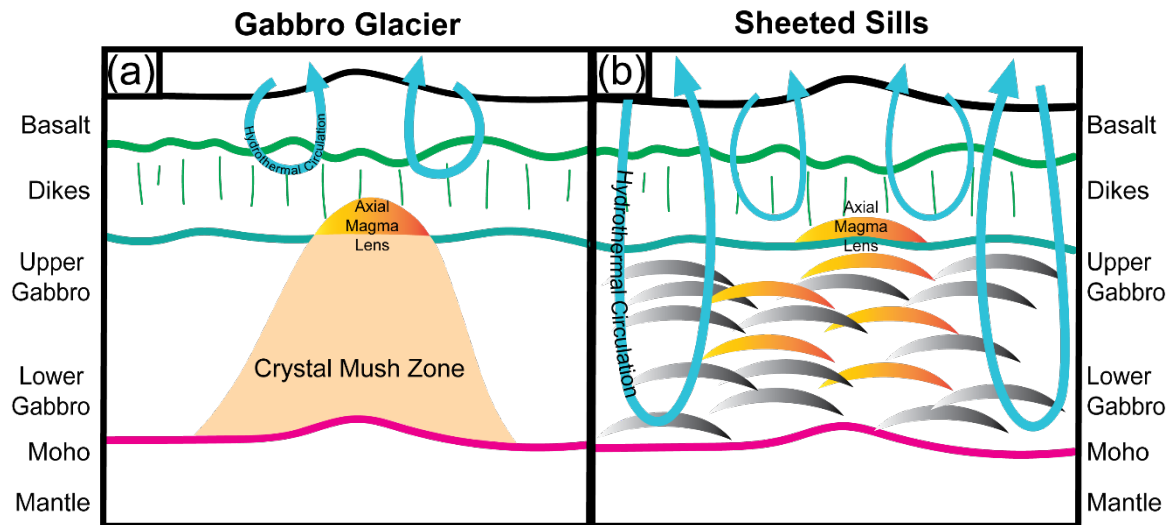


Figure 1.1. Schematic illustrating end-member crustal accretion models. (a) The Gabbro Glacier model (e.g. Henstock et al., 1993; Phipps Morgan & Chen, 1993; Quick & Denlinger, 1993; Sinton & Detrick, 1992; Sleep, 1975); (b) the Sheeted Sills model (e.g. Kelemen, Hirth, et al., 1997; Kelemen, Koga, et al., 1997; Korenaga & Kelemen, 1997; VanTongeren et al., 2008, 2015). The Gabbro Glacier model posits that the lower section of crust is formed accretion of by a large zone of crystalline mush, which accumulates beneath an axial magma lens at the base of the upper crustal dikes. In this model, cooling of the entire lower crustal section and underlying mantle is purely conductive, through heat lost to the hydrothermally cooled extrusive section (basalts and dikes). (b) The Sheeted Sills model assumes similar crustal accretion in the extrusive section (basalts and dikes) but diverges from the gabbro glacier model in the lower crust. In this model, the lower crust is formed from the injection of a multitude of magmatic sills at a range of depths beneath an axial magma lens at the base of the extrusive section. Deep and vigorous hydrothermal circulation through the entire crustal section (through networks of fractures) is required to accommodate heat released by solidification of the sills, which necessarily produces fast cooling rates in the entire lower crustal section and uppermost part of the mantle section.

Divergent thermal histories for the lower crust and uppermost mantle invoked by the Sheeted Sills and Gabbro Glacier models are testable by application of geothermometry and geospeedometry to oceanic gabbros and peridotites. These techniques rely on diffusively moderated temperature sensitive exchange of elements or mineral components among a phase assemblage, e.g., partitioning of the diopside component around the two-pyroxene solvus (e.g. Brey & Köhler, 1990), exchange of Ca and Fe-Mg between olivine and clinopyroxene (Köhler & Brey, 1990), Fe-Mg and Ca exchange between coexisting plagioclase and clinopyroxene (e.g. Faak et al., 2013; Sun & Liang, 2017; Sun & Lissenberg, 2018a), and exchange of rare earth elements (REEs) between coexisting pyroxenes (Dygert & Liang, 2015; Liang et al., 2013) and plagioclase and clinopyroxene (Sun & Liang, 2017). Application of geothermometers and geospeedometers (hereafter thermometers and speedometers) to oceanic lithosphere from ophiolites and drilled and dredged samples from mid-ocean ridges has produced inconsistent results, which have been used to invoke both end-member models for crustal accretion, see Section 1.0.2 below for a summary (e.g. Coogan et al., 2002, 2007; Dygert et al., 2017; Faak et al., 2015; Faak & Gillis, 2016; Garrido et al., 2001; Sun & Lissenberg, 2018a; VanTongeren et al., 2008). These inconsistent conclusions may be related to the disparate methods used to constrain cooling rates, and/or local geologic history, as many studies investigated different localities (Hess Deep gabbros being a prominent exception, Faak et al., 2015; Faak & Gillis, 2016; Sun & Lissenberg, 2018a).

Here, we apply the aforementioned thermometers and speedometers to gabbros and mantle harzburgites from the Hess Deep rift (East Pacific Rise, EPR) and the Oman Drilling Project (Wadi Zeeb, Samail ophiolite, OmanDP). These localities present a unique opportunity to explore the coupled thermal history of crust and mantle lithosphere formed beneath intermediate-fast spreading centers, direct comparison with studies that used alternative speedometric methods to constrain thermal histories (Faak et al., 2015; Faak & Gillis, 2016; Sun & Lissenberg, 2018a), and the opportunity to apply a variety of independently calibrated speedometric methods to a continuous section of core drilled through the crust-mantle transition zone. Additionally, we compare our new



speedometric results to cooling rates calculated from previously published data, recalculated using the same methods. Our objective is to advance the debate beyond arguments about the strengths and weaknesses of alternative speedometric approaches, which involve obtaining cooling rates from averaged mineral compositions or grain-scale mineral traverses, as well as differing thermometric calibrations and kinetic models (cf., Coogan et al., 2007; Sun & Lissenberg, 2018a, and the comment by Faak et al. (2018) and Sun & Lissenberg (2018b)), to a focus on establishing whether cooling mechanisms do or do not differ among localities, and providing data for future studies to evaluate why cooling mechanisms might be different in different places. Additionally, our study enables direct comparison of the thermal history of oceanic mantle lithosphere that formed beneath a mid-ocean ridge spreading center with a typical crustal section, to lithosphere from a mid ocean ridge-like ophiolitic setting using consistent methods.

### *1.0.1 Crustal Accretion models*

Early models for crustal formation beneath oceanic spreading centers called for a large magma chamber beneath the ridge axis, extending from the base of the extrusive section of oceanic crust to the petrologic Moho (e.g., Pallister & Hopson, 1981; Smewing, 1981). These models explain mineral stratification observed in lower crustal gabbros as a product of crystal settling, often observed in layered intrusions, but are not supported by seismic studies, which failed to reveal extensive low velocity zones (LVZ) beneath mid ocean ridge spreading centers (e.g., Detrick et al., 1987, 1993; Dunn & Toomey, 2000). The Gabbro Glacier model is a next-generation permutation, invoking the presence of a relatively thin and narrow magma lens immediately beneath the extrusive section of oceanic crust, from which the entire lower crust solidifies (e.g., Dewey & Kidd, 1977; Henstock et al., 1993; Nicolas et al., 1988; Phipps Morgan & Chen, 1993; Quick & Denlinger, 1993; Sinton & Detrick, 1992; Sleep, 1975). In this model, as hydrothermal cooling of the uppermost part of the magma lens occurs and as seafloor spreading continues, viscously deforming solid material at the base of the lens sinks downward and outward to form the gabbroic section of the crust as in a deforming glacier (Fig. 1.1a). In the Gabbro Glacier model, hydrothermal cooling is necessarily

restricted to the pillow basalts and dikes of the upper crust, because the gabbro glacier must deform as a viscous solid. In this scenario, the gabbro cools conductively, leading to a rapid and systematic decrease in cooling rates in the lower crust with depth (e.g. Coogan et al., 2002; Faak et al., 2015; Faak & Gillis, 2016; Gillis et al., 2014; Quick & Denlinger, 1993).

The alternative end-member Sheeted Sills model invokes lower crustal emplacement by crystallization of many thin magmatic sills at a range of depths beneath the ridge axis, which are cooled convectively by hydrothermal circulation that extends to the crust-mantle boundary during seafloor spreading (Kelemen, Hirth, et al., 1997; Kelemen, Koga, et al., 1997; Korenaga & Kelemen, 1997; VanTongeren et al., 2008, 2015). In this scenario, deep and efficient hydrothermal circulation is required to accommodate the latent and specific heat released by crystallization of sills at a range of depths beneath the ridge axis, beneath an axial magma lens. The Sheeted Sills model is supported by rhythmic, meter-scale geochemical variations observed within lower oceanic crust (e.g., Korenaga & Kelemen, 1997), hydrothermal (fast) cooling rates in lower crustal gabbros and peridotites directly beneath the crust-mantle transition zone (Dygert & Liang, 2015; VanTongeren et al., 2008), and systematic spatial variations in cooling rate deeper in the mantle section suggesting hydrothermal cooling above the crust-mantle transition and conductive cooling below (Dygert et al., 2017). A Sheeted Sills scenario is also supported by the observation of plagioclase a-axis girdles in crustal gabbros reflecting compaction-related shape preferred orientations (VanTongeren et al., 2015), inconsistent with crystallographic alignments associated with high strains, as required in a Gabbro Glacier scenario (e.g. Quick & Denlinger, 1993), and geochemical evidence for hydrothermal interaction between seawater and oceanic lithosphere under high temperature conditions (e.g. Gregory & Taylor, 1981; Nielsen et al., 2000).

### *1.0.2 Results from previous investigations that constrained cooling rate variations in oceanic lithosphere*

Here we briefly summarize results from previous speedometric studies of oceanic lithosphere. Garrido et al. (2001), applied crystal size distribution analysis to plagioclase

in gabbros from Wadi Khafifah in the southern Oman ophiolite, obtaining cooling rates in the shallow intrusive crust that decreased with depth, and were interpreted to be most consistent with hydrothermal cooling and solidification of the intrusive oceanic crust in sheeted sills. Coogan et al. (2002) applied a Ca-in-olivine thermometer to samples from a thin (3km thick) crustal section in the northern Oman ophiolite (Wadi Abyad) and interpreted the data using a 1-D grain scale model for diffusive exchange between olivine and clinopyroxene. The same data were reanalyzed by Coogan et al. (2007) using a revised Ca in olivine diffusion coefficient (Coogan et al., 2005), producing a smooth, systematic decrease in cooling rate with depth in the crustal section (rates of  $10^{-1}$  °C/y near the sheeted dikes to  $10^{-6}$  °C/y near the crust-mantle transition), consistent with conductive cooling of the crust. Coogan et al. (2007) additionally investigated samples from an ultra-slow spreading segment of the Southwest Indian Ridge (SWIR). They found moderately fast, uniform cooling with depth ( $10^{-3}$  to  $10^{-2}$  °C/y). Van Tongeren et al. (2008) applied a Ca-in-olivine thermometer and Dodson (1973) closure temperature model to gabbros from Wadi Khafifah, southern Oman ophiolite, obtaining fast and uniform cooling rates with depth throughout the gabbroic section ( $10^{-2}$  to 1 °C/y).

At Hess Deep, Faak & Gillis (2016) investigated olivine gabbros and troctolites inferred to originate from the shallow crust, as well as deeper plutonics, and found a spatially varying gradient in cooling rate of  $\sim 0.3$  °C/y in the shallow crust to  $10^{-4}$  °C/y in the deeper crust using a Mg-in-plagioclase thermometer and a speedometric method based on inversion of grain-scale chemical variations (or lack thereof, Faak et al., 2014). Faak et al. (2015) investigated the same Hess Deep samples as well as several gabbros from Pito Deep (along the margin of the Easter microplate) and IODP hole 1256D, reaching similar conclusions. Dygert et al. (2017) applied Ca-in-olivine and REE-in-two-pyroxene-based speedometric methods (Dygert & Liang, 2015) to mantle peridotites from Wadi Tayin, southern Oman ophiolite, and observed a smooth and systematic decrease of cooling rate with depth moving deeper into the mantle section beneath the crust ( $\sim 0.1$  °C/y near the crust-mantle transition and  $10^{-3}$  °C/y 4km beneath it). Sun & Lissenberg (2018a) developed a coupled Mg-in-plagioclase and REE-in-

clinopyroxene-plagioclase speedometer based on averaged mineral compositions and applied it to Hess Deep gabbros inferred to come from structural depths greater than those investigated by Faak et al. (2015; 2016). They determined fast and near uniform cooling rates with depth ( $\sim 1$  to  $10^{-2}$  °C/y), and inferred that hydrothermal circulation cooled the entire Hess Deep lithosphere, which accreted from solidification of periodically replenished magma bodies (sills). Mock et al. (2020) investigated gabbros from the mid-plutonic and lowermost crust at the southern Oman ophiolite (Smail and Wadi Tayin massifs, respectively), recovering cooling rates of  $\sim 10^{-2}$  °C/y and  $\sim 10^{-1}$  °C/y through Ca-in-olivine and Mg-in-plagioclase closure temperatures, and demonstrating efficient heat loss from the lowermost crust, perhaps by deep hydrothermal circulation.

### **1.1 Study Areas**

Samples investigated in this study were drilled in ophiolitic and abyssal settings. The lithosphere recovered from ophiolites and abyssal environments provides insights into the architecture and thermal history of intermediate to fast-spreading mid-ocean ridges, however, these environments represent imperfect analogs for the oceanic lithosphere most common in the ocean basins. Ophiolite sequences are well exposed but interpreted to represent spreading centers from trench-proximal settings that differ geochemically and tectonically from mid-ocean ridges (e.g., MacLeod et al., 2013; Pearce et al., 1981; Rioux et al., 2016). On the other hand, oceanic lithosphere drilled and dredged from the seafloor lacks geologic context, and typically comes from magma starved spreading centers, which are not thermally or structurally representative of oceanic lithosphere with a typical 6-km thick crustal section (e.g. Cannat et al., 2004; Chen, 1992; Dick et al., 2003). By obtaining new geochemical data and thermal histories from the Smail ophiolite and a tectonic window in the East Pacific Rise, we overcome these potential sampling biases, thus enabling direct comparison between ophiolitic lithosphere and oceanic lithosphere formed beneath a normal mid-ocean ridge.

### *1.1.1 Wadi Zeeb, Oman ophiolite, as sampled by the Oman Drilling Project*

The Samail ophiolite in the Sultanate of Oman and the United Arab Emirates, exposes 5-6 km of oceanic crust and in places, underlying mantle peridotite representing >10km of structural depth obducted onto the Arabian margin (Boudier & Coleman, 1981; Hanghøj et al., 2010; Nicolas, 1989). Though the tectonic setting during formation is debated, geochemical and geologic evidence suggests the southern part of the ophiolite formed in a setting similar to modern fast-spreading ridges such as the East Pacific Rise (e.g. Braun, 2004; Garrido et al., 2001; Godard et al., 2000; Hanghøj et al., 2010; Kelemen et al., 1995; Kelemen, et al., 1997a; Kelemen, et al., 1997b; Nicolas, 1989; Pallister & Knight, 1981). See Mock et al. (2021) for a concise summary. Samples in the present study were drilled as part of Phase 2 of the international Oman Drilling Project at Wadi Zeeb, Northern Sharqiyah, a location near an axis of a paleo-spreading center as mapped in previous petrologic and structural studies, (Nicolas, 1989; Nicolas & Boudier, 2015; Python & Ceuleneer, 2003). The inferred tectonic setting of the sampling area is shown in Figure 1.11 (in Appendix 1).

Phase 2 of the Oman Drilling Project sampled two continuous sections of rock that encompass the crust, crust-mantle transition zone (CMTZ) and uppermost mantle at holes CM1A and CM2B from November 2017 to January 2018. Hole CM1A, drilled at 30° from vertical to correct for the southwestward dip of the ophiolitic strata, began in the gabbroic lower crust, coring 150 m before reaching the CMTZ (as defined by the onset of dunites) and another 150 m through the CMTZ until reaching upper mantle harzburgites. The upper mantle harzburgites were cored for 100 m, producing a total of 400 m of core at CM1A. Hole CM2B was drilled vertically relative to the surface (i.e., at an angle of 60° relative to the ophiolitic strata) and began in the CMTZ, coring 110 m of CMTZ, followed by 180 m of mantle peridotites. The samples investigated here include gabbros, a troctolite, and peridotites collected above and below the crust-mantle transition. These samples originate from both holes. The structural depth relationships among the samples are well established by the locations and orientations of the holes, sampling depths, and a common lithological horizon marked by the onset of continuous dunites (Kelemen et al., 2021a, 2021b).

### *1.1.2 Hess Deep*

Hess Deep provides a globally unique exposure of lithosphere initiated within the last ~1.5 Ma (Lonsdale, 1988). The Hess Deep tectonic window emerged from the instability of ridge-ridge-ridge spreading between the Pacific, Cocos and Nazca plates at the Galapagos Triple Junction (e.g. Klein et al., 2005; Lonsdale et al., 1992). Despite the tectonic complexity of the Galapagos microplate region, the EPR origin of the rocks at Hess Deep is well established and provides exposures of rock that represent the full suite of crust and upper mantle lithologies from a contemporary fast spreading mid-ocean ridge (e.g. Girardeau & Francheteau, 1993; Hekinian et al., 1993; Karson et al., 2002; Lissenberg et al., 2013; Natland & Dick, 2009). The samples used in this study are gabbros and peridotites from Ocean Drilling Project (ODP) Leg 147 (1992-1993) and International Ocean Drilling Project (IODP) Expedition 345, Site 1415 (2012-2013) (Gillis et al., 2014; Mevel et al., 1996). Site 1415 is located along the southern slope of the intrarift ridge between 4675 and 4850 m below sea level and is covered with approximately 10–30 m of gabbroic rubble overlain by a few meters of pelagic sediment mixed with lithic debris (Gillis et al., 2014). The samples investigated were recovered from holes 1415G and 1415J. Collectively, the holes sampled three units of note: Unit 1 – surficial rubble zone, Unit 2 – oikocryst-bearing layered gabbro series, and Unit 3 – troctolite series. Hole G penetrated Unit 1, while Hole J penetrated all three units (c.f. Mevel et al., 1996 for site 894 and 895 characterizations from ODP Leg 147). The sampling locations and their relation to the inferred local geology is shown in Figure 1.11.

## **2. Sample Description**

### **2.1 Samples**

Sample names and locations, lithologies, leg and expedition number, and drill site information are reported in Table 1.1. Six gabbros (three each from Hess Deep and OmanDP), one troctolite (OmanDP), and eight harzburgitic peridotites (four from each locality) were investigated here. Representative cross-polarized light and backscatter

Table 1.1. Samples and sampling locations.

Sample	Location	Lithology	Latitude (°N)	Longitude (°)	Leg/Expedition Number	Site	Hole	Depth in hole (m)	Structural depth* (m)
345_1415G_1R1_0-4	HD	Gabbro	2°15.1'90'	101°32.6'63' W	IODP Exp 345	1415	G	0	--
345_1415J_4R1_2-6	HD	Gabbro	2°15.1'04'	101°32.6'22' W	IODP Exp 345	1415	J	22.2	--
147_894G_9R4_60-67	HD	Gabbro	2°17.'77'	101°31.'55' W	ODP Leg 147	894	G	79.1	--
5057_5707A_009z_03_059-063	OmanDP	Troctolite	22°54.'35'	58°20.'49' E	ICDP Exp 5057	CM1	A	16.1	296.9
5057_5707A_032z_02_053-056	OmanDP	Gabbro	22°54.'35'	58°20.'49' E	ICDP Exp 5057	CM1	A	72	241
5057_5707A_059z_04_004-008	OmanDP	Gabbro	22°54.'35'	58°20.'49' E	ICDP Exp 5057	CM1	A	148	165
5057_5707A_113z_03_036-040	OmanDP	Gabbro	22°54.'35'	58°20.'49' E	ICDP Exp 5057	CM1	A	259	54
147_895D_3R1_22-27	HD	Harzburgite	2°16.'35'	101°26'77' W	ODP Leg 147	895	D	26.2	--
147_895D_3R1_66-69	HD	Harzburgite	2°16.'35'	101°26'77' W	ODP Leg 147	895	D	26.6	--
147_895D_5R1_70-76	HD	Harzburgite	2°16.'35'	101°26'77' W	ODP Leg 147	895	D	44	--
147_895D_5R1_140-144	HD	Harzburgite	2°16.'35'	101°26'77' W	ODP Leg 147	895	D	44.7	--
5057_5708B_100z_03_035-040	OmanDP	Harzburgite	22°54.'60'	58°20.'49' E	ICDP Exp 5057	CM2	B	223	-71.9
5057_5708B_114z_02_030-034	OmanDP	Harzburgite	22°54.'60'	58°20.'49' E	ICDP Exp 5057	CM2	B	261	-104.8
5057_5708B_119z_03_006-009	OmanDP	Harzburgite	22°54.'60'	58°20.'49' E	ICDP Exp 5057	CM2	B	274	-116
5057_5708B_124z_02_076-081	OmanDP	Harzburgite	22°54.'60'	58°20.'49' E	ICDP Exp 5057	CM2	B	286	-126

\*Relative to base of crust-mantle transition zone as defined by the onset of dunitic units. (HD = Hess Deep, OmanDP = Oman Drilling Project).

electron micrographs are shown in Figure 1.2. To first order, sample characteristics are similar for the two localities.

Gabbros are poikilitic, medium grained (0.25-1 mm) and granular consisting of euhedral to subhedral plagioclase and anhedral clinopyroxene (e.g., Figure 1.2a, d) and olivine. Clinopyroxenes in Hess Deep gabbros occasionally host exsolution lamellae and are often oikocrystic with plagioclase chadacrysts. OmanDP gabbros have fewer clinopyroxene oikocrysts and exsolution lamellae are largely absent. One pyroxene-free troctolite was analyzed in this study (OmanDP). This sample contains subhedral olivine, with grain sizes of 0.5-1 mm and 0.5-1 mm euhedral to subhedral plagioclase. Olivines in the troctolite are relatively fresh, but olivine grain rims and fractured interiors are serpentinized.

Olivines in the gabbros (both localities) are interstitial and fractured but remain fresh relative to olivines in the peridotites. Based on visual inspection of the thin sections and the core descriptions, we estimate that total gabbro alteration ranges from ~5 to 20% and is mostly concentrated among olivines and clinopyroxene rims. Hess Deep gabbros are altered homogeneously across the thin sections while OmanDP gabbros are altered in ~1mm thick anastomosing veins of variable spacing, decorated by magnetites, and occasional patches of alteration several mm across. Sample 147\_894G\_9R4\_60-67 (Hess Deep) and 5057\_5707A\_059z\_04\_004-008 (OmanDP), show higher degrees of alteration (60-70% total; e.g., Mevel et al., 1996, Table 1.3), but in all cases, fresh mineral grains are present for analysis.

Peridotites (all clinopyroxene-poor harzburgites) are porphyroclastic and extensively altered (~75-95% Table 1.3). Olivines are almost completely serpentinized, however, dispersed remnants of olivine grain interiors are present in all peridotites (Figure 1.2b, c, e, f). Original olivine grain size was estimated by finding the average radius across unaltered relics of matched birefringence, and/or using magnetite decorations that indicate original grain boundaries. Most clinopyroxenes in peridotite samples are small (~100 $\mu$ m), subhedral to euhedral, and interstitial (e.g., Figure 1.2c, f), but in some cases larger grains up to several mm are present (Figure 1.2b). Orthopyroxene porphyroclasts



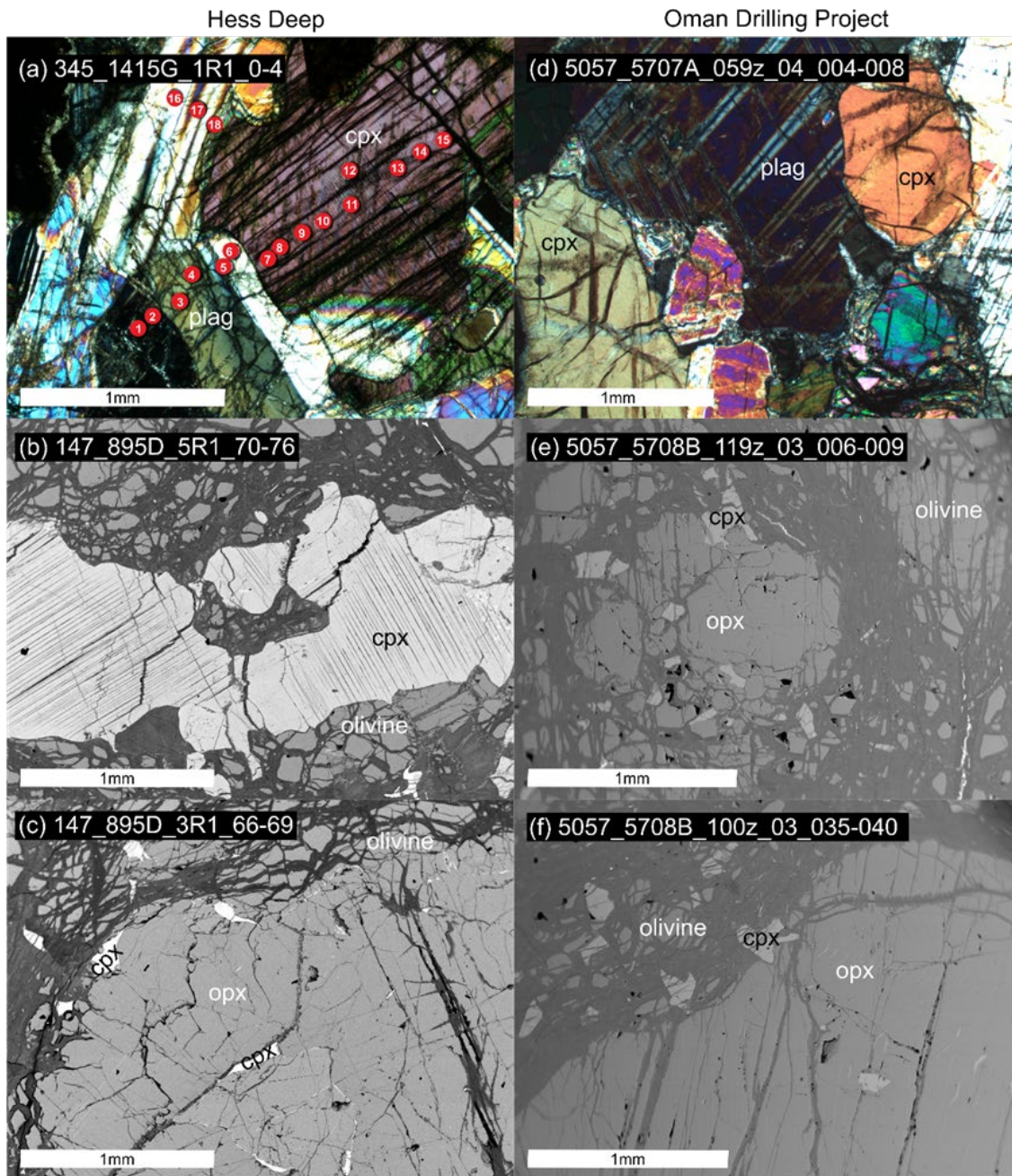


Figure 1.2. Representative cross polarized light and backscatter electron photomicrographs of samples from Hess Deep and Oman Drilling Project (left and right columns, respectively). (a) is a crustal gabbro from site 1415G, IODP Expedition 345 and (b) and (c) are upper mantle peridotites from hole 895D of ODP Leg 147. (d) is a crustal gabbro from hole CM1 and (e) and (f) are peridotites from the crust-mantle transition of hole CM2. Red spots in (a) correspond to LA-ICP-MS spot numbers shown in Figure 1.5. According to petrographic observation and modal mineralogy (Table 1.3), clinopyroxenes interpreted to be residual are shown in the middle row; the bottom row (c), (f) shows samples with minor clinopyroxene that may have exsolved at subsolidus temperatures, and/or crystallized from melt present during cooling.

are typically fresh, one to several mm in diameter, and anhedral to subhedral, with minor or absent exsolution lamellae (e.g., Figure 1.2e, c, f).

### **3. Analytical Methods**

#### **3.1 Major Element Analysis**

Analytical work was conducted at the University of Texas at Austin and the University of Tennessee, Knoxville on thin sections of standard or double thickness. Major elements were analyzed in Hess Deep samples at the University of Texas; major elements were analyzed in OmanDP samples at the University of Tennessee. Analyses at the University of Texas were conducted using a focused beam on a JEOL JXA-8200 electron microprobe. Olivine, orthopyroxene, clinopyroxene, chromite, and plagioclase were analyzed at 15kV and 30nA beam current. Na signal intensity was monitored as a function of time during plagioclase analysis and did not exhibit statistically significant decay or merit application of a Time Dependent Intensity correction (Donovan et al., 2016). Counting intervals were typically 30 seconds on peak and 15 seconds on background; for Ca in olivine, they were 40 seconds on peak and 20 seconds on background. Based on counting statistics, we estimate CaO detection limits of ~0.014 wt% for olivine. Natural and synthetic reference materials were employed and data were processed using a ZAF matrix correction procedure.

Analyses at the University of Tennessee were conducted using a Cameca SX-100 electron microprobe. Olivine, orthopyroxene, clinopyroxene, and chromite were analyzed using a 1 $\mu$ m beam at 15kV and 30nA. Counting intervals were generally 30 seconds on peak and 15 seconds on background; for Al and Ca in olivine, they were 100 seconds on peak and 50 seconds on background. Based on counting statistics, we estimate detection limits for CaO and Al<sub>2</sub>O<sub>3</sub> in olivine of 0.012 and 0.009 wt%, respectively. Plagioclase was analyzed using a 5 $\mu$ m beam at 15kV and 10nA with counting intervals of 30 seconds on peak and 15 seconds on background. Natural and synthetic reference materials were employed and data were processed using a ZAF correction applied using the Cameca PAP procedure.

### **3.2 Trace Element Analysis**

Mg, Si, Li, Sc, Ti, Sr, Zr, Nb, Pb, Y, and REEs were analyzed in orthopyroxene, clinopyroxene and plagioclase at the University of Texas using a New Wave UP193FX laser with a dual-volume sample chamber coupled to an Agilent 7500ce Quadrupole Inductively Coupled Plasma Mass Spectrometer (ICP-MS). Samples were analyzed in three separate analytical sessions, at a laser frequency of 10 hertz, with fluences of 2.6, 2.9, and 1.4 J/cm<sup>2</sup>. The different fluences were selected according to count returns and ablation signal time for analytes of interest in preliminary analyses of the unknowns. Optimal conditions varied according to thin section thickness and the phases to be analyzed, and ensured introduction of measurable quantities of REEs into the ICP-MS with 60 second ablations that penetrated through the samples completely. Synthetic NIST glasses (610 and 612) and a natural basalt (BCR-2G) were used as reference materials. Data were processed in LasyBoy (Sparks, 2011) with Si as the reference analyte. Spot sizes ranged from 40-100µm. The largest spots possible were used (up to 100µm) while avoiding cracks or alteration. Reference materials were analyzed twice or in triplicate before and after the unknowns using the same or similar spot sizes as the unknowns. REE detection limits vary depending on ICP-MS background counts, ranging from a few to tens of ppb for each analysis. Replicate analyses of BCR-2G are reported in Table 1.4 (Attachment Chapter\_1\_Data\_Tables.xlsx) for the analytical sessions in which trace element data were obtained, and demonstrate good reproducibility (≤6%) and recovery within ~10% of GeoReM accepted values (Jochum et al., 2005).

## **4. Analytical and Thermometric Results**

### **4.1 Major elements**

Major elements in clinopyroxene, orthopyroxene, plagioclase, olivine, and spinel are presented in Tables 1.5-11 (Attachment Chapter\_1\_Data\_Tables.xlsx) respectively, as averages, with 1σ standard deviations of replicate analyses for each thin section (see Section 4.1.1 for a description of major element zoning). Averaged major element variations in plagioclase, clinopyroxene, olivine and spinel are plotted in Figure 1.3. Samples from Hess Deep are shown as orange diamonds, OmanDP samples are

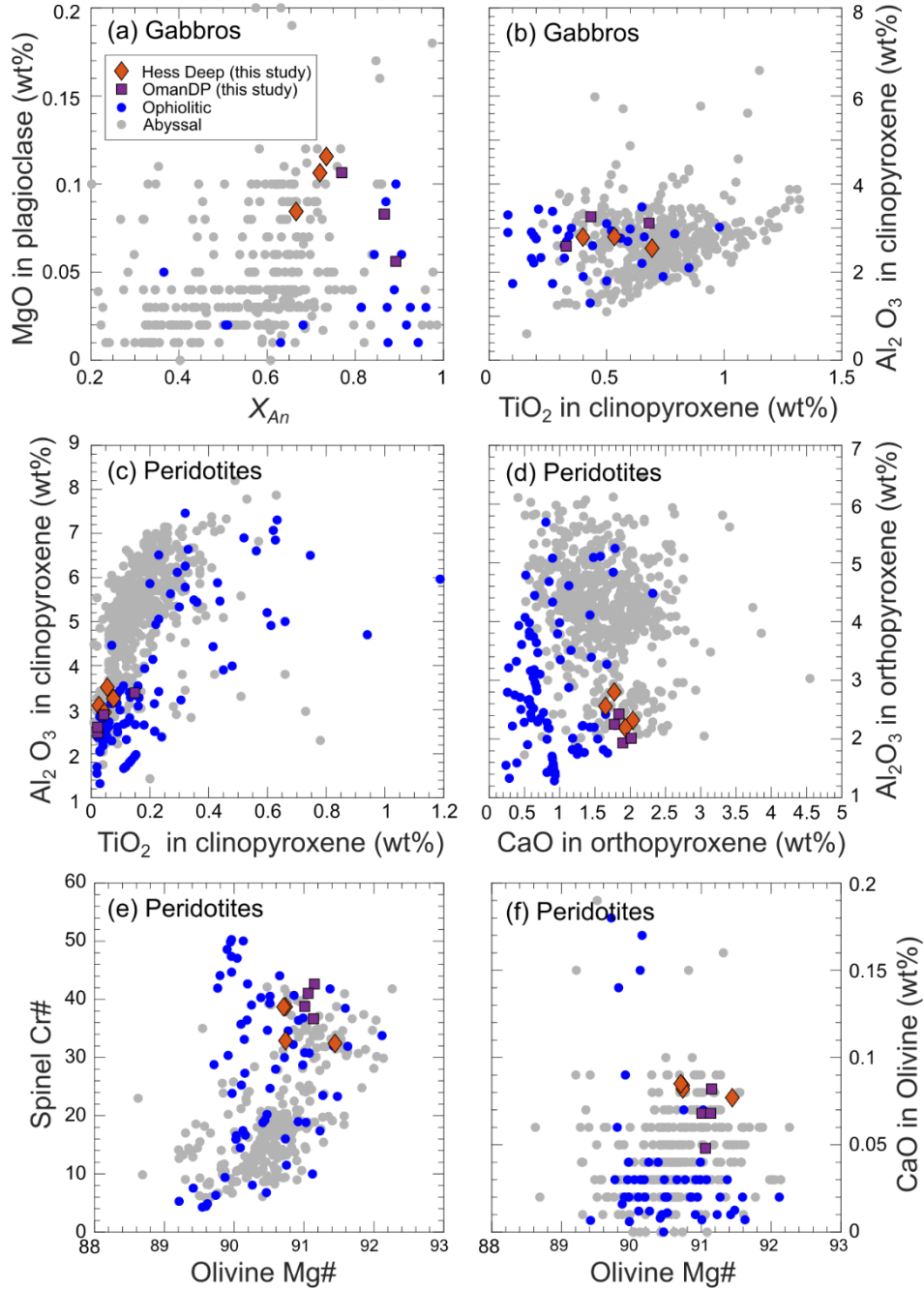


Figure 1.3. Variations in major element compositions of minerals in samples from this study (averages) and the literature. Gabbros are shown in the first row (a, b) and peridotites are shown in the second and third rows (c-f). Samples from this study are shown as orange diamonds (Hess Deep) and purple squares (OmanDP). Ophiolitic gabbros and peridotites from petDB and Dygert et al., 2017, are shown as gray and blue dots, respectively, and abyssal peridotites from Warren, 2016, are shown as gray dots. MgO in plagioclase data shown in (a) and used in thermometric interpretations (this study) were collected by LA-ICP-MS. We note MgO concentrations in the literature data shown in (a) may not have been collected under optimized analytical conditions, perhaps accounting for some of the scatter.

shown as purple squares, and are compared to ophiolitic and abyssal data from the literature (blue and gray circles, respectively). In general, among both gabbros (Figures 1.3a, b) and peridotites (Figures 1.3c-f), mineral compositions for the two localities cluster tightly compared to the global distribution of abyssal and ophiolitic data. In gabbroic plagioclase,  $X_{An}$  ( $Ca/(Ca+Na)$ , in moles) ranges from ~0.65 to 0.9 (Figure 1.3a), while plagioclase MgO abundances plot near the upper end of the global distribution (~0.5-0.12 wt%). In clinopyroxene-saturated systems, partitioning of Mg in plagioclase is known to be temperature dependent, with higher temperatures favoring higher Mg concentrations (Faak et al., 2013; Sun & Lissenberg, 2018a). Slow cooling from magmatic temperatures would promote temperature-dependent exchange (loss) of Mg in plagioclase for Ca with clinopyroxene, while fast cooling from magmatic temperatures would lock in the elevated Mg concentrations associated with magmatic temperatures. Thus, the high MgO abundances observed here may be consistent with relatively fast cooling of the gabbros from high initial temperatures. Gabbroic clinopyroxenes demonstrate a broad range of  $TiO_2$  (0-0.2 wt%) and fall in the middle of the global  $Al_2O_3$  distribution (2-4 wt%, Figure 1.3b). Gabbroic olivines (Table 1.8, not shown in Figure 1.3) have Mg#s ( $Mg/(Mg+Fe)*100$ , in moles) of 74-89 which decrease downsection; all have CaO abundances of ~0.04 wt%.

In peridotitic clinopyroxenes,  $Al_2O_3$  and  $TiO_2$  from both localities cluster at the lower end of the ranges exhibited by ophiolites and abyssal peridotites globally (Figure 1.3c); orthopyroxenes are similarly depleted in  $Al_2O_3$  (Figure 1.3d). Low concentrations of these incompatible minor elements may be attributed to the high extents of melting experienced by these melting residues. CaO in orthopyroxenes is high compared to many other ophiolitic rocks but in the middle of the range of abyssal peridotites (1.5-2.5 wt%, Figure 1.3d). As exchange of CaO between orthopyroxene and clinopyroxene around the pyroxene solvus is temperature dependent, the elevated CaO abundances suggest relatively fast cooling of the Hess Deep and OmanDP peridotites from high initial temperatures (e.g. Brey & Köhler, 1990).

In Figure 1.3e, the Mg# of the peridotitic olivines is compared to the Cr# ( $Cr/(Cr+Al)*100$ ) in spinel. The Mg#s of olivines are consistent with normal values for

peridotitic residues of partial melting (90.7-91.4). The Cr# in spinels (32-43) are near the high end of our compilation, but fall within the distribution of samples from abyssal environments (Cr#s <60), consistent with adiabatic decompression melting in anhydrous settings (e.g. Arai, 1987; Dick & Bullen, 1984). CaO in olivines is approximately 0.05-0.1 wt%, elevated compared to most ophiolitic peridotites but consistent with many abyssal peridotites (Figure 1.3f). (e.g. Köhler & Brey, 1990)

#### *4.1.1 Major element zonation*

Characterization and scrutiny of major element zoning is critical for evaluating the significance of temperatures determined using thermometers (e.g., see Section 5.1), and is described below for gabbros (Hess Deep and then OmanDP), and peridotites (again, Hess Deep and then OmanDP). Major element mineral zonation was evaluated by electron microprobe traverses across representative grains, and/or using representative core and rim analyses.

In all Hess Deep gabbros, significant grain-scale compositional variations in clinopyroxenes and plagioclase are observed. Single plagioclase grains record  $X_{An}$  variations of up to ~0.1. Some clinopyroxenes are zoned in Fe-Mg-Ca, exhibiting near constant Mg#s but significant CaO depletions (up to 10 wt%) in grain rims. These observations are consistent with carefully documented zoning reported in Lissenberg et al. (2013) and Lissenberg & MacLeod (2016) for Hess Deep gabbros, which was attributed to reactive porous flow (we refer the reader to those publications for graphical representations of the zoning patterns described here). In all Hess Deep gabbros,  $Al_2O_3$  is enriched in clinopyroxene rims relative to cores, by up to 4 wt%. In contrast, Hess Deep gabbroic olivines are uniform in composition within analytical uncertainty.

Oman Drilling Project troctolite plagioclase and gabbroic plagioclase and clinopyroxene exhibit little to no zonation. In three samples, major element variations across grains are within analytical uncertainty. In gabbro 5057\_5707A\_032z\_02\_053-056, minor core-rim zonation is observed in clinopyroxenes, with  $Al_2O_3$  variation of 2.8-3.5 wt% from rim to core, and rim-core FeO variations of similar magnitude. Within analytical uncertainty, OmanDP gabbroic olivines are uniform in composition across the grains.

For Hess Deep peridotites, olivines and spinels in all samples are unzoned, within analytical uncertainty. The large clinopyroxene grain in 147\_895D\_3R1\_66-69 (Figure 1.2b), exhibits minor Cr<sub>2</sub>O<sub>3</sub> variations ranging from 1.1 wt% at the rim to 1.4 wt% in the core, clinopyroxenes are otherwise not zoned. Orthopyroxenes are also unzoned, except in sample 47\_895D\_3R1\_22-27, which exhibits minor core-rim CaO zoning, (1.4 wt% at rims to 1.7 wt% in cores). No zoning beyond analytical uncertainty was observed in olivines or spinels.

Oman Drilling Project peridotites exhibit more significant but still minor grain-scale variations. Clinopyroxenes are generally unzoned, but sample 5057\_5708B\_119z\_03\_006-009 exhibits relatively Al<sub>2</sub>O<sub>3</sub> enriched cores (2.9 wt%) trending toward rims depleted by up to 0.5 wt%. All orthopyroxenes exhibit minor Al<sub>2</sub>O<sub>3</sub> and Cr<sub>2</sub>O<sub>3</sub> zoning, with relatively enriched cores (1.9-2.4 wt% Al<sub>2</sub>O<sub>3</sub> and 0.7-0.8 wt% Cr<sub>2</sub>O<sub>3</sub>), and rims depleted by up to 0.5 wt% in Al<sub>2</sub>O<sub>3</sub> and up to 0.3 wt% in Cr<sub>2</sub>O<sub>3</sub>. Two samples (5057\_5708B\_114z\_02\_030-034 and 5057\_5708B\_119z\_03\_006-009) exhibit relatively enriched CaO abundances in grain cores (1.8-2.0 wt%) and depletions of up to 0.5 wt% at rims. Olivines do not exhibit CaO abundance variations beyond analytical uncertainty.

## **4.2 Trace elements**

Average trace element abundances from LA-ICP-MS analysis of clinopyroxenes, orthopyroxenes and plagioclase are reported in Tables 1.9, 1.10, and 1.11 (Attachment Chapter\_1\_Data\_Tables.xlsx) respectively. Chondrite normalized spider diagrams are plotted for mineral averages from all samples in Figure 1.4. Colored lines represent sample averages, while light gray lines represent individual spot analyses. Error bars represent 1 $\sigma$  standard deviations of replicate analyses for each thin section. Here we briefly describe the REE patterns, starting with the gabbros.

Plagioclase from both localities exhibit a positive Eu anomaly (Eu/Eu\*, 10.8 to 14.2 in Hess Deep gabbros and 11.3 to 16.7 in OmanDP gabbros) and steeply dipping light-heavy REE patterns. Heavy REEs (HREEs) are below detection limit in all plagioclase. Some coexisting clinopyroxenes have small negative Eu anomalies in Hess Deep samples (Eu/Eu\* = 0.66 to 1.00), Eu anomalies in OmanDP gabbros are minor or

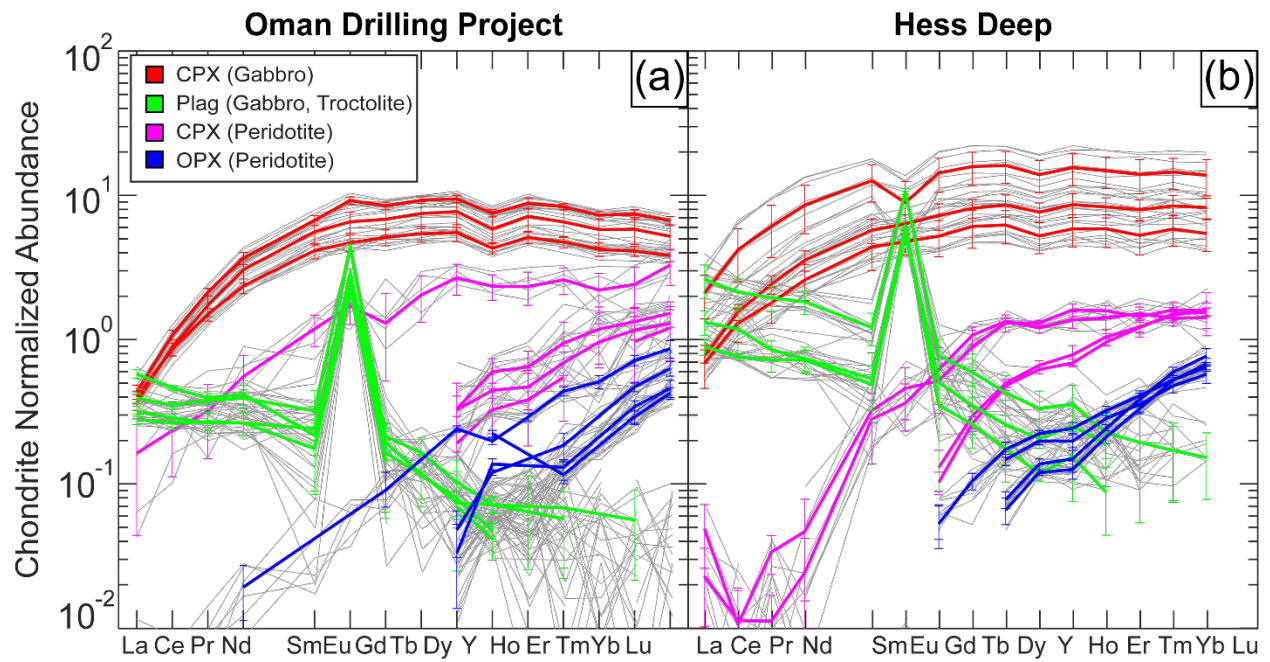


Figure 1.4. Chondrite normalized REE+Y abundances in minerals from the crust and mantle sections of Oman Drilling Project (a) and Hess Deep (b). Individual spot analyses are shown in gray in the background, and sample averages are shown as thicker colored lines, error bars are  $1\sigma$  standard deviations of replicate analyses for each sample. Minerals in crustal samples are green (plagioclase) and red (clinopyroxene), minerals in peridotites are magenta (clinopyroxene) and blue (orthopyroxene).



unresolvable, within analytical uncertainty ( $\text{Eu}/\text{Eu}^* = 0.87$  to  $1.12$ ). Gabbroic clinopyroxenes from both localities have flat mid- to heavy-REE patterns and are strongly light-REE (LREE) depleted. Gabbroic clinopyroxenes from Hess Deep exhibit relatively large standard deviations and trace element variations among spots in individual samples which reflect grain-scale zoning (Figure 1.5), while OmanDP gabbroic clinopyroxenes are homogeneous within analytical uncertainty.

In the peridotites, REE patterns are steeply LREE depleted and below analytical detection limit for many clinopyroxenes and all orthopyroxenes; two Hess Deep samples with resolvable LREEs have spoon-shaped patterns defined by slight enrichments in La relative to Ce. Rare earth element abundances in clinopyroxenes from both localities fall near the depleted end of the global distribution of abyssal harzburgites (e.g. Johnson et al., 1990; Warren, 2016), in agreement with previous analyses of Hess Deep and southern Samail ophiolite peridotites (e.g. Dygert et al., 2017; Hesse et al., 2015). In orthopyroxenes, the REE patterns are sub-parallel to the clinopyroxenes, with abundances  $\sim 0.5$ -1 order of magnitude lower.

#### **4.2.2 Trace element zoning**

Hess Deep gabbros exhibit zoning in plagioclase and especially clinopyroxene. We plot concentration variations across paired mineral grains from a representative sample in Figure 1.5 (spot locations are shown in Figure 1.2a). Elemental abundances vary across grains well beyond analytical uncertainty, as previously documented by Lissenberg et al. (2013) and Lissenberg & MacLennan, 2016. The minor intrasample trace element abundance variations exhibited by Hess Deep peridotites and OmanDP gabbros and peridotites (Figure 1.4) establishes that zoning in those phases and samples is within analytical uncertainty, as representative data were collected from mineral cores and rims whenever possible.

#### **4.3 Temperatures**

Thermometers were applied to the crustal gabbros and mantle peridotites according to mineral assemblages present. Gabbros were investigated using a Ca-in-olivine thermometer (Köhler & Brey, 1990) ( $T_{\text{Ca-in-Ol}}$ ), REE-in-clinopyroxene thermometer (Sun

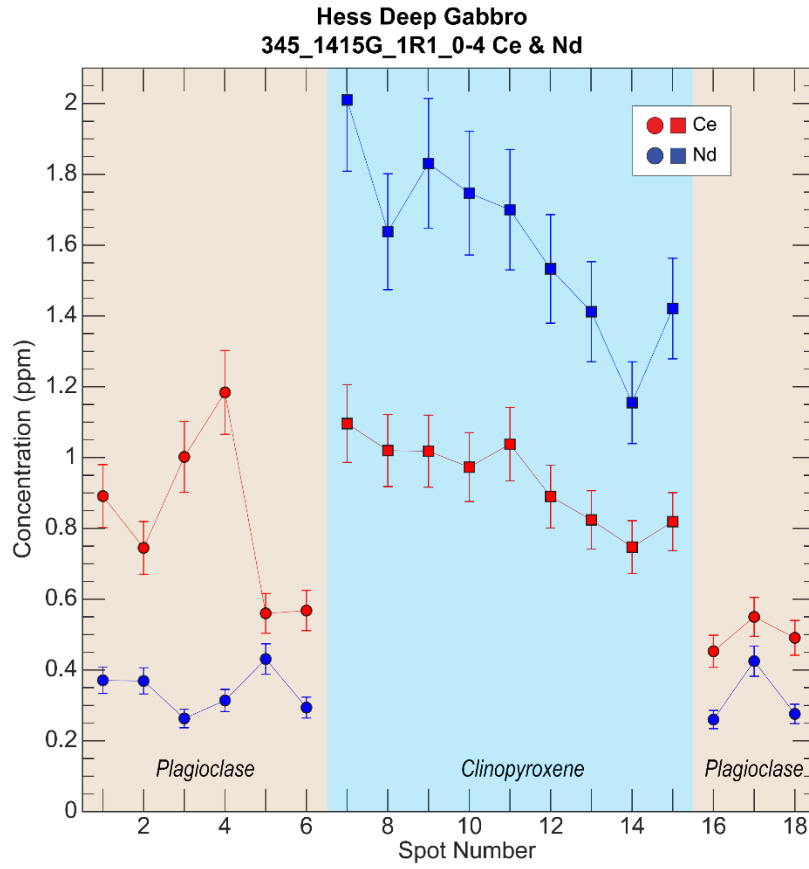


Figure 1.5. Ce and Nd concentrations in paired plagioclase and clinopyroxene grains measured by LA-ICP-MS. Analytical uncertainty (relative) is estimated at 10% of the concentration. Trace element abundances vary beyond the analytical uncertainty in the plagioclase grain on the left and in the clinopyroxene. These variations are representative of Hess Deep gabbros in general, and the variations are interpreted to reflect magmatic processes. See Section 5.1.1 and Lissenberg et al., 2013, and Lissenberg & Macleod, 2016.

& Liang, 2017) ( $T_{REE-in-Cpx-Plag}$ ), and a magnesium-in-plagioclase thermometer (Faak et al., 2014; Sun & Lissenberg, 2018a) ( $T_{Mg-in-Plag}$ ). Peridotites were investigated using the Köhler & Brey, 1990 Ca-in-olivine thermometer and several two-pyroxene solvus thermometers; Brey & Köhler, 1990 ( $T_{BKN}$ ), Wells, 1977 ( $T_{Wells}$ ), Putirka, 1997 ( $T_{Putirka}$ ), a Ca-in-opx solvus-based thermometer, Köhler & Brey, 1990 ( $T_{Ca-in-Opx}$ ), a REE-in-two-pyroxene thermometer (Liang et al., 2013) ( $T_{REE-in-two-Pyroxene}$ ), a thermometer based on exchange of Al and Cr between orthopyroxene and spinel (Witt-Eickschen & Seck, 1991) ( $T_{Al-in-Opx}$ ), and an olivine-spinel thermometer based on Fe-Mg exchange (Fabriès, 1979) ( $T_{Ol-Sp}$ ). Results are presented in Table 1.2 and representative data are shown in Figure 1.6 with samples arranged by proximity to the crust-mantle transition, i.e., the present-day petrologic Moho. Note the sample placement in the figure does not represent absolute or relative distance, but simply a relational proximity to the Moho.

Error bars are estimated  $1\sigma$  uncertainties from scatter in the temperature inversions ( $T_{REE-in-Cpx-Plag}$ ;  $T_{REE-in-two-Pyroxene}$ ), or based on propagation of major element data uncertainty through the thermometers ( $T_{Mg-in-Plag}$ ;  $T_{BKN}$ ;  $T_{Ca-in-Olivine}$ ;  $T_{Al-in-Opx}$ ) (Dyger et al., 2017). Hess Deep gabbros have a  $T_{Ca-in-Ol}$  range of 885-896°C, a  $T_{Mg-in-Plag}$  range of 1046-1071°C (calculated using LA-ICP-MS data) and a  $T_{REE-in-Cpx-Plag}$  range of 1185-1224°C. Oman Drilling Project gabbros have a  $T_{Ca-in-Ol}$  range of 891-893°C, a  $T_{Mg-in-Plag}$  range of 963-1066°C and a  $T_{REE-in-Cpx-Plag}$  range of 1194-1269°C.

Hess Deep peridotites have a  $T_{BKN}$  range of 1048-1141°C, a  $T_{Al-in-OPX}$  range of 978-1041°C, a  $T_{Ca-in-Ol}$  range of 1023-1038°C, a  $T_{Ol-Sp}$  range of 751-787°C, and a  $T_{REE-in-two-Pyroxene}$  range of 1222-1403°C. Oman Drilling Project peridotites have a  $T_{BKN}$  range of 1001-1023°C, a  $T_{Al-in-OPX}$  range of 960-1004°C,  $T_{Ca-in-Ol}$  range of 957-1027°C, a  $T_{Ol-Sp}$  range of 707-775°C, and a  $T_{REE-in-two-Pyroxene}$  range of 1140-1299°C. The  $T_{BKN}$  temperatures are corroborated by similar temperatures obtained using the Wells (1977) and Putirka (1997) two pyroxene-solvus thermometers (Table 1.2). Note that for both localities, for samples from the crust and the mantle, temperatures determined using thermometers based on subsolidus exchange of slower diffusing trivalent elements ( $T_{REE-in-Cpx-Plag}$ ;  $T_{REE-in-two-Pyroxene}$ ) are higher than temperatures determined using thermometers based on exchange of faster diffusing divalent elements ( $T_{Mg-in-Plag}$ ;  $T_{BKN}$ ;

Table 1.2. Temperatures.

Sample	Rock Type	Location	$T_{REE-in-two-Pyroxene}$	$1\sigma$	$T_{REE-in-CPX-Plag}$	$1\sigma$	$T_{Mg-in-Plag}$	$T_{BKN}$	$T_{Wells}$	$T_{Putirk_a}$	$T_{Ca-in-OPX}$	$T_{Al-in-OPX}$	$T_{Ca-in-OI}$	$T_{Ol-Sp}$
345_1415G_1R1_0-4			--	--	1224 <sup>*</sup>	4	1071 <sup>*</sup>	--	--	--	--	--	885	--
345_1415J_4R1_2-6		Hess Deep	--	--	1220 <sup>*</sup>	6	1063 <sup>*</sup>	--	--	--	--	--	--	--
147_894G_9R4_60-67			--	--	1185 <sup>*</sup>	3	1046 <sup>*</sup>	--	--	--	--	--	896	--
5057_5707A_032z_02_053-056	Gabbro		--	--	1194	5	1066	--	--	--	--	--	893	--
5057_5707A_059z_04_004-008		OmanDP	--	--	1238	4	1016	--	--	--	--	--	891	--
5057_5707A_113z_03_036-040			--	--	1269 <sup>†</sup>	10	963 <sup>†</sup>	--	--	--	--	--	893	--
147_895D_3R1_22-27			1287 <sup>‡</sup>	23	--	--	--	1048 <sup>‡</sup>	1041 <sup>‡</sup>	1040 <sup>‡</sup>	1167	1020	1034	754
147_895D_3R1_66-69		Hess Deep	1222 <sup>‡</sup>	53	--	--	--	1069 <sup>‡</sup>	1064 <sup>‡</sup>	1063 <sup>‡</sup>	1188	1041	1023	751
147_895D_5R1_70-76			1357	53	--	--	--	1141	1133	1126	1234	996	1036	787
147_895D_5R1_140-144			1403 <sup>‡</sup>	55	--	--	--	1115 <sup>‡</sup>	1109 <sup>‡</sup>	1103 <sup>‡</sup>	1216	978	1038	760
5057_5708B_100z_03_035-040	Peridotite		1211 <sup>‡</sup>	27	--	--	--	1023 <sup>‡</sup>	1033 <sup>‡</sup>	1038 <sup>‡</sup>	1211	960	1001	707
5057_5708B_114z_02_030-034			1144	30	--	--	--	1001	1002	1023	1203	1004	1027	727
5057_5708B_119z_03_006-009		OmanDP	1299	49	--	--	--	1040	1045	1053	1191	996	1002	764
5057_5708B_124z_02_076-081			1140	18	--	--	--	1023	1031	1041	1232	973	957	775

Peridotite temperatures calculated at 1GPa for consistency among datasets (only affects major element thermometer temperatures, except  $T_{Wells}$ , which are pressure insensitive), gabbros at 2kb.

\*Pyroxenes and plagioclase in Hess Deep gabbros are affected by complex zoning and temperatures may not be meaningful (see Section 5.1.1).

<sup>†</sup>This sample has a temperature distribution beyond Dodson limits for cooling (cf. Sun & Lissenberg, 2018a), suggesting one or more of the temperatures may not be physically meaningful (see Section 5.2.3).

<sup>‡</sup>Rather than being a residual phase, minor clinopyroxene may originate by exsolution from orthopyroxene under subsolidus conditions or crystallization from trapped melt (see Section 5.1.2).

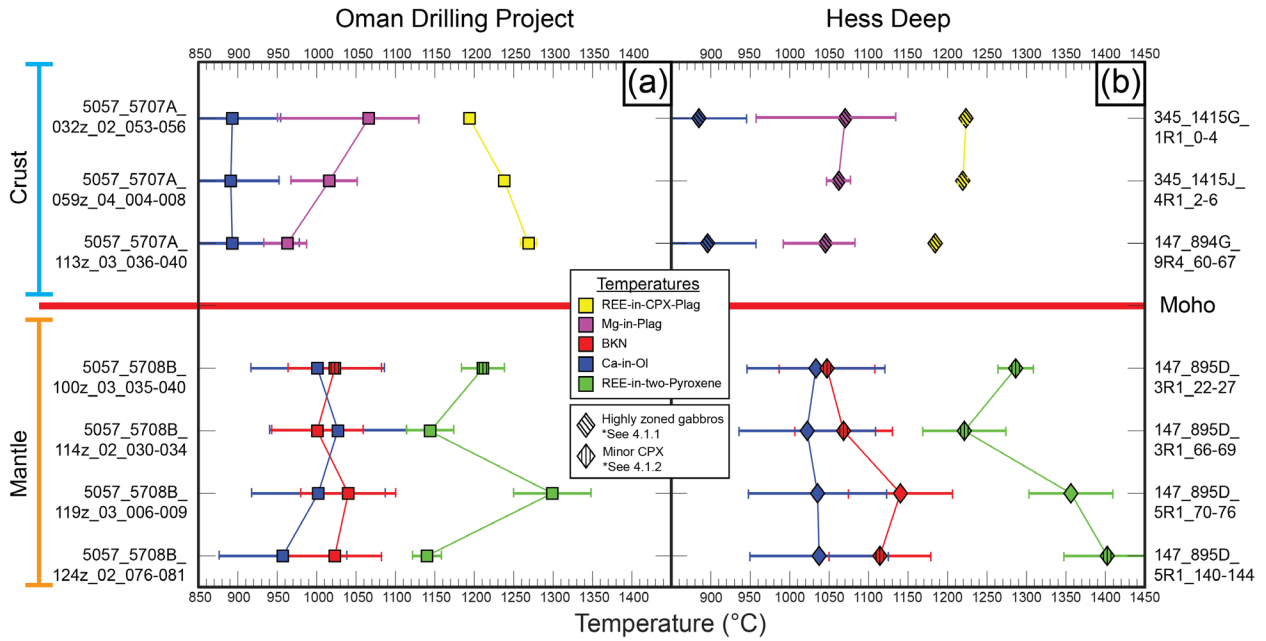


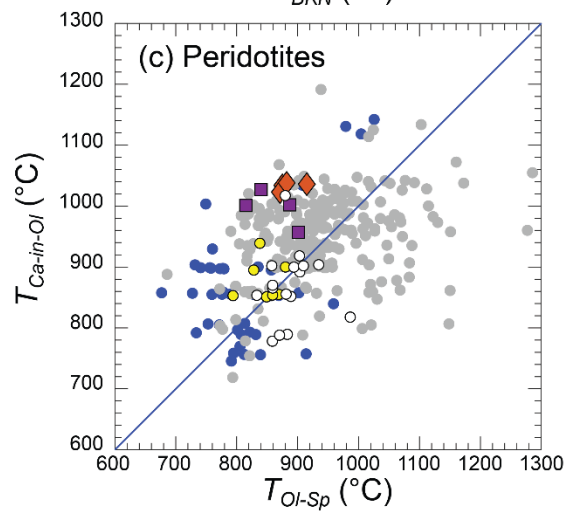
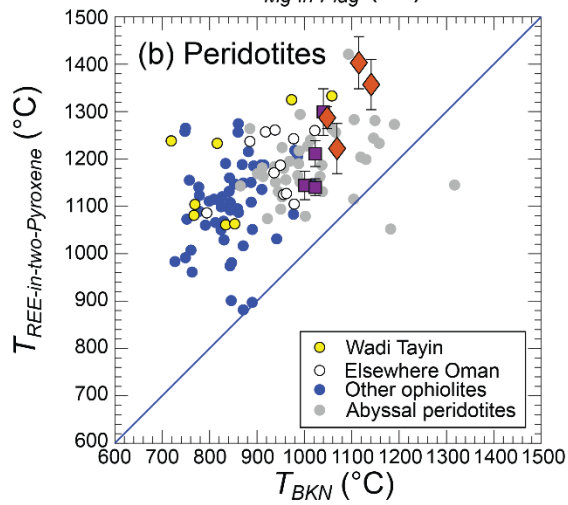
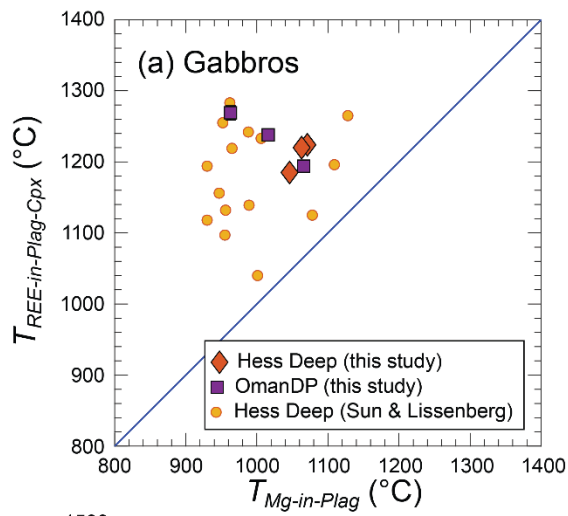
Figure 1.6. Temperature comparison for samples from the Oman Drilling Project (a) and Hess Deep (b) above and below the petrologic Moho, which is indicated by the horizontal red line. In order to compare trends between drilling sites, samples are shown in relational depth, not absolute distance, as Hess Deep peridotites and gabbros cannot be directly related in stratigraphic depth owing to uncertainty in the local structure. For all samples, depths within the holes are reported in Table 1.1. Structural depths of the Oman Drilling Project samples are reported in Table 1.1 and are presented graphically in Figures 1.9 & 1.10. Hess Deep samples are schematically plotted relative to the Moho in Figures 1.9 & 1.10.

$T_{Ca-in-Ol}$ ,  $T_{Ol-Sp}$ ) (an exception being  $T_{Al-in-Opx}$ , which are similar to divalent element-based thermometer temperatures). We note the peridotites investigated here fall outside the calibration dataset of the  $T_{Al-in-Opx}$  thermometer (Witt-Eickschen & Seck, 1991), which was parameterized using peridotites with elevated Al abundances relative to many residual peridotites.

Here we briefly describe the “downhole” trends in the temperature data.  $T_{Ca-in-Ol}$  are higher in peridotites than gabbros, perhaps because of the larger olivine grain sizes (Table 1.3 in Attachment Chapter\_1\_Data\_Tables) and/or higher initial temperatures in the latter.  $T_{REE-in-Cpx-Plag}$  slightly increase with depth at Oman and decrease with depth in the samples from Hess Deep. Within error,  $T_{Mg-in-Plag}$  do not vary with depth. At both localities, peridotite samples show narrowly scattered  $T_{REE-in-two-Pyroxene}$ ,  $T_{BKN}$ ,  $T_{Ca-in-Ol}$ ,  $T_{Al-in-Opx}$ , with no systematic variability with depth for any thermometer. The lack of systematic variability among the samples may reflect their spatial proximity to each other relative to the scale of spatial variations in cooling rate within oceanic lithosphere (Dygert et al., 2017).

The new Hess Deep and OmanDP temperatures are plotted in comparison to other ophiolitic and abyssal peridotites and gabbros in Figure 1.7.  $T_{REE-in-Cpx-Plag}$  are compared to  $T_{Mg-in-Plag}$  in (a); literature data are limited, but the OmanDP and Hess Deep data are similar to temperatures previously recovered from Hess Deep gabbroic lithosphere (Sun & Lissenberg, 2018a).  $T_{REE-in-two-Pyroxene}$  are compared to  $T_{BKN}$  in (b), in all cases, samples from this study have  $T_{REE-in-two-Pyroxene} > T_{BKN}$ , in agreement with temperature distributions previously interpreted to suggest fast cooling for many ophiolitic peridotites ( $\geq 0.01$  °C/y, Dygert & Liang, 2015). Samples from this study plot among the abyssal peridotites, at the high end of the distributions exhibited by ophiolitic peridotites from southern Oman (uppermost Wadi Tayin massif), which cooled at rates  $> 0.1$  °C/y (Dygert et al., 2017, also see Figure 1.8b). In (c),  $T_{Ca-in-Ol}$  are compared to  $T_{Ol-Sp}$ . The new Hess Deep and OmanDP data fall at or above temperatures determined previously for ophiolites. As noted by Dygert et al., 2017, in general, abyssal peridotite temperatures are systematically higher than ophiolitic peridotite temperatures for these thermometers, suggesting faster cooling for abyssal peridotites than ophiolites through closure

Figure 1.7. Temperatures obtained in this study compared to other localities in Oman, previous work on Hess Deep and the global distribution of ophiolites and abyssal peridotites. (a)  $T_{REE-in-Plag-Cpx}$  vs.  $T_{Mg-in-Plag}$  (gabbros), (b)  $T_{REE-in-two-Pyroxene}$  vs.  $T_{BKN}$  (peridotites); (c)  $T_{Ca-in-Ol}$  vs.  $T_{Ol-Sp}$  (peridotites). Temperatures obtained for gabbros are consistent with but at the high temperature end of previous work on Hess Deep (a). Note that samples from this study have high  $T_{REE}$  and  $T_{BKN}$ , consistent with abyssal peridotites and some samples from Oman (b). Peridotite temperatures obtained using fast-resetting thermometers (Ca-in-Olivine and Olivine-Spinel) are at the high end of the global distribution of ophiolites (c), perhaps owing to the close proximity of the samples from this study to the transition zone compared to other ophiolitic peridotites. Data sources are the following: Wadi Tayin, Dygert et al., 2017; Elsewhere Oman (Wadi Fizh, Wadi Thuqbah, Wadi Rajmi, and Wadi Sarami in central and northern Oman; Akizawa et al., 2012, 2016); Other ophiolites, Dygert et al., 2015; Abyssal peridotites, Dygert et al., 2017; Hess Deep, Sun and Lissenberg, 2018.





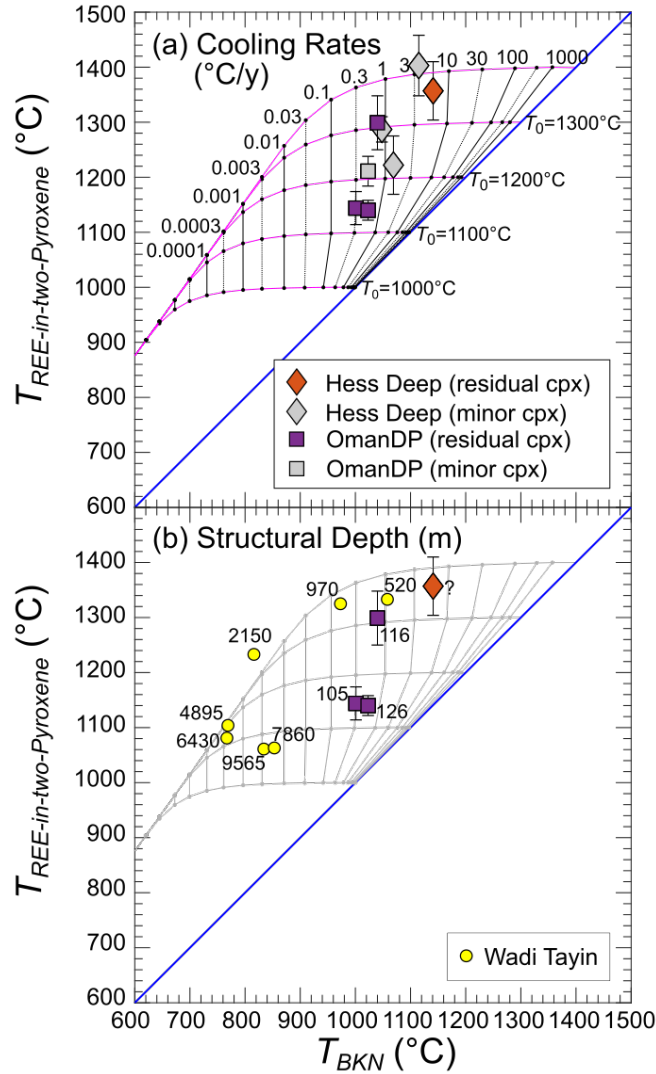


Figure 1.8. Temperatures for Hess Deep and Oman Drilling Project (OmanDP) peridotites compared to models for closure temperature calculated as a function of cooling rate (grid composed of black and magenta lines). (a) Shows samples from this study with colored symbols are interpreted to have retained residual clinopyroxene throughout partial melting, those with gray symbols are interpreted to have exsolved from orthopyroxene under subsolidus conditions, or crystallized from melt during cooling, and thus may not record cooling rates from peak temperatures. The cooling rate grid was calculated utilizing a modified form of the Dodson equation assuming a radius of 0.5 mm (Ganguly & Tirone, 1999, see Dygert & Liang, 2015, for details). The 1:1 line, shown in blue, represents equal temperatures for the two thermometers. Initial temperatures ( $T_0$ ) represent the peak temperatures from which samples cooled, the paths samples take in this temperature space are indicated by the magenta lines extending from initial temperatures along the blue 1:1 line. The near-vertical black lines represent cooling rates in °C/year. Assuming an effective grain radius of 0.5 mm, all samples in this study cooled at rates of 0.3°C/year or faster. Cooling rates calculated using the measured, sample specific grain sizes from samples with residual clinopyroxene are reported in Table 1.3 and shown in Figure 1.9 (blue symbols). (b) Shows samples from (a) with residual clinopyroxene from this study, alongside published samples from Dygert et al., 2017, with structural depths of samples beneath the crust-mantle transition indicated (meters). The question mark indicates that the structural depth of Hess Deep peridotites relative to crust-mantle transition is unknown.

temperature intervals relevant to the thermometers. The proximity of samples investigated in this study to the crust-mantle transition may explain the systematically higher temperatures compared to the overall distribution of the ophiolitic data, which are from a range of structural depths in ophiolites that evolved in a variety of tectonic settings.

## **5. Discussion**

### **5.1 Significance of temperatures**

Thermometers are empirical, semithermodynamic, or thermodynamic models describing temperature-sensitive elemental exchange among a mineral assemblage in a sample. Three types of thermometers applied here are based on (1) exchange of a minor element for major element(s), e.g., Ca-in-olivine and Mg-in-plagioclase thermometers (Köhler & Brey, 1990; Sun & Lissenberg, 2018a); (2) temperature sensitive Ca-Mg-Fe partitioning around the orthopyroxene-clinopyroxene solvus, as in two-pyroxene thermometers (e.g., Brey & Köhler, 1990); and (3) temperature-sensitive REE partitioning between coexisting phases, as in the REE-in-two pyroxene and REE-plagioclase-clinopyroxene thermometers (Liang et al., 2013; Sun & Liang, 2017). The applicability of each thermometer depends on the mineralogy and composition of the sample and the calibration range of the thermometer. To obtain meaningful temperatures, analytical data must be accurate and representative, and the sample must have achieved chemical equilibrium before cooling, and not have been chemically disturbed by metasomatic, melt-rock reaction or other geologic processes that produce disequilibrium at the grain or thin section scales.

With the exception of the Hess Deep gabbros (see Section 5.1.1 below), our new geochemical data meet the aforementioned criteria. The data are accurate (e.g., as demonstrated by replicate analyses of reference material BCR as an unknown, Table 1.4) reproducible (as demonstrated by small standard deviations of replicate analyses, Tables 1.5-1.8), and representative, as major and trace element data were collected across multiple grains in each sample (in many cases, in core-rim traverses). Minerals in peridotites from Hess Deep and OmanDP are minimally zoned, and the slight

depletions in  $\text{Al}_2\text{O}_3$ ,  $\text{Cr}_2\text{O}_3$  and CaO in pyroxene rims are consistent with subsolidus exchange between pyroxenes and with spinel during cooling (e.g. Dygert et al., 2016; Takazawa et al., 1996). The OmanDP gabbros are also largely unzoned (see Sections 4.1.1 and 4.2.2). In all samples, REE abundances and LREE depletion are consistent with adiabatic decompression melting rather than metasomatic interactions that could perturb REE-based temperatures (e.g. Johnson et al., 1990; Navon & Stolper, 1987). We note that the slightly elevated La abundances in two Hess Deep peridotites (Figure 1.4) are excluded from temperature determinations (a summary of the inversion diagrams used to obtain  $T_{\text{REE-in-two-Pyroxene}}$  and  $T_{\text{REE-in-CPX-Plag}}$  temperatures is presented in Figure 1.12 in Appendix 1; see Liang et al., 2013 and Sun & Liang, 2017, for a description of the methods). These observations all support interpretation of the Hess Deep and OmanDP peridotite and OmanDP gabbro temperatures as bulk (mineral average) closure temperatures, i.e., temperatures locked in by the effective cessation of an exchange reaction during cooling (see Section 5.2).

#### *5.1.1 Hess Deep gabbros may not record meaningful cooling rates*

Previously, workers interpreted chemical variations in Hess Deep gabbros as reflecting reactive transport of melts through crystal mushes in the lower oceanic crust (e.g. Lissenberg et al., 2013; Lissenberg & MacLeod, 2016), and suggested that averaged mineral compositions reflect “bulk closure,” such that their thermal histories could be quantified (Sun & Lissenberg, 2018a). Hess Deep gabbros exhibit complex grain-scale elemental heterogeneity beyond analytical uncertainty, inconsistent with subsolidus exchange during monotonic cooling (e.g., Section 4.1.1; Figure 1.5). While the cooling rates obtained in Sun & Lissenberg (2018a) are consistent with previous investigations into cooling of oceanic lithosphere (e.g., Dygert et al., 2017; Dygert & Liang, 2015; VanTongeren et al., 2008), many of the temperatures (up to  $\sim 1300^\circ\text{C}$ ) are higher than clinopyroxene and plagioclase cosaturation temperatures for dry, primitive, mid-ocean ridge basalts (e.g., Grove and Bryan, 1983; Villiger et al., 2004). The proposition that chemical variations in unequilibrated pyroxene and plagioclase in a reacting, open system can be interpreted as recording a thermal history is questionable. Faak et al. (2015) and Faak & Gillis (2016) used chemical variations across minerals

obtained in line traverses and applied Ca-in-olivine and Mg-in-plagioclase thermometers and speedometers to compositional profiles. The latter approach would similarly produce misleading apparent thermal histories from samples that failed to attain equilibrium after fractional crystallization and melt-rock reaction, and also in samples where grains are chemically disturbed by alteration. Because the grain-scale heterogeneity in major and trace elements in plagioclase and clinopyroxene in our Hess Deep gabbro samples demonstrates that they failed to attain chemical equilibrium, we report apparent  $T_{Mg-in-Plag}$ ,  $T_{REE-in-CPX-Plag}$  and  $T_{Ca-in-Ol}$  obtained from these data in Tables 1.2 and 1.3 and Figures 1.6 and 1.7, but refrain from presenting the apparent (0.02-0.44 °C/y) gabbroic cooling rates calculated using the temperatures in Figures 1.9 and 1.10. As lithospheric cooling at Hess Deep is constrained by the peridotites underlying the gabbros, this has little effect on our conclusions.

#### *5.1.2 Some peridotites may not provide a record of cooling from peak temperatures*

To obtain information on a sample's thermal history after achieving a peak temperature, stability of the phases the thermometer is based on throughout the cooling history is required. This requirement may be violated for highly depleted peridotites, where clinopyroxene is exhausted by extensive partial melting (e.g. Pirard et al., 2013). In such cases, small clinopyroxene grains may exsolve from orthopyroxene at subsolidus temperatures owing to orthopyroxene unmixing along the solvus. Alternatively, minor clinopyroxenes may crystallize from small pools of silicate melt during cooling (e.g., Hanghøj et al., 2010). Application of two-pyroxene thermometers to such samples may produce temperatures that reflect subsolidus cooling (e.g., Dygert et al., 2017), or spurious thermal histories, rather than cooling from peak temperatures. Here, we considered the potential for clinopyroxene exhaustion by visual inspection (e.g., Figure 1.2; c; e; f), and using the mineral modes reported in core descriptions, which are summarized in Table 1.3. In cases where the clinopyroxene are small and scarce, and the clinopyroxene/orthopyroxene mode ratio is less than 0.05 (cf. Dygert et al., 2017), we infer that the minor clinopyroxene present may not be representative of cooling from peak temperature. We report the  $T_{BKN}$  and other solvus thermometer temperatures and  $T_{REE-in-two-Pyroxene}$  temperatures obtained from these samples (flagged

using gray symbols in Figure 1.8a), and report the apparent cooling rates in Table 1.3, but exclude presentation of the rates determined using these data from Figures 1.9 and 1.10. After this exercise, cooling rates from peak temperature for four peridotites remain (three OmanDP samples and one Hess Deep sample). We infer that thermal histories provided by the Köhler & Brey (1990) Ca-in-olivine thermometer are not afflicted by this issue, as Ca exchange between clinopyroxene and olivine is rapid (Coogan et al., 2005), such that the Ca-in-olivine thermometer records thermal conditions at low subsolidus temperatures (e.g., Figure 1.7c) where the clinopyroxene in the samples was present.

## 5.2 Cooling Rates

Temperatures recorded by thermometers reflect rate-limited, time-dependent exchange reactions that occur during cooling. For samples that cool at rates relevant to geologic processes such as tectonic exhumation, thermometers based on relatively rapid exchange of divalent elements (e.g., the Ca-in-olivine thermometer of Köhler & Brey, 1990) record lower, subsolidus temperatures than thermometers based on trivalent elements (e.g., the REE-based thermometers, Liang et al., 2013; Sun & Liang, 2017), explaining the range of temperatures exhibited by our samples (Figure 1.6). The faster a rock cools, less spread in temperature will be seen among thermometers that respond to cooling at different rates (and vice versa). If exchange rates relevant to a given thermometer are known, closure temperature models can be applied to quantify the rate at which diffusive exchange of the element(s) the thermometer relies on effectively ceased. A widely used closure temperature model is described by the Dodson equation (Dodson, 1973):

$$\frac{-ART_c^2 D_0}{E \exp\left(\frac{E}{RT_c}\right) a^2} = \frac{dT}{dt} \quad (1),$$

where  $T_c$  is the temperature provided by the thermometer (which must be established as a closure temperature, see Section 5.1),  $E$  and  $D_0$ , are the activation energy and pre-exponential factors for the element of interest, respectively;  $R$  is the gas constant,  $A$  is a geometric constant (in this study we assumed spherical geometry ( $A=55$ )), and  $a$  is an

effective grain size. The Dodson equation makes simplifying assumptions that may or may not be justified depending on the exchange reaction considered and the geologic history of a sample, among them, continuous cooling from peak temperature at a constant rate, diffusive exchange between a mineral grain and a semi-infinite reservoir, and the lack of any grain growth (or resorption) during cooling. These assumptions may be justified for simple exchange reactions, e.g., the Köhler & Brey (1990) Ca-in-olivine thermometer, where the Ca-Fe-Mg exchange reaction between olivine and clinopyroxene is well understood, and the kinetics are constrained (e.g. Coogan et al., 2005; Jurewicz & Watson, 1988).

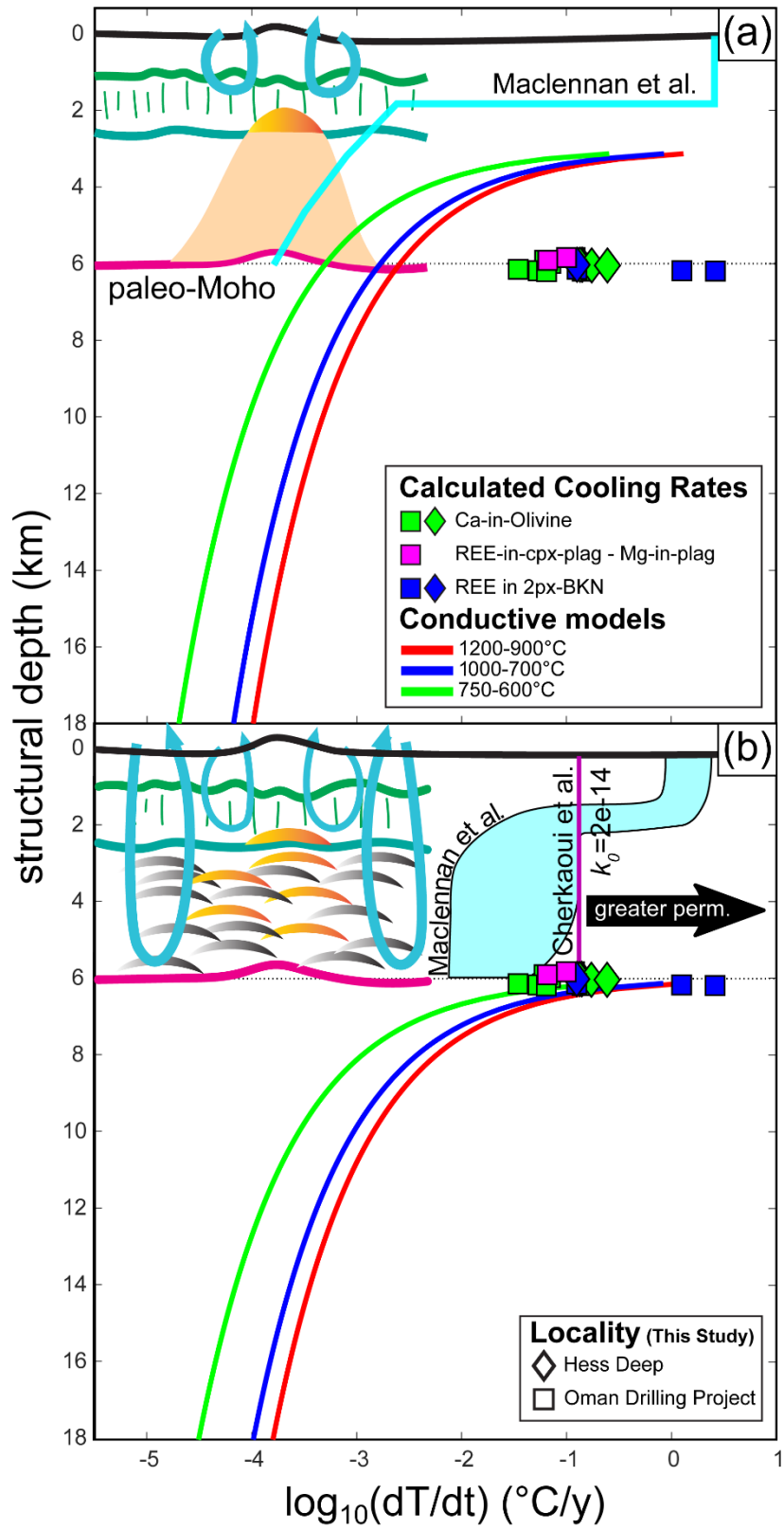
### *5.2.1 Rates from Ca-in-olivine temperatures*

Using Equation 1 and olivine grain sizes measured petrographically (see Section 2.1), we calculated cooling rates from the  $T_{Ca-in-Ol}$  data, which range from 0.06 to 0.12 °C/y for the OmanDP gabbros, and 0.03 to 0.25 °C/y for the Hess Deep and OmanDP peridotites (Table 1.3, green symbols, Figure 1.9). Serpentinization of olivine rims could inflate these rates by removing the portion of the grain exhibiting Ca depletion after exchange with clinopyroxene during cooling. Underestimating grain size would also inflate the cooling rates, because the rates scale with the square of grain size (Equation 1). Grain sizes a factor of two larger than the values we measured would produce cooling rates a factor of four slower, which is still ~2 orders of magnitude faster than rates anticipated in a scenario where the lower crust and underlying mantle cooled conductively (e.g. Dygert et al., 2017; Faak & Gillis, 2016).

### *5.2.2 Rates from REE-in-two-pyroxene temperatures and pyroxene solvus temperatures*

Application of Equation 1 to  $T_{REE-in-two-Pyroxene}$  is less straightforward, as the thermometer relies on exchange of multiple elements with differing diffusion rates between phases. Yao & Liang (2015) explored this problem numerically; Liang (2015) developed a generalized closure temperature equation for biminerals systems. The studies found that unless the clinopyroxene mode is less than 5% that of orthopyroxene, clinopyroxene can be treated as an effectively infinite reservoir for REEs, and diffusion in orthopyroxene rate limits REE exchange between two pyroxenes (see Table 1.3 for

Figure 1.9. Comparison between cooling rates obtained from samples in this study (green, magenta and blue diamonds and squares) and modeled conductive cooling rates for three temperature intervals (red, blue and green lines, 1200-900°C, 1000-700°C, and 750-600°C, respectively). Insets show cartoons reflecting the relevant crustal accretion mechanism and cooling regime assumed for each panel. A Gabbro Glacier scenario is shown in (a), with conductive cooling starting at the dike-gabbro transition, beneath which hydrothermal circulation does not extend. A hydrothermal model from Maclennan et al., 2005, is shown for comparison, which assumes a thinner extrusive section and lower thermal diffusivity compared to models from this study. A Sheeted Sills scenario is shown in (b), which assumes convective cooling by hydrothermal circulation throughout the entire crustal column, and conductive cooling beneath the Moho. The sample-based cooling rates obtained in this study are shown at their approximate depths relative to the Moho, and are the same in both panels. Note the sample-based cooling rates obtained from three independent thermometric and geospeedometric methods (Dodson, 1973; Dygert & Liang, 2015; Sun & Lissenberg, 2018a) are in agreement, and that the rates are consistent for samples above and below the Moho at both localities. The rates obtained in this study are significantly higher than rates predicted in a Gabbro Glacier scenario (a), but consistent with deep hydrothermal circulation and convective cooling throughout the gabbroic section, as in a Sheeted Sills scenario (b). A model of hydrothermal cooling of the crust is shown as a vertical purple line in (b) for a reference permeability ( $k_0$ ) of  $2 \times 10^{-14}$  (Cherkaoui et al., 2003), the black arrow indicates that as crustal permeability increases, the cooling rate in the crust would correspondingly increase. Predicted cooling rates from published conductive-hydrothermal hybrid scenarios and a gabbro glacier scenario with concomitant off-axis hydrothermal circulation (blue field, Maclennan et al., 2005) are ~1 order of magnitude slower than rates obtained from our samples, implying that hydrothermal cooling efficiency exceeded ~80 kW/m.





relative pyroxene modes in rocks from this study). Experimental work has demonstrated that within analytical uncertainty, diffusion rates are uniform among REEs in orthopyroxene (Cherniak & Liang, 2007). Dygert & Liang (2015) developed a method to extract rates from  $T_{REE-in-two-Pyroxene} - T_{BKN}$  using a modified form of Equation 1 (Ganguly & Tirone, 1999). This method assumes  $T_{BKN}$  are effectively modeled using diffusivities for Fe-Mg interdiffusion in diopside (Dimanov & Wiedenbeck, 2006), and provides an average cooling rate through the temperature interval recorded by the two thermometers. The initial or peak temperature the sample cooled from can also be constrained.

Using the aforementioned methods, and assuming an average grain radius for the peridotite samples of 0.5 mm (Figure 1.2; Mevel et al., 1996), we produced a net of cooling-rate dependent closure temperatures overlaid on the  $T_{BKN}$  and  $T_{REE-in-two-Pyroxene}$  data (Figure 1.8). Samples potentially affected by low pyroxene modes (see Section 5.1.2) are shown in gray, samples with clinopyroxene interpreted to be residual after partial melting and cooling from peak temperatures are shown with colored symbols. Cooling rates scaled to the measured grain sizes are reported in Table 1.3, and range from 0.13 to 2.6 °C/y, from apparent peak or initial temperatures of ~1150 to ~1350°C. Interestingly, the OmanDP samples have similar or lower initial temperatures than the Hess Deep sample. The rates are highly consistent with those determined from  $T_{Ca-in-Ol}$ , previous determinations for samples from the oceanic crust and uppermost mantle lithosphere (e.g., Canil et al., 2019; Dygert et al., 2017; Mock et al., 2021; Sun & Lissenberg, 2018a; VanTongeren et al., 2008), and are 2-3 orders of magnitude faster than a scenario where the overlying lower crustal section is cooled conductively. The rates are plotted as blue squares in Figure 1.9.

### *5.2.3 Rates from REE-in-clinopyroxene-plagioclase temperatures and Mg-in-plagioclase temperatures*

Cooling rates for the gabbros were calculated using the coupled  $T_{Mg-in-Plag} - T_{REE-in-Cpx-Plag}$  speedometer of Sun & Lissenberg, 2018a, which leverages numerical solutions to a biminerally formulated diffusion equation, in order to determine a cooling rate and initial temperature (assuming spherical geometry). The speedometer takes mineral

composition, grain size, and mineral modes into account, and is applicable to average mineral compositions as provided by our dataset. The model of Sun & Lissenberg (2018a) was parameterized using a larger calibration dataset and leverages a more generalized silica activity model than that of Faak et al. (2013; 2014). Additionally, it does not rely on the presence of exchange-related grain-scale concentration gradients which may be absent depending on kinetics, grain size and cooling rate, making it more broadly applicable to oceanic gabbros. We refrain from commenting further on other respective advantages and disadvantages of the Faak et al., (2014) and Sun & Lissenberg, (2018a) speedometers for oceanic gabbros, as they are thoroughly described in the commentary of Faak et al., 2018 and reply of Sun & Lissenberg, 2018b. (However, see Section 5.1.1, for a brief discussion of potential issues associated with determining temperatures and cooling rates from samples with complex open-system geologic histories, which would afflict both speedometers).

Cooling rate inversion diagrams are presented in the electronic supplement (Figure 1.12), and cooling rates (for the OmanDP samples only, see Section 5.1.1) are reported in Table 1.3. Perhaps owing to analytical scatter or the sample's geologic history, one of the three OmanDP gabbros (5057\_5707A\_113z\_03\_036-040) has a  $T_{REE-in-Cpx-Plag}$  and  $T_{Mg-in-Plag}$  temperature distribution beyond the physically reasonable Dodson limit (cf., Sun & Lissenberg, 2018a); for this sample no rate can be determined. Rates for the other OmanDP gabbros are 0.1 and 0.07 °C/y, consistent with rates determined using the  $T_{REE-in-two-Pyroxene} - T_{BKN}$  and  $T_{Ca-in-Ol}$ -based methods described in Sections 5.2.1 and 5.2.2. The  $T_{REE-in-Cpx-Plag} - T_{Mg-in-Plag}$  rates are plotted as magenta squares in Figure 1.9.

### **5.3 Implications for cooling and crustal accretion mechanisms**

In Figure 1.9, cooling rates obtained from thermometric data are compared to conductive cooling models relevant to Gabbro Glacier and Sheeted Sills scenarios. Only the cooling rate data we interpret as most physically meaningful are compared to the models (see Sections 5.1 and 5.2), however, we note that the apparent rates from samples flagged because of grain scale heterogeneity or minor clinopyroxene mode are consistent with our general observations (Table 1.3). Despite the fact that reliable cooling rates cannot be recovered from Hess Deep gabbros, because their thermal

histories must be intimately related to underlying peridotites, the peridotites place important constraints on cooling of the oceanic crust beneath the East Pacific Rise.

Our cooling models assume conductive cooling of the lithosphere into a cold thermal boundary layer and are constructed using a half-space solution to the one-dimensional heat conduction equation (Equation 4-125, Turcotte and Schubert, 2002):

$$T = (T_1 - T_0) \times \operatorname{erf} \left( \frac{z}{2\sqrt{\kappa t}} \right) + T_0 \quad (2).$$

where  $T_1$  is the uniform initial temperature of the lithosphere and  $T_0$  is the temperature at the rock–seawater interface;  $z$  is the depth into the conductive profile;  $t$  is time; and  $\kappa$  is thermal diffusivity ( $10^{-6} \text{ m}^2/\text{s}$ ). Here we assume an initial temperature of  $1250^\circ\text{C}$ , close to (but slightly higher than) plagioclase and clinopyroxene cosaturation temperatures for dry MORBs (e.g., Grove & Bryan, 1983; Villiger et al., 2004), and between the REE-based temperatures obtained from the peridotites and gabbros (Table 1.2). Figure 1.9 shows average cooling rates calculated using Equation 2 through temperature intervals relevant to the thermometers applied in this study. In the Gabbro Glacier scenario (Figure 1.9a) and the Sheeted Sills scenario (Figure 1.9b), the lithosphere starts with a uniform initial temperature at all depths but the conductive cooling regime underlying the hydrothermal section of the lithosphere is shallower or deeper depending on the vertical extent of hydrothermal cooling due to sea-water circulation. In a Gabbro Glacier scenario, the extrusive section of the crust is hydrothermally cooled, and the gabbroic section of the crust and underlying peridotites cool conductively (Figure 1.9a). In a Sheeted Sills scenario, the peridotites underlying the crustal section are conductively cooled, and the entire overlying crustal section is hydrothermally cooled.

A Gabbro Glacier scenario would produce a dramatic decrease in cooling rate with depth starting immediately beneath the extrusive section. A Sheeted Sills scenario produces the same rates at greater depth, with cooling above the Moho dominated by convection (Figure 1.9b). For reference, Figure 1.9b also shows a convective cooling model for the entire crust assuming a reference permeability of  $2 \times 10^{-14}$  (Cherkaoui et al., 2003); higher permeabilities would produce faster cooling rates in the crustal section. Conductive-hydrothermal hybrid models from Maclennan et al., (2005), based on the model formulation of Maclennan et al., (2004), are also shown in Figure 1.9b,

and in Figure 1.9a, their model assuming conductive cooling for a lower thermal diffusivity and thinner extrusive crust than our model is shown.

At a given depth, the measured peridotitic and gabbroic cooling rates are much faster than the predicted cooling rates in the Gabbro Glacier scenario while in a Sheeted Sills scenario, the predicted cooling rates agree with rates from the geochemical data obtained in this study (0.02 - 2.6 °C/y), for temperature intervals relevant to the thermometers. We note these rates are consistent among three independent geospeedometric methods based on five independent thermometers. We conclude that the new geospeedometric results are inconsistent with a Gabbro Glacier-type scenario, and instead support hydrothermal cooling of the entire crustal section beneath the ridge axis for rocks recovered at Hess Deep and Wadi Zeeb, Oman, consistent with a Sheeted Sills scenario for accretion of oceanic crust. The ~1 order of magnitude discrepancy between models of MacLennan et al. (2005) and our results suggests that hydrothermal cooling efficiency exceeded ~80 kW/m throughout the crust at Hess Deep and Wadi Zeeb.

#### ***5.4 Comparison with previous thermometric investigations***

Our new cooling rates were calculated using methods that rely on closure temperatures determined from averaged mineral compositions (Dodson, 1973; Dygert and Liang, 2015; Sun and Lissenberg, 2018a). Several authors took an alternative approach and applied diffusion models to geochemical profiles obtained from grain-scale electron microprobe traverses, to invert rates from spatial variations (or lack thereof) in concentration (e.g., Coogan et al., 2002; Coogan et al., 2007; Faak and Gillis, 2016; Mock et al., 2021). To facilitate direct comparison with our new results, we recalculated Ca-in-olivine rates using data from Coogan et al., 2002, Coogan et al., 2007, and Faak and Gillis, 2016, using the average-based methods we employed to evaluate our own data. Redetermining rates from Mg-in-plagioclase data was not possible, as the mineral average-based Sun and Lissenberg, 2018a speedometer takes mineral modes and grain size information into consideration, and requires knowledge of coexisting clinopyroxene composition, information that was not reported in the studies of Faak et al., 2015 or Faak and Gillis, 2016. The recalculated Ca-in-olivine rates are

similar to, but in some cases, faster than the rates determined in the data sources (Figure 1.13 in Appendix 1), on average, 1.4 and 1.6 log units faster than the published rates (for the data of Coogan et al., 2002, and Faak & Gillis, 2016, respectively).

The recalculated Ca-in-olivine rates, our new results, and previously published cooling rates from mid-ocean ridge type spreading centers (Dygert et al., 2017; Sun and Lissenberg, 2018a; VanTongeren et al., 2008) are compared in Figure 1.10 (data from mid-ocean ridge spreading centers, or ophiolites with mid-ocean ridge tectonic affinity only). Samples from spreading centers with typical 6 km thick crust are shown in (a) (OmanDP crust and mantle, Wadi Tayin, Samail ophiolite crust and mantle sections, and Hess Deep crust and mantle, Dygert et al., 2017; Faak and Gillis, 2016; Sun and Lissenberg, 2018a; VanTongeren et al., 2008), samples from localities with thinner crustal sections are shown in (b) (Wadi Abyad, Samail ophiolite and the Atlantis Bank of the Southwest Indian Ridge (SWIR), Coogan et al., 2002; Coogan et al., 2007). Also shown are conductive and hydrothermal cooling models described in Section 5.3, in a Sheeted Sills scenario in (a) and a Gabbro Glacier scenario in (b) (the corresponding alternative cooling profiles are shown in gray in both panels).

Cooling rates from the three localities represented in (a) are fast and uniform with depth in the crustal section and across the transition zone, and at Wadi Tayin, systematically decrease with depth moving into the mantle section, consistent with hydrothermal cooling of the crust and conductive cooling of the mantle, as in a Sheeted Sills scenario. A similar systematic decrease in cooling rate with increasing depth beneath the paleo-Moho was also observed by Canil et al., 2019, at an ophiolite with probable supra-subduction zone tectonic affinity.

We note that a systematic decrease in cooling rate in Hess Deep and Pito Deep gabbros directly beneath the dike-gabbro transition (i.e., in rocks formed in an axial magma lens, Figure 1.1) was observed by Faak et al. (2015) according to application of Mg-in-plagioclase speedometry (Faak et al., 2014). For reasons mentioned previously we could not recalculate the cooling rates using the Sun and Lissenberg (2018a) speedometer. The gradient in cooling rate observed by Faak et al. (2015) may reflect conductive cooling of the axial magma lens immediately beneath the dikes, while the

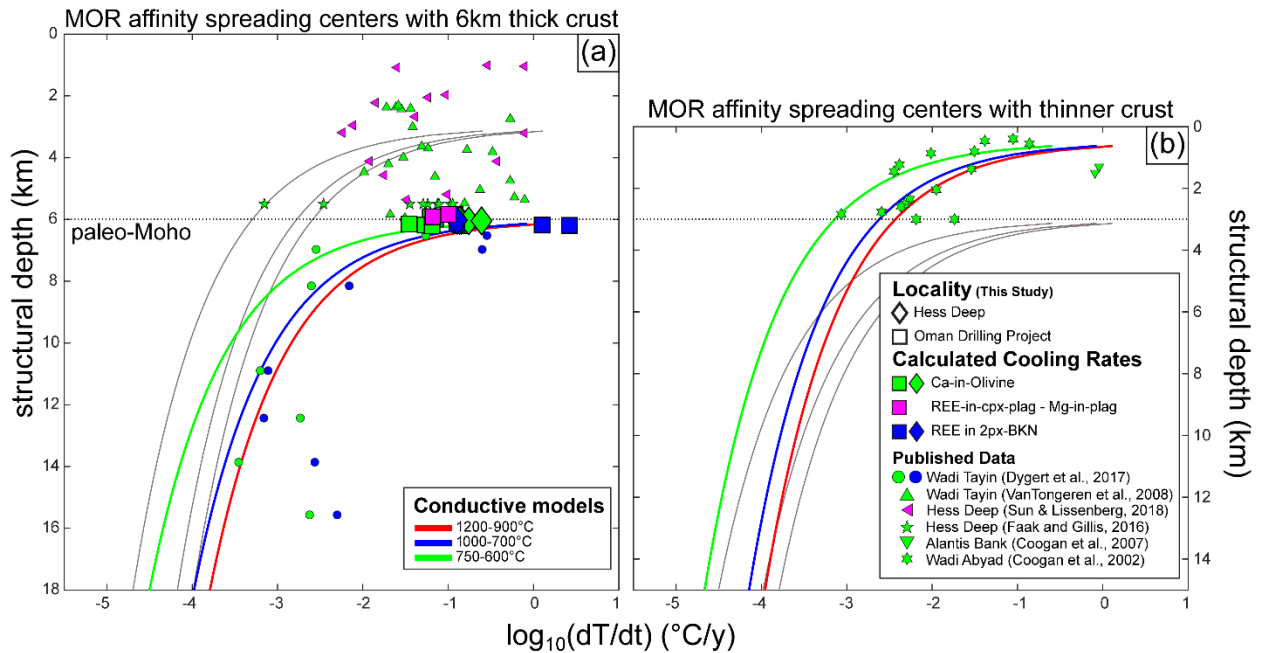


Figure 1.10. Cooling rates from this study (Hess Deep, diamonds, OmanDP, squares) compared to rates gathered from the literature that were calculated using the methods we employed (Dyger et al., 2017; Sun and Lissenberg, 2018a, VanTongeren et al., 2008), or recalculated using those methods (Coogan et al., 2002; Coogan et al., 2007; Faak and Gillis, 2016) (smaller symbols), plotted against structural depth. Symbol color corresponds to speedometric method (see legend). Conductive cooling models are also shown (see Section 5.3 and caption to Figure 1.9 for details). All samples originate from oceanic spreading centers or ophiolites with mid-ocean ridge tectonic affinity. Samples from localities with “normal” 6km thick crust are shown in (a), samples with thinner crust are shown in (b). Data from Faak and Gillis (2016) and the Atlantis Bank (Coogan et al., 2007) are placed at an arbitrary depth in the lower crustal section. The observations support hydrothermal cooling of oceanic lower crust at Hess Deep, Wadi Zeeb (OmanDP), Wadi Tayin, and the SWIR (Atlantis Bank). Samples from Wadi Abyad (Coogan et al., 2002) support conductive cooling of the lower oceanic crust. The gray lines in the background correspond to thermal scenarios lacking convective cooling beneath the extrusive section in (a) and with convective cooling extending to the crust-mantle boundary in (b).

underlying gabbros were cooled hydrothermally by a fracture network that drew in cold seawater from off axis (Figure 1.1b, also see cartoons in Garrido et al., 2001 and Sun and Lissenberg, 2018a).

In Figure 1.10b, data from Wadi Abyad data are shown, which exhibit a continuous and systematic decrease in cooling rate with depth. These data are well matched by models that assume conductive cooling of the entire lower oceanic crust, as in a Gabbro Glacier scenario. The two data points from the SWIR (placed at an arbitrary depth within the lower crust) are in better agreement with hydrothermal cooling throughout the SWIR lower crustal section.

Cooling rates from four of the five localities (including our new Hess Deep and OmanDP data) are consistent with hydrothermal cooling of the oceanic lower crust. In contrast, the results from Wadi Abyad demonstrate that at least in some places, oceanic lower crust is cooled conductively. This observation implies that controls on hydrothermal vs. conductive cooling (and by implication, crustal accretion mechanisms) could be related to crustal thickness, melt productivity, spreading rate, and/or location along a ridge segment. Cooling rate constraints from other spreading centers are needed to further characterize global variability in lithospheric cooling rates, and to elucidate geologic controls on cooling mechanisms. These constraints would promote a deeper understanding of the conditions under which interactions between the oceans and Solid Earth occur, and the implications for global geochemical cycling across a major interface between the oceans and Earth's interior.

## 6. Summary and Conclusions

We analyzed three gabbros and four harzburgites from IODP Expedition 345 and ODP Leg 147 to Hess Deep, and three gabbros, one troctolite and four harzburgites from IODP Expedition 5057, the Oman Drilling Project (OmanDP), from Wadi Zeeb in the southern Samail ophiolite. After consideration of textural information and grain-scale elemental variations (which are prevalent in Hess Deep gabbros but minor or absent in other samples), we applied thermometers to the gabbros and peridotites using sample averaged compositions. Gabbros were investigated using thermometers based on exchange of REEs ( $T_{REE-in-Cpx-Plag}$ , Sun & Liang, 2017) and Mg ( $T_{Mg-in-Plag}$ , Sun &

Lissenberg, 2018a) between coexisting clinopyroxene and plagioclase, and Ca between olivine and clinopyroxene ( $T_{Ca-in-Ol}$ ). For individual thermometers temperatures were similar between the two localities, and in all cases  $T_{Ca-in-Ol} < T_{Mg-in-Plag} < T_{REE-in-Cpx-Plag}$  ( $T_{Ca-in-Ol}$  are 885-893°C,  $T_{Mg-in-Plag}$  are 963-1071°C;  $T_{REE-in-Cpx-Plag}$  are 1185-1269°C). Peridotites were investigated using thermometers based on exchange of REEs between two pyroxenes ( $T_{REE-in-two-Pyroxene}$ ; Liang et al., 2013), exchange of the diopside component around the two-pyroxene solvus ( $T_{BKN}$ ; Brey & Köhler, 1990), and exchange of Ca for Fe and Mg between olivine and coexisting clinopyroxene ( $T_{Ca-in-Ol}$ ; Köhler & Brey, 1990). Again, for each thermometer, the temperatures are comparable between the two localities, and  $T_{Ca-in-Ol} \lesssim T_{BKN} < T_{REE-in-two-Pyroxene}$  ( $T_{Ca-in-Ol}$  are 957-1038°C;  $T_{BKN}$  are 1001-1141°C;  $T_{REE-in-two-Pyroxene}$  are 1140-1403°C). The magmatic or near-magmatic REE-based thermometer temperatures are interpreted to reflect near-peak temperatures owing to the slow diffusive exchange of trivalent REEs between coexisting phases during cooling, while the lower temperatures recorded by thermometers based on divalent major elements reflect the relatively fast exchange of those elements under subsolidus conditions.

We applied three independent speedometers to the new temperature data. Cooling rates are fast (~0.01 to several °C/y) and consistent among all the Hess Deep and OmanDP samples. A coupled two-pyroxene solvus – REE-in-two-pyroxene speedometer (Dygert & Liang, 2015) recovers rates of 0.1-2.6 °C/y from peak or near-peak temperatures in mantle harzburgites. Application of the Dodson (1973) closure temperature model to  $T_{Ca-in-Ol}$  from the peridotites recovers cooling rates of 0.03-0.81 °C/y, and 0.06-0.12 °C/y from OmanDP gabbros in the crustal section. A coupled Mg-in-plagioclase – REE-in-clinopyroxene-plagioclase speedometer (Sun & Lissenberg, 2018a) recovers rates of 0.07 and 0.1 °C/y from gabbros in the OmanDP crustal section. The similar, fast cooling rates recorded by samples from across the crust-mantle transition zone at the two localities provide insights into the mode of lower crustal accretion beneath fast-spreading mid-ocean ridges, and a window into the thermal histories of an ophiolitic paleo-ridge environment (the Samail ophiolite) and modern mid-ocean ridge environments (Hess Deep). The consistent thermal histories



suggest shared processes of lithosphere formation. The cooling rates were compared to convective and conductive cooling models expected in Gabbro Glacier and Sheeted Sills scenarios for crustal accretion, which invoke shallower and deeper convective (hydrothermal) cooling regimes, respectively. Fast cooling ( $\sim 0.01$  to several  $^{\circ}\text{C}/\text{y}$ ) from magmatic or near-magmatic temperatures at the crust-mantle boundary suggests a network of deeply circulating ocean water extended from the seafloor to the crust-mantle boundary beneath the spreading centers, as expected in a Sheeted Sills-type scenario.

We compared the new cooling rates to those recalculated from previously published data using self-consistent methods, which enables direct comparison among studies. Oceanic lithosphere from four of five localities exhibits cooling rates consistent with hydrothermal cooling of the oceanic lower crust from peak or near-peak temperatures, while one locality is consistent with conductive cooling of the lower crust. We conclude that cooling and crustal accretion mechanisms differ among ridges or locations along ridge segments. New constraints from other spreading centers are needed to further characterize the variability in lithospheric cooling rates, to elucidate geologic controls on cooling mechanisms, and to realize the implications for geochemical cycling between the oceans and Solid Earth.

## **7. Acknowledgments, Samples, and Data**

This work was partly supported by awards to BB from the University of Tennessee NASA Space Grant Consortium, an Alexander Von Humboldt Stiftung to MMJ, and a Postdoctoral Fellowship to ND by the University of Texas at Austin. The authors acknowledge the assistance of Allan Patchen and Nathaniel Miller in collecting major and trace element data. This work would not have been possible without the support and encouragement of the Oman Drilling Project Phase 2 core description party. Measured compositions used to calculate temperatures and replicate analyses of reference material BCR-2G are archived in a Mendeley Data repository at <https://dx.doi.org/10.17632/7rbj8x89th.1>.

## References

- Akizawa, N., Arai, S., & Tamura, A. (2012). Behavior of MORB magmas at uppermost mantle beneath a fast-spreading axis: An example from Wadi Fizh of the northern Oman ophiolite. *Contributions to Mineralogy and Petrology*, 164(4), 601–625. <https://doi.org/10.1007/s00410-012-0762-4>
- Akizawa, N., Tamura, A., Fukushi, K., Yamamoto, J., Mizukami, T., Python, M., & Arai, S. (2016). High-temperature hydrothermal activities around suboceanic Moho: An example from diopside and anorthosite in Wadi Fizh, Oman ophiolite. *Lithos*, 263, 66–87. <https://doi.org/10.1016/j.lithos.2016.07.012>
- Arai, S. (1987). An estimation of the least depleted spinel peridotite on the basis of olivine-spinel mantle array. *Neues Jahrbuch Fur Mineralogie, Monatshefte*, (January 1987), 347–354.
- Boudier, F., & Coleman, R. G. (1981). Cross section through the peridotite in the Samail Ophiolite, southeastern Oman Mountains. *Journal of Geophysical Research: Solid Earth*, 86(B4), 2573–2592. <https://doi.org/10.1029/JB086iB04p02573>
- Braun, M. G. (2004). *Petrologic and microstructural constraints on focused melt transport in dunites and the rheology of the shallow mantle*. Massachusetts Institute of Technology and the Woods Hole Oceanographic Institution. Retrieved from <http://hdl.handle.net/1721.1/29538>
- Brey, G. P., & Köhler, T. P. (1990). Geothermobarometry in Four-phase Lherzolites II . New Thermobarometers , and Practical Assessment of Existing Thermobarometers. *Journal of Petrology*, 31(6), 1353–1378. <https://doi.org/https://doi.org/10.1093/petrology/31.6.1353>
- Canil, D., Grundy, R., & Johnston, S. T. (2019). Thermal history of the Donjek harzburgite massif in ophiolite from Yukon, Canada with implications for the cooling of oceanic mantle lithosphere. *Lithos*, 328–329, 33–42. <https://doi.org/10.1016/j.lithos.2019.01.001>
- Cannat, M., Cann, J., & MacLennan, J. (2004). Some hard rock constraints on the

- supply of heat to mid-ocean ridges. *Geophysical Monograph Series*, 148, 111–149.  
<https://doi.org/10.1029/148GM05>
- Chen, Y. J. (1992). Oceanic crustal thickness versus spreading rate. *Geophysical Research Letters*, 19(8), 753–756. <https://doi.org/10.1029/92GL00161>
- Cherkaoui, A. S. M., Wilcock, W. S. D., Dunn, R. A., & Toomey, D. R. (2003). A numerical model of hydrothermal cooling and crustal accretion at a fast spreading mid-ocean ridge. *Geochemistry, Geophysics, Geosystems*, 4(9).  
<https://doi.org/10.1029/2001GC000215>
- Cherniak, D. J., & Liang, Y. (2007). Rare earth element diffusion in natural enstatite. *Geochimica et Cosmochimica Acta*, 71(5), 1324–1340.  
<https://doi.org/10.1016/j.gca.2006.12.001>
- Coogan, L. A., Jenkin, G. R. T., & Wilson, R. N. (2002). Constraining the cooling rate of the lower oceanic crust: A new approach applied to the Oman ophiolite. *Earth and Planetary Science Letters*, 199(1–2), 127–146. [https://doi.org/10.1016/S0012-821X\(02\)00554-X](https://doi.org/10.1016/S0012-821X(02)00554-X)
- Coogan, L. A., Hain, A., Stahl, S., & Chakraborty, S. (2005). Experimental determination of the diffusion coefficient for calcium in olivine between 900°C and 1500°C. *Geochimica et Cosmochimica Acta*, 69(14), 3683–3694.  
<https://doi.org/10.1016/j.gca.2005.03.002>
- Coogan, L. A., Jenkin, G. R. T., & Wilson, R. N. (2007). Contrasting cooling rates in the lower oceanic crust at fast- and slow-spreading ridges revealed by geospeedometry. *Journal of Petrology*, 48(11), 2211–2231.  
<https://doi.org/10.1093/petrology/egm057>
- Detrick, R. S., Buhl P, Vera E, Mutter J, Orcutt J, Madsen J, & Brocher T. (1987). Multi-channel seismic imaging of a crustal magma chamber along the East Pacific Rise. *Nature*, 326(5), 35–41.
- Detrick, R. S., Harding, A. J., Kent, G. M., Orcutt, J. A., Mutter, J. C., & Buhl, P. (1993). Seismic Structure of the Southern East Pacific Rise, 259(5094), 499–503.

- Dewey, J. F., & Kidd, W. S. F. (1977). Geometry of plate accretion. *Bulletin of the Geological Society of America*, 88(7), 960–968. [https://doi.org/10.1130/0016-7606\(1977\)88<960:GOPA>2.0.CO;2](https://doi.org/10.1130/0016-7606(1977)88<960:GOPA>2.0.CO;2)
- Dick, H. J. B., & Bullen, T. (1984). Chromian spinel as a petrogenetic indicator in abyssal and alpine-type peridotites and spatially associated lavas. *Contributions to Mineralogy and Petrology*, 86(1), 54–76. <https://doi.org/10.1007/BF00373711>
- Dick, H. J. B., Lin, J., & Schouten, H. (2003). An ultraslow-spreading class of ocean ridge. *Nature*, 426, 405–412.
- Dimanov, A., & Wiedenbeck, M. (2006). (Fe,Mn)-Mg interdiffusion in natural diopside: effect of pO<sub>2</sub>. *European Journal of Mineralogy*, 18(6), 705–718. <https://doi.org/10.1127/0935-1221/2006/0018-0705>
- Dodson, M. H. (1973). Closure temperature in cooling geochronological and petrological systems. *Contributions to Mineralogy and Petrology*, 40(3), 259–274.
- Donovan, J. J., Kremser, D., Fournelle, J., & Karsten, G. (2016). Probe for EPMA User's Guide and Reference. *Probe Software, Inc.*
- Dunn, R. A., & Toomey, D. R. (2000). Three-dimensional seismic structure and physical properties of the crust and shallow mantle beneath the East Pacific Rise at 9°30'N. *Journal of Geophysical Research*, 105, 23537–23555. <https://doi.org/10.1029/2000JB900210>
- Dygert, N., & Liang, Y. (2015). Temperatures and cooling rates recorded in REE in coexisting pyroxenes in ophiolitic and abyssal peridotites. *Earth and Planetary Science Letters*, 420, 151–161. <https://doi.org/10.1016/j.epsl.2015.02.042>
- Dygert, N., Liang, Y., & Kelemen, P. B. (2016). Formation of plagioclase Iherzolite and associated dunite-harzburgite-Iherzolite sequences by multiple episodes of melt percolation and melt-rock reaction: An example from the trinity ophiolite, California, USA. *Journal of Petrology*, 57(4), 815–838. <https://doi.org/10.1093/petrology/egw018>
- Dygert, N., Kelemen, P. B., & Liang, Y. (2017). Spatial variations in cooling rate in the

- mantle section of the Samail ophiolite in Oman: Implications for formation of lithosphere at mid-ocean ridges. *Earth and Planetary Science Letters*, 465, 134–144. <https://doi.org/10.1016/j.epsl.2017.02.038>
- Faak, K., & Gillis, K. M. (2016). Slow cooling of the lowermost oceanic crust at the fast-spreading East Pacific Rise. *Geology*, 44(2), 115–118. <https://doi.org/10.1130/G37353.1>
- Faak, K., Chakraborty, S., & Coogan, L. A. (2013). Mg in plagioclase: Experimental calibration of a new geothermometer and diffusion coefficients. *Geochimica et Cosmochimica Acta*, 123, 195–217. <https://doi.org/10.1016/j.gca.2013.05.009>
- Faak, K., Coogan, L. A., & Chakraborty, S. (2014). A new Mg-in-plagioclase geospeedometer for the determination of cooling rates of mafic rocks. *Geochimica et Cosmochimica Acta*, 140, 691–707. <https://doi.org/10.1016/j.gca.2014.06.005>
- Faak, K., Coogan, L. A., & Chakraborty, S. (2015). Near conductive cooling rates in the upper-plutonic section of crust formed at the East Pacific Rise. *Earth and Planetary Science Letters*, 423, 36–47. <https://doi.org/10.1016/j.epsl.2015.04.025>
- Faak, K., Chakraborty, S., Coogan, L. A., & Dohmen, R. (2018). Comment on ‘Formation of fast-spreading lower oceanic crust as revealed by a new Mg–REE coupled geospeedometer’ by Sun and Lissenberg. *Earth and Planetary Science Letters*, 502, 284–286. <https://doi.org/10.1016/j.epsl.2018.08.036>
- Fabriès, J. (1979). Spinel-olivine geothermometry in peridotites from ultramafic complexes. *Contributions to Mineralogy and Petrology*, 69(4), 329–336. <https://doi.org/10.1007/BF00372258>
- Ganguly, J., & Tirone, M. (1999). Diffusion closure temperature and age of a mineral with arbitrary extent of diffusion: Theoretical formulation and applications. *Earth and Planetary Science Letters*, 170(1–2), 131–140. [https://doi.org/10.1016/S0012-821X\(99\)00089-8](https://doi.org/10.1016/S0012-821X(99)00089-8)
- Garrido, C. J., Kelemen, P. B., & Hirth, G. (2001). Variation of cooling rate with depth in lower crust formed at an oceanic spreading ridge: Plagioclase crystal size

- distributions in gabbros from the Oman ophiolite. *Geochemistry, Geophysics, Geosystems*, 2(10). <https://doi.org/10.1029/2000GC000136>
- Gillis, K. M., Snow, J. E., Klaus, A., Guerin, G., Abe, N., Akizawa, N., et al. (2014). Expedition 345 summary, 345. <https://doi.org/10.2204/iodp.proc.345.101.2014>
- Gillis, K. M., Snow, J. E., Klaus, A., Abe, N., Adrião, Á. B., Akizawa, N., et al. (2014). Primitive layered gabbros from fast-spreading lower oceanic crust. *Nature*, 505(7482), 204–207. <https://doi.org/10.1038/nature12778>
- Girardeau, J., & Francheteau, J. (1993). Plagioclase-wehrlites and peridotites on the East Pacific Rise (Hess Deep) and the Mid-Atlantic Ridge (DSDP Site 334): evidence for magma percolation in the oceanic upper mantle. *Earth and Planetary Science Letters*, 115(1–4), 137–149. [https://doi.org/10.1016/0012-821X\(93\)90218-X](https://doi.org/10.1016/0012-821X(93)90218-X)
- Godard, M., Joussetin, D., & Bodinier, J. L. (2000). Relationships between geochemistry and structure beneath a palaeo-spreading centre: A study of the mantle section in the Oman ophiolite. *Earth and Planetary Science Letters*, 180(1–2), 133–148. [https://doi.org/10.1016/S0012-821X\(00\)00149-7](https://doi.org/10.1016/S0012-821X(00)00149-7)
- Gregory, R. T., & Taylor, H. P. (1981). An oxygen isotope profile in a section of Cretaceous oceanic crust, Samail Ophiolite, Oman: Evidence for  $\delta^{18}\text{O}$  buffering of the oceans by deep (>5 km) seawater-hydrothermal circulation at mid-ocean ridges. *Journal of Geophysical Research: Solid Earth*, 86(B4), 2737–2755. <https://doi.org/10.1029/JB086iB04p02737>
- Grove, T. L., & Bryan, W. B. (1983). Fractionation of pyroxene-phyric MORB at low pressure: An experimental study. *Contributions to Mineralogy and Petrology*, 84(4), 293–309. <https://doi.org/10.1007/BF01160283>
- Hanghøj, K., Kelemen, P. B., Hassler, D., & Godard, M. (2010). Composition and genesis of depleted mantle peridotites from the Wadi Tayin massif, Oman ophiolite; Major and trace element geochemistry, and Os isotope and PGE systematics. *Journal of Petrology*, 51(1–2), 201–227. <https://doi.org/10.1093/petrology/egp077>

- Hekinian, R., Bideau, D., Francheteau, J., Cheminee, J. L., Armijo, R., Lonsdale, P., & Blum, N. (1993). Petrology of the East Pacific Rise Crust and Upper Mantle Exposed in Hess Deep ( Eastern Equatorial Pacific ) were zone 85øW a volcanically starved segment of the Cocos-Nazca ridge in the Hess Deep Upper levels and Kashintsev , Fe-oxyhydroxide, *98(92)*, 8069–8094.
- Henstock, T. J., Woods, A. W., & White, R. S. (1993). The accretion of oceanic crust by episodic sill intrusion. *Journal of Geophysical Research*, *98(B3)*, 4143–4161.  
<https://doi.org/10.1029/92JB02661>
- Hesse, K. T., Gose, J., Stalder, R., & Schmädicke, E. (2015). Water in orthopyroxene from abyssal spinel peridotites of the East Pacific Rise (ODP Leg 147: Hess Deep). *Lithos*, *232*, 23–34. <https://doi.org/10.1016/j.lithos.2015.06.011>
- Jochum, K. P., Nohl, U., Herwig, K., Lammel, E., Stoll, B., & Hofmann, A. W. (2005). GeoReM: A new geochemical database for reference materials and isotopic standards. *Geostandards and Geoanalytical Research*, *29(3)*, 333–338.  
<https://doi.org/10.1111/j.1751-908x.2005.tb00904.x>
- Johnson, K. T. M., Dick, H. J. B., & Shimizu, N. (1990). Melting in the Oceanic Upper Mantle' An Ion Microprobe Study of Diopsides in Abyssal Peridotites. *Journal of Geophysical Research*, *95(10)*, 2661–2678.  
<https://doi.org/10.1029/JB095iB03p02661>
- Jurewicz, A. J. G., & Watson, E. B. (1988). Cations in olivine, Part 2: Diffusion in olivine xenocrysts, with applications to petrology and mineral physics. *Contributions to Mineralogy and Petrology*, *99(2)*, 186–201. <https://doi.org/10.1007/BF00371460>
- Karson, J. A., Klein, E. M., Hurst, S. D., Lee, C. E., Rivizzigno, P. A., Curewitz, D., et al. (2002). Structure of uppermost fast-spread oceanic crust exposed at the Hess Deep Rift: Implications for subaxial processes at the East Pacific Rise. *Geochemistry, Geophysics, Geosystems*, *3(1)*, n/a-n/a.  
<https://doi.org/10.1029/2001GC000155>
- Kelemen, Peter B., Shimizu, N., & Salters, V. J. M. (1995). Extraction of mid-ocean-

- ridge basalt from the upwelling mantle by focused flow of melt in dunite channels. *Nature*. <https://doi.org/10.1038/375747a0>
- Kelemen, Peter B., Hirth, G., Shimizu, N., Spiegelman, M., & Dick, H. J. B. (1997a). A review of melt migration processes in the adiabatically upwelling mantle beneath oceanic spreading ridges. *Philosophical Transactions of the Royal Society of London. Series A: Mathematical, Physical and Engineering Sciences*, 355(1723), 283–318. <https://doi.org/10.1098/rsta.1997.0010>
- Kelemen, Peter B., Koga, K., & Shimizu, N. (1997b). Geochemistry of gabbro sills in the crust-mantle transition zone of the Oman ophiolite: implications for the origin of the oceanic lower crust. *Earth and Planetary Science Letters*, 146(3–4), 475–488. [https://doi.org/10.1016/S0012-821X\(96\)00235-X](https://doi.org/10.1016/S0012-821X(96)00235-X)
- Kelemen, Peter B., Matter, J. M., Teagle, D. A. H., Coggon, J. A., & Team, T. O. D. P. S. (2021a). Site CM1: layered gabbros, crustal ultramafic rocks, and mantle harzburgite. In P.B. Kelemen, J. M. Matter, D. A. H. Teagle, & J. A. Coggon (Eds.). College Station, TX: International Ocean Discovery Program. <https://doi.org/10.14379/OmanDP.proc.2020>
- Kelemen, Peter B., Matter, J. M., Teagle, D. A. H., Coggon, J. A., & Team, T. O. D. P. S. (2021b). Site CM2: Crust–Mantle Transition Zone and into upper mantle. In P.B. Kelemen, J. M. Matter, D. A. H. Teagle, & J. A. Coggon (Eds.). College Station, TX: International Ocean Discovery Program. <https://doi.org/10.14379/OmanDP.proc.2020>
- Klein, E. M., Smith, D. K., Williams, C. M., & Schouten, H. (2005). Counter-rotating microplates at the Galpagos triple junction. *Nature*, 433(1986), 855–858.
- Köhler, T. P., & Brey, G. P. (1990). Calcium exchange between olivine and clinopyroxene calibrated as a geothermobarometer for natural peridotites from 2 to 60 kb with applications. *Geochimica et Cosmochimica Acta*, 54(9), 2375–2388. [https://doi.org/10.1016/0016-7037\(90\)90226-B](https://doi.org/10.1016/0016-7037(90)90226-B)
- Korenaga, J., & Kelemen, P. B. (1997). Origin of gabbro sills in the Moho transition zone



- of the Oman ophiolite: Implications for magma transport in the oceanic lower crust. *Journal of Geophysical Research: Solid Earth*, 102(B12), 27729–27749.  
<https://doi.org/10.1029/97jb02604>
- Liang, Y. (2015). A simple model for closure temperature of a trace element in cooling bi-mineralic systems. *Geochimica et Cosmochimica Acta*, 165, 35–43.  
<https://doi.org/10.1016/j.gca.2015.05.028>
- Liang, Y., Sun, C., & Yao, L. (2013). A REE-in-two-pyroxene thermometer for mafic and ultramafic rocks. *Geochimica et Cosmochimica Acta*, 102, 246–260.  
<https://doi.org/10.1016/j.gca.2012.10.035>
- Lissenberg, C. J., & MacLeod, C. J. (2016). A reactive porous flow control on mid-ocean ridge magmatic evolution. *Journal of Petrology*, 57(11–12), 2195–2220.  
<https://doi.org/10.1093/petrology/egw074>
- Lissenberg, C. J., MacLeod, C. J., Howard, K. A., & Godard, M. (2013). Pervasive reactive melt migration through fast-spreading lower oceanic crust (Hess Deep, equatorial Pacific Ocean). *Earth and Planetary Science Letters*, 361, 436–447.  
<https://doi.org/10.1016/j.epsl.2012.11.012>
- Lonsdale, P. (1988). Structural Pattern of the Galapagos Microplate and Evolution of the galapagos Triple Junction. *Journal of Geophysical Research*, 93(B11), 13551–13574. <https://doi.org/10.1029/JB093iB11p13551>
- Lonsdale, P., Blum, N., & Puchelt, H. (1992). The RRR triple junction at the southern end of the Pacific-Cocos East Pacific Rise, 109, 73–85.
- Maclennan, J., Hulme, T., & Singh, S. C. (2004). Thermal models of oceanic crustal accretion: Linking geophysical, geological and petrological observations. *Geochemistry, Geophysics, Geosystems*, 5(2).  
<https://doi.org/10.1029/2003GC000605>
- Maclennan, John, Hulme, T., & Singh, S. C. (2005). Cooling of the lower oceanic crust. *Geology*, 33(5), 357–360. <https://doi.org/10.1130/G21207.1>
- MacLeod, C. J., Johan Lissenberg, C., & Bibby, L. E. (2013). “Moist MORB” axial

- magmatism in the Oman ophiolite: The evidence against a mid-ocean ridge origin. *Geology*, 41(4), 459–462. <https://doi.org/10.1130/G33904.1>
- Mevel, C., Gillis, K. M., Allan, J. F., & Meyer, P. S. (Eds.). (1996). Proceedings of the Ocean Drilling Program, 147 Scientific Results, 147. <https://doi.org/10.2973/odp.proc.sr.147.1996>
- Mock, D., Neave, D. A., Müller, S., Garbe-Schönberg, D., Namur, O., Ildefonse, B., & Koepke, J. (2021). Formation of Igneous Layering in the Lower Oceanic Crust From the Samail Ophiolite, Sultanate of Oman. *Journal of Geophysical Research: Solid Earth*, 126(1). <https://doi.org/10.1029/2020JB019573>
- Natland, J. H., & Dick, H. J. B. (2009). Paired melt lenses at the East Pacific Rise and the pattern of melt flow through the gabbroic layer at a fast-spreading ridge. *Lithos*, 112(1–2), 73–86. <https://doi.org/10.1016/j.lithos.2009.06.017>
- Navon, O., & Stolper, E. (1987). Geochemical Consequences of Melt Percolation: The Upper Mantle as a Chromatographic Column. *The Journal of Geology*, 95(3), 285–307. <https://doi.org/10.1086/629131>
- Nicolas, A. (1989). *Structures of Ophiolites and Dynamics of Oceanic Lithosphere* (Vol. 4). Dordrecht: Springer Netherlands. <https://doi.org/10.1007/978-94-009-2374-4>
- Nicolas, A., & Boudier, F. (2015). Structural contribution from the Oman ophiolite to processes of crustal accretion at the East Pacific Rise. *Terra Nova*, 27(2), 77–96. <https://doi.org/10.1111/ter.12137>
- Nicolas, A., Reuber, I., & Benn, K. (1988). A new magma chamber model based on structural studies in the Oman ophiolite. *Tectonophysics*, 151(1–4), 87–105. [https://doi.org/10.1016/0040-1951\(88\)90242-9](https://doi.org/10.1016/0040-1951(88)90242-9)
- Nielsen, R. L., Sours-Page, R. E., & Harpp, K. S. (2000). Role of a Cl-bearing flux in the origin of depleted ocean floor magmas. *Geochemistry, Geophysics, Geosystems*, 1(5). <https://doi.org/10.1029/1999gc000017>
- Pallister, J. S., & Hopson, C. A. (1981). Samail ophiolite plutonic suite: field relations, phase variation, cryptic variation and layering, and a model of a spreading ridge

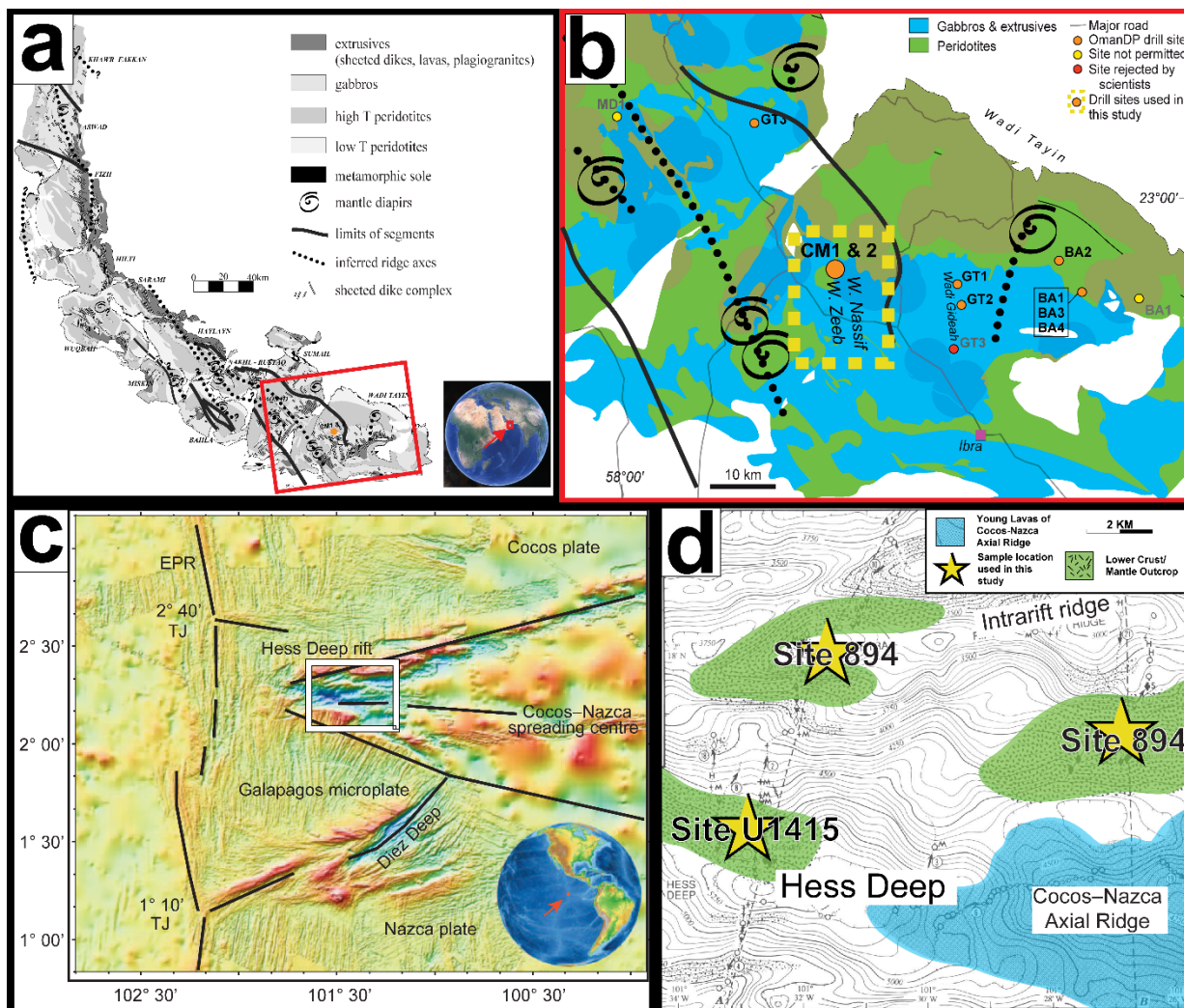
- magma chamber. *Journal of Geophysical Research*, 86(B4), 2593–2644.  
<https://doi.org/10.1029/JB086iB04p02593>
- Pallister, J. S., & Knight, R. J. (1981). Rare-earth element geochemistry of the Samail Ophiolite near Ibra, Oman. *Journal of Geophysical Research: Solid Earth*, 86(B4), 2673–2697. <https://doi.org/10.1029/JB086iB04p02673>
- Pearce, J. A., Alabaster, T., Shelton, A. W., & Searle, M. P. (1981). The Oman ophiolite as a Cretaceous arc-basin complex: evidence and implications. *Philosophical Transactions of the Royal Society of London. Series A, Mathematical and Physical Sciences*, 300(1454), 299–317. <https://doi.org/10.1098/rsta.1981.0066>
- Phipps Morgan, J., & Chen, Y. J. (1993). The genesis of oceanic crust: Magma injection, hydrothermal circulation, and crustal flow. *Journal of Geophysical Research: Solid Earth*, 98(B4), 6283–6297. <https://doi.org/10.1029/92JB02650>
- Pirard, C., Hermann, J., & O'Neill, H. S. C. (2013). Petrology and geochemistry of the crust-mantle boundary in a Nascent Arc, Massif du Sud Ophiolite, New Caledonia, SW Pacific. *Journal of Petrology*, 54(9), 1759–1792.  
<https://doi.org/10.1093/petrology/egt030>
- Purdy, G. M., Kong, L. S. L., Christeson, G. L., & Solomon, S. C. (1992). Relationship between spreading rate and the seismic structure of mid-ocean ridges. *Nature*, 355(6363), 815–817. <https://doi.org/10.1038/355815a0>
- Putirka, K. (1997). Magma transport at Hawaii: Inferences based on igneous thermobarometry. *Geology*, 25(1), 69–72. [https://doi.org/10.1130/0091-7613\(1997\)025<0069:MTAHIB>2.3.CO;2](https://doi.org/10.1130/0091-7613(1997)025<0069:MTAHIB>2.3.CO;2)
- Python, M., & Ceuleneer, G. (2003). Nature and distribution of dykes and related melt migration structures in the mantle section of the Oman ophiolite. *Geochemistry, Geophysics, Geosystems*, 4(7), 1–34. <https://doi.org/10.1029/2002GC000354>
- Quick, J. E., & Denlinger, R. P. (1993). Ductile deformation and the origin of layered gabbro in ophiolites. *Journal of Geophysical Research: Solid Earth*, 98(B8), 14015–14027. <https://doi.org/10.1029/93jb00698>

- Rioux, M., Garber, J., Bauer, A., Bowring, S., Searle, M., Kelemen, P. B., & Hacker, B. (2016). Synchronous formation of the metamorphic sole and igneous crust of the Semail ophiolite: New constraints on the tectonic evolution during ophiolite formation from high-precision U–Pb zircon geochronology. *Earth and Planetary Science Letters*, *451*, 185–195. <https://doi.org/10.1016/j.epsl.2016.06.051>
- Sinton, J. M., & Detrick, R. S. (1992). Mid-ocean ridge magma chambers. *Journal of Geophysical Research*, *97*(B1), 197–216. <https://doi.org/10.1029/91JB02508>
- Sleep, N. H. (1975). Formation of oceanic crust: Some thermal constraints. *Journal of Geophysical Research*, *80*(29), 4037–4042. <https://doi.org/10.1029/JB080i029p04037>
- Smewing, J. D. (1981). Mixing characteristics and compositional differences in mantle-derived melts beneath spreading axes: Evidence from cyclically layered rocks in the ophiolite of North Oman. *Journal of Geophysical Research: Solid Earth*, *86*(B4), 2645–2659. <https://doi.org/10.1029/jb086ib04p02645>
- Sparks, J. (2011). LasyBoy. Boston University, U.S.A.
- Sun, C., & Liang, Y. (2017). A REE-in-plagioclase–clinopyroxene thermometer for crustal rocks. *Contributions to Mineralogy and Petrology*, *172*(4), 1–20. <https://doi.org/10.1007/s00410-016-1326-9>
- Sun, C., & Lissenberg, C. J. (2018a). Formation of fast-spreading lower oceanic crust as revealed by a new Mg–REE coupled geospeedometer. *Earth and Planetary Science Letters*, *487*, 165–178. <https://doi.org/10.1016/j.epsl.2018.01.032>
- Sun, C., & Lissenberg, C. J. (2018b). Caveats and challenges in geospeedometry: A reply to Faak et al.'s critique of the Mg–REE coupled geospeedometry. *Earth and Planetary Science Letters*, *502*, 287–290. <https://doi.org/10.1016/j.epsl.2018.08.044>
- Takazawa, E., Frey, F., Shimizu, N., & Obata, M. (1996). Evolution of the Horoman Peridotite (Hokkaido, Japan): Implications from pyroxene compositions. *Chemical Geology*, *134*(1–3), 3–26. [https://doi.org/10.1016/S0009-2541\(96\)00083-6](https://doi.org/10.1016/S0009-2541(96)00083-6)

- Turcotte, D. L., & Schubert, G. (2002). *Geodynamics - 2nd edition*.  
<https://doi.org/10.2277/0521661862>
- VanTongeren, J. A., Kelemen, P. B., & Hanghøj, K. (2008). Cooling rates in the lower crust of the Oman ophiolite: Ca in olivine, revisited. *Earth and Planetary Science Letters*, 267(1–2), 69–82. <https://doi.org/10.1016/j.epsl.2007.11.034>
- VanTongeren, J. A., Hirth, G., & Kelemen, P. B. (2015). Constraints on the accretion of the gabbroic lower oceanic crust from plagioclase lattice preferred orientation in the Samail ophiolite. *Earth and Planetary Science Letters*, 427, 249–261.  
<https://doi.org/10.1016/j.epsl.2015.07.001>
- Villiger, S., Ulmer, P., Müntener, O., & Thompson, A. B. (2004). The liquid line of descent of anhydrous, mantle-derived, tholeiitic liquids by fractional and equilibrium crystallization - An experimental study at 1.0 GPa. *Journal of Petrology*, 45(12), 2369–2388. <https://doi.org/10.1093/petrology/egh042>
- Warren, J. M. (2016). Global variations in abyssal peridotite compositions. *Lithos*, 248–251, 193–219. <https://doi.org/10.1016/j.lithos.2015.12.023>
- Wells, P. R. A. (1977). Pyroxene thermometry in simple and complex systems. *Contributions to Mineralogy and Petrology*, 62(2), 129–139.  
<https://doi.org/10.1007/BF00372872>
- Witt-Eickschen, G., & Seck, H. A. (1991). Solubility of Ca and Al in orthopyroxene from spinel peridotite: an improved version of an empirical geothermometer. *Contributions to Mineralogy and Petrology*, 106(4), 431–439.  
<https://doi.org/10.1007/BF00321986>
- Yao, L., & Liang, Y. (2015). Closure temperature in cooling bi-mineralic systems: I. Definition and with application to REE-in-two-pyroxene thermometer. *Geochimica et Cosmochimica Acta*, 162, 137–150. <https://doi.org/10.1016/j.gca.2015.03.041>

# Appendix

## Appendix 1. Supplemental Figures



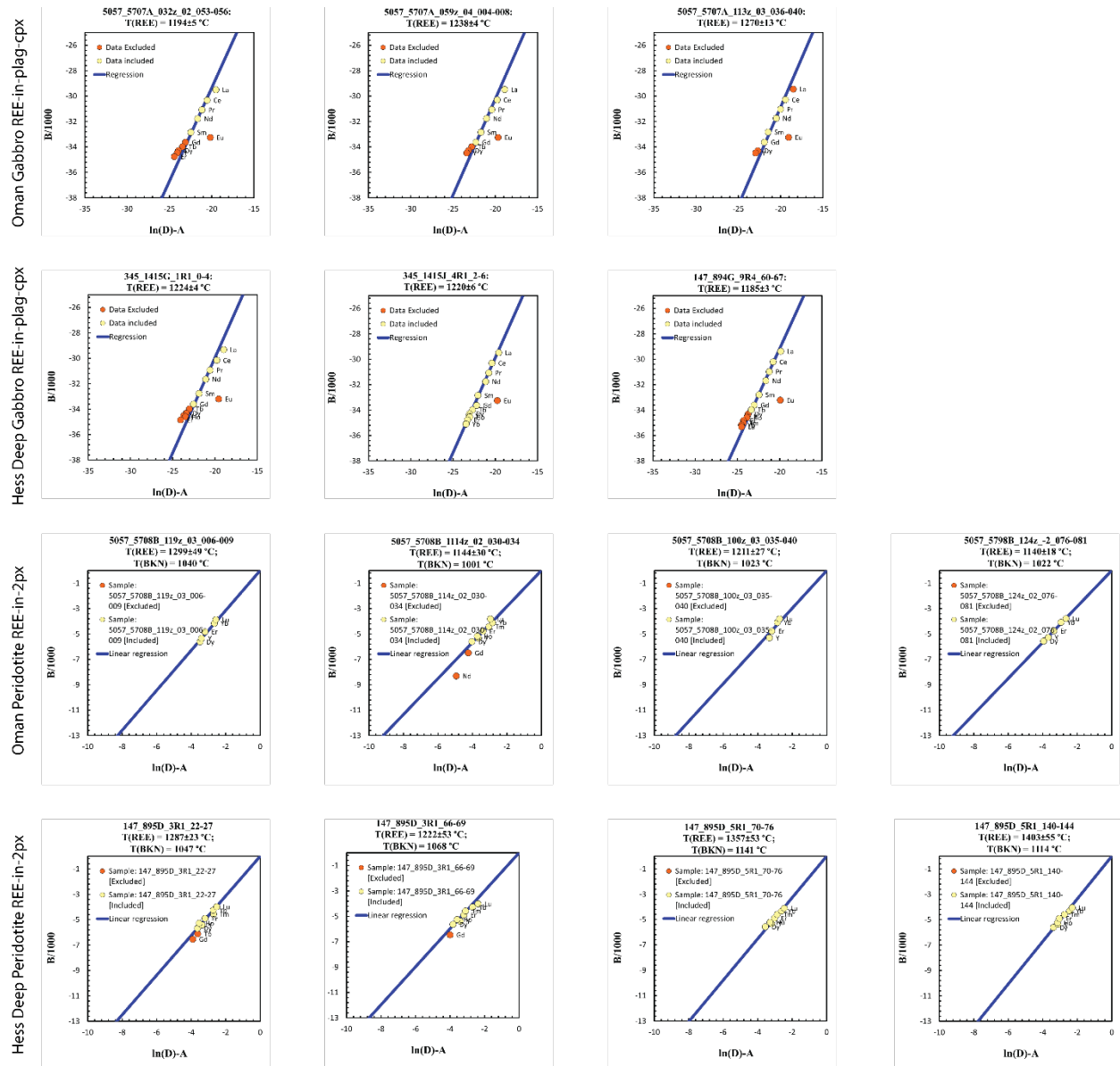


Figure 1.12. Inversion diagrams from application of REE-in-two-pyroxene (Liang et al., 2013) and REE-in-plag-cpx (Sun & Liang, 2017) thermometers to peridotite and gabbro samples from Hess Deep and the Oman Drilling Project. All reported trace element data are shown, with data excluded from the temperature inversions indicated using orange symbols. Data used in the temperature determinations are indicated in yellow. Inversion diagrams were produced using Excel spreadsheets available publicly on the web at <http://earth-sun.weebly.com>.

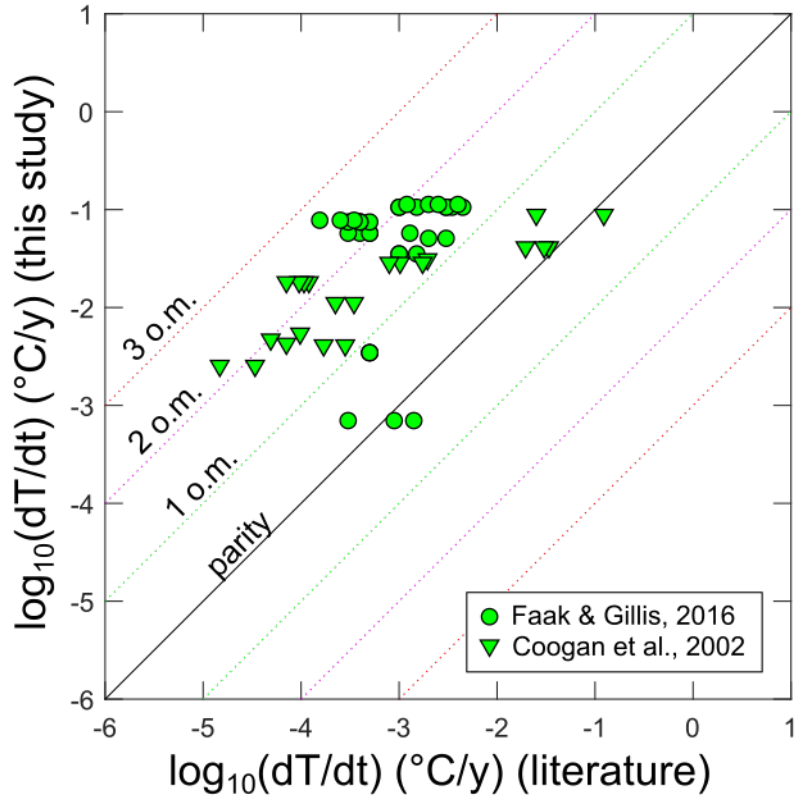


Figure 1.13. A comparison of Ca-in-olivine cooling rates determined for Hess Deep gabbros (Faak & Gillis, 2016, circles) and gabbros from the Wadi Abyad section of the Samail ophiolite (Coogan et al., 2002, triangles) to rates recalculated using the methods we employed in this study. For consistency, literature rates for the Wadi Abyad data were gathered from Coogan et al., 2007, as they were calculated using the Ca-in-olivine diffusivity of Coogan et al., 2005, as employed in the main text and in other studies. The black line is the 1:1 line, green, magenta and red dotted lines show order of magnitude deviations of the literature rates from recalculated rates. Recalculated rates are mostly somewhat higher; average deviations of the recalculated rates from the literature rates are 1.4 and 1.6 orders of magnitude for Coogan et al. (2002; 2007) and Faak and Gillis (2016) respectively. In the case of the Faak & Gillis (2016) dataset, samples with slower rates agree better with the recalculated rates. In the case of the Coogan et al. (2002; 2007) data, samples with faster rates better agree with the recalculated rates.



### **Appendix 1 References**

- MacLeod, C. J., Celerier, B., Fruh-Green, G. L., & Manning, C. E. (1996). Tectonics of Hess Deep: A Synthesis of Drilling Results from Leg 147. *Proceedings of the Ocean Drilling Program, 147 Scientific Results, 147*(1990).  
<https://doi.org/10.2973/odp.proc.sr.147.032.1996>
- Nicolas, A., Bouldier, F., Ildefonse, B., & Ball, E. (2000). Accretion of Oman and United Arab Emirates ophiolite - Discussion of a new structural map. *Marine Geophysical Research, 21*(3–4), 147–180. <https://doi.org/10.1023/A:1026769727917>

## **Chapter 2: Microstructural Investigation of Ilmenite-Olivine Aggregates Deformed in Shear**

## Abstract

To examine the development of fabrics and rheological properties of ilmenite<sub>40</sub> ((Fe<sub>0.4</sub>Mg<sub>0.6</sub>)TiO<sub>3</sub>)-olivine aggregate rocks, general shear molten salt cell experiments were conducted on varying phase proportions in a Griggs-style apparatus at confining pressures of 1 GPa and 1100°C, and a nominal axial compression rate of 10<sup>-6</sup> s<sup>-1</sup>. The mechanical data from deformation carried out for this study show that higher percentages of ilmenite<sub>40</sub> in aggregates lead to increased weakening of the aggregate. Photomicrograph and electron back scatter diffraction analysis data from 5 samples with 4 different phase proportions show the weaker phase, ilmenite, preferentially accommodates the strain in the system even at volume fractions as low as 10%. In all samples, ilmenite shows development of c-axis alignment perpendicular to the shear plane, while olivine shows B-type fabric development, most prominent in high olivine, high total accumulated strain samples. The data from this study provide a starting point that could aid in the model refinement of lunar mantle overturn caused by density driven Rayleigh-Taylor instabilities formed between an ilmenite bearing cumulate layer and an underlying, earlier crystallized, mafic cumulate pile.

## 1. Introduction

Aggregate flow laws are of interest to a wide range of geologic problems, ranging from applications in modern plate tectonics to aiding models for the history of the lunar interior. This study examines the rheologic behavior of two minerals, ilmenite, and olivine, in aggregate deformation experiments, to better constrain the process of mantle overturn due to density instability during the crystallization of the lunar mantle (e.g. Charlier et al., 2018; Dygert et al., 2016; Elardo et al., 2011; Elkins-Tanton et al., 2011; Hess & Parmentier, 1995; Maurice et al., 2020; Michaut & Neufeld, 2022; Shearer et al., 2006; Snyder et al., 1992). Through increased constraint of system rheology between the late-stage ilmenite bearing cumulate (IBC) layer and the underlying mafic cumulate pile that formed from the lunar magma ocean, future modeling efforts can better predict the geometry and scale of overturn, caused by the sinking of the IBC. In this study, we use molten salt cell general shear experiments in a Griggs-style deformation apparatus

to test the properties of different percent mixtures of ilmenite and olivine and examine the effect of each mineral phase on the overall strength of the aggregate.

Flow laws for individual minerals have been established through field and laboratory observations and refined through experimental methods in efforts to explain the deformation behaviors of rocks on Earth and the Moon (e.g. Dygert et al., 2016; Goetze & Poirier, 1978; Hansen et al., 2011; Hirth & Kohlstedt, 2003; Kohlstedt & Goetze, 1974; Stipp et al., 2002; J. L. Till & Rybacki, 2020; J. Till & Moskowitz, 2013; Tokle et al., 2019, 2021; Y. H. Zhao et al., 2009). While some minerals, such as olivine and quartz are well studied as proxies for the upper continental crust and the mantle lithosphere, minerals that are less abundant in terrestrial geologic systems, such as ilmenite, have only recently been characterized in flow laws. For this study, we investigated the rheologic behavior of ilmenite and olivine via aggregate deformation experiments with differing proportions of ilmenite<sub>40</sub> ((Fe<sub>0.4</sub>Mg<sub>0.6</sub>)TiO<sub>3</sub>) (ilm<sub>40</sub>) and San Carlos olivine (SCO), which are in chemical equilibrium at mantle-relevant experimental conditions, while comparing results to monomineralic flow laws established for two lunar mantle-relevant minerals, ilmenite and olivine (Hirth & Kohlstedt, 2003; Tokle et al., 2021),.

The strength and viscosity of polymineralic rocks depends on the partitioning of deformation into the different phases and can be relatively independent of phase proportions depending on deformation mechanisms and individual grain behaviors. Theoretical aggregate flow laws have been developed through numerical modeling (e.g., Bevilard et al., 2019; Huet et al., 2014; T. E. Tullis et al., 1991) and from examination of experimental and natural samples (e.g. Dimanov & Dresen, 2005; Faul et al., 2016; Gonçalves et al., 2015; Handy, 1990, 1994; Herwegh et al., 2011; Jordan, 1987; Platt, 2015; J. Tullis & Wenk, 1994; T. E. Tullis et al., 1991), but aggregate rheologies are unique to the minerals in the system and the conditions of deformation. Findings from Jordan (1987) and Gonçalves et al. (2015) suggest that deformed aggregate strength is highly dependent on percent weak phase from experimental findings on limestone-halite, and quartz-iron oxides, respectively.

In this study, we investigate the effect of ilm40 on the strength of SCO in different volume fractions of ilm40:SCO to observe the aggregate behavior of these lunar mantle-relevant materials. We conducted general shear experiments on samples of natural SCO and synthesized ilm40 to examine the effect of the stronger, and more viscous olivine, when mixed with weaker, less viscous ilm40, on the overall rock behavior during deformation and to compare the resulting microstructures at different phase proportions and total strain.

## 2. Experimental Design and Methods

General shear experiments were conducted in a Griggs-type apparatus using molten salt assemblies (Figure 2.1a) at confining pressures of 1 GPa and temperatures of 1100°C. Molten salt cells are designed for use at high temperatures and pressures, and have low friction, allowing for accurate measurements on Griggs-type apparatus (Holyoke-III, 2005).

### 2.1 Starting Materials

Preliminary investigation of aggregate ilmenite:olivine rheology in shear used end-member ilmenite ( $\text{FeTiO}_3$ ) and San Carlos olivine ( $(\text{Mg}_{0.9}\text{Fe}_{0.1})_2\text{SiO}_4$ ), which are not in equilibrium at the experimental conditions (Andersen & Lindsley, 1979; Thacker et al., 2009). For this study, ilm40 ( $(\text{Mg}_{0.6}\text{Fe}_{0.4})\text{TiO}_3$ ) synthesized by L. Tokle for Tokle et al. (2021), was used. This composition of 40% ilmenite and 60% giekielite ( $\text{MgTiO}_3$ ) is in equilibrium with SCO at the experimental conditions of 1 GPa confining pressure and 1100°C, as experimentally determined in previous studies (Andersen & Lindsley, 1979; Thacker et al., 2009; Tokle et al., 2021).

Starting powders of SCO and ilm40 were ground and sieved to a minimum grain size of 20-30  $\mu\text{m}$ . As per the steps outlined in Appendix B of Holyoke, (2005), experimental powders and shear pistons were cold pressed into a thick Ni jacket and conditioned in a horizontal gas mixing furnace at 1000°C at an oxygen fugacity approximating the Ni/NiO buffer for 9 hours. The conditioned samples were then inserted into thinner Pt and Ni outer jackets with Ni and Pt disks covering the top and bottom of the jacketed sample (Figure 2.1a). The Pt sleeve was mechanically folded

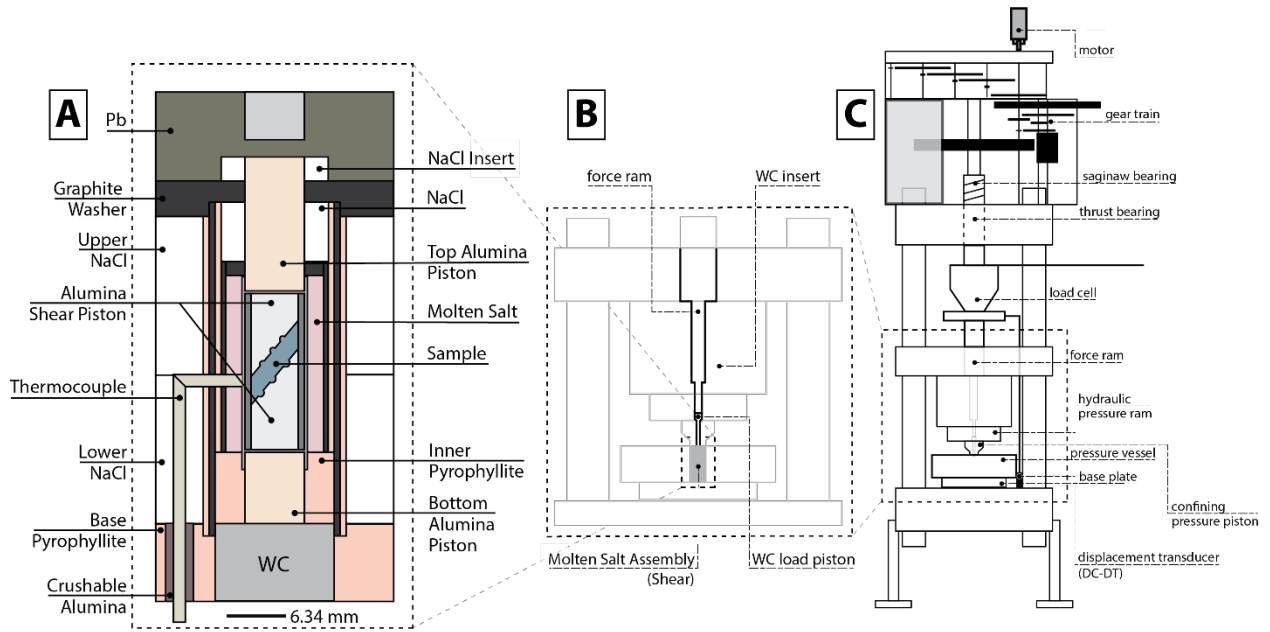


Figure 2.11. Diagram of components for molten salt cell and Griggs apparatus used in this study. Panel A shows the assembly for the sample in shear. Panel B shows the interior schematic for the force ram portion of the Griggs apparatus and panel C shows the entire Griggs apparatus. Figure modified from Holyoke and Kronenberg, 2010 for Rig 2 at the Brown University Rock Deformation lab.

over the disks to seal the jacketed sample. The jacketed samples were then annealed overnight at run conditions prior to deformation. A hydrostatic experiment, LMO-007, demonstrates vertical shortening of the powders by approximately 3% prior to and during annealing.

## **2.2 Experimental Conditions**

Experiments were conducted at 1100°C and at a confining pressure of 1.0 +/- 0.1 GPa at a nominal axial compression rate of 10<sup>-6</sup> s<sup>-1</sup>. Individual sample data related to each run are listed in Table 2.1. To preserve the microstructures, at the end of the experiment the temperature was lowered at a rate of 3°C/s to 300°C whenever possible, though due to thermocouple failures, samples LMO-001, LMO-003, and LMO-004 were quenched from 1100°C for reasons specified in Table 2.2. During the temperature decrease, the confining pressure decreases slightly, and once the sample temperature decreases to 300°C, the confining pressure is decreased manually over 1 hour to prevent decompression cracking.

Applied force and deformation piston displacement during experimental runs are measured through an external load cell and displacement transducer (resolution = 1 μm) (Figure 2.1c). Experimental run data are recorded at a sampling rate of 2 Hz digitally. Data were processed using a version of the RIG program for MATLAB (Peč, 2010), modified to work with data produced by Rig 2 at Brown University.

Notes on experimental runs, including experimental conditions, thermocouple failures and changes to motor speeds pre-deformation are noted in Table 2.2, with the run number for the Brown University cataloging system and the sample number assigned for this study.

## **3. Analytical Methods**

Post-deformation, samples were prepared for microanalysis by carefully extracting the jacketed sample from the molten salt assembly, and marking the orientation, and indicating the position of the thermocouple, when possible. Samples were then cut in half perpendicular to the strike of the shear pistons, along the dip of the deformed sample. One-half of the sample was then mounted in 1-inch clear epoxy pucks for photomicrograph and electron beam microanalysis.

**Table 2.3 Sample information by experiment in order of first run to last run.**

Run Number	Sample Name	Volume percent ilm40	Volume percent SCO	Temperature	Force ram displacement rate (mm*s <sup>-1</sup> )	Post-run thickness <sup>^</sup> (μm)	Shear strain rate*	Axial equivalent strain rate*
W2384	LMO-001	100	0	1100°C	1.85E-05	1.0851	3.86E-06	7.72E-06
W2387	LMO-002	10	90	1100°C	1.80E-05	1.0200	4.26E-06	8.52E-06
W2389	LMO-003	10	90	1100°C	9.19E-06	0.9100	1.77E-06	3.53E-06
W2393	LMO-004	50	50	1100°C	1.86E-05	0.9369	3.50E-06	7.00E-06
W2395	LMO-005	25	75	1100°C	1.86E-05	1.0869	6.42E-07	1.28E-06
W2546	LMO-006	5	95	1100°C	N/A	..	..	..
W2544	LMO-007	10	90	1100°C	Hydrostatic	1.0912	..	..
W2549	LMO-008	5	95	1100°C	N/A	..	..	..
W2562	LMO-009	5	95	1100°C	9.26E-06	..	9.77E-06	1.95E-05
W2559	LMO-010	25	75	1100°C	9.37E-06	1.2000	8.23E-07	1.65E-06
W2560	LMO-011	25	75	1100°C	9.35E-06	1.4498	2.86E-06	5.73E-06

\* Shear strain rate calculated for end of experiment.

<sup>^</sup>Thickness is measured from piston to piston (perpendicular to piston surface) in 5 spots on sample, then averaged. Height is the vertical height of the sample in the direction of axial compression, and is calculated from thickness using height = thickness \* sin(45°). Starting sample thickness was calculated from the mass of the SCO and ilm40, converted to volume. Percent compaction prior to deformation was estimated from a hydrostatic experiment and thinning was assumed constant throughout.



**Table 2.4. Notes on variations in experimental run conditions.**

<b>Run Number</b>	<b>Sample name</b>	<b>Notes</b>
W2384	LMO-001	Failsafe tripped, motor ran in ~ 1.5 hours post trip
W2387	LMO-002	Turned failsafe off and watched output until quench. Shows excessive T swings, likely thermocouple issue.
W2389	LMO-003	Failsafe tripped, motor turned off immediately
W2393	LMO-004	Failsafe tripped in middle of night, motor may have ran in 4+ hours
W2395	LMO-005	Quenched Sample
W2546	LMO-006	No hit, thermocouple failure and ran on output until it was unstable
W2544	LMO-007	Thermocouple failure before motor was turned on. Sat at temperature for ~4 hours
W2549	LMO-008	Failed thermocouple, motor ran in while cold.
W2558/W2562	LMO-009	Initially ran as W2558, thermocouple failure at 700°C. Removed and rerun as W2562. Thermocouple failure/extreme T flux for final 6 hours of experiment, cannot confirm thickness/lack of salt leak
W2559	LMO-010	Ran in fast ( $1 \times 10^{-5}$ ), ran stress loops at end of experiment which induced a pressure leak
W2560	LMO-011	Ran in fast ( $1 \times 10^{-5}$ )

Samples were analyzed under reflected light to check for potential salt leaks and to measure the post-deformation height and thickness of the sample. Backscatter electron (BSE) images were taken of samples to perform visual assessment of the phase ratios, distribution of grains, and do initial observation of microstructures.

After preliminary analysis at the University of Tennessee – Knoxville, all samples ran in 2019, LMO-001, LMO-002, LMO-003, LMO-004 & LMO-005, were taken to Scripps Institution of Oceanography, to run electron backscatter diffraction (EBSD) analysis for microstructural data.

### ***3.1 Electron Backscatter Diffraction***

EBSD analyses were completed using an Oxford Instruments Symmetry EBSD detector on a FEI Apreo LoVac Field Emission Gun Scanning Electron Microscope (SEM) at the University of California – San Diego/Scripps Institution of Oceanography. All samples were analyzed at a 1  $\mu\text{m}$  step size, across the entire polished surface of the sample at a working distance between 26 to 28 mm, and voltage of 20 kV. Sample LMO-001 was indexed for only ilmenite because it was prepared as a 100% ilmenite experiment. Samples LMO-002, LMO-003, LMO-004 and LMO-005 were indexed for ilmenite and forsterite.

Data processing was completed using the open source MTEX software (version 5.7.0) (Bachmann et al., 2011). The program was used to correct for rotation of the epoxy mount so that all samples plotted with the shear pistons in the same orientation, then used to generate EBSD maps, pole figures, and statistical data such as aspect ratio histograms and misorientation index (M-index) characterization. The M-index describes fabric strength in a deformed sample (Skemer et al., 2005). Grain boundaries for indexed minerals were defined with an angle of  $10^\circ$ .

## **4. Mechanical Data and Analytical Results**

### ***4.1 Mechanical Data***

Mechanical data processed using code based on RIG (Peč, 2010) are shown in Figure 2.2. Shear strain is plotted against shear stress in (a) and phase ratios are denoted at the termination of each curve in the ilm40:SCO format. Conversion to axial equivalent strain versus axial equivalent stress is shown in (b) for experiments LMO-

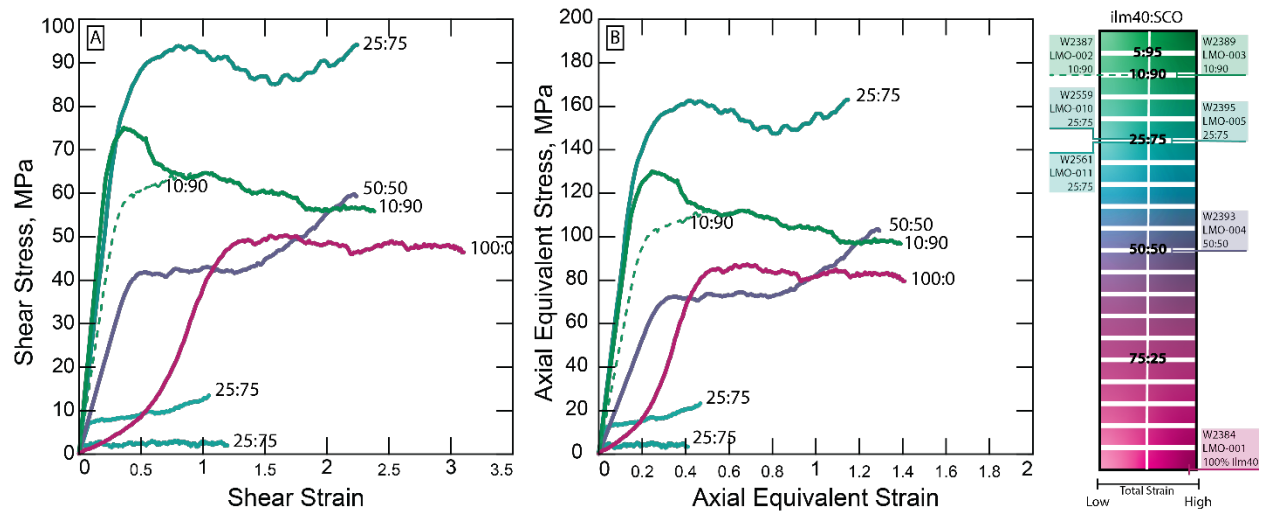


Figure 2.12. Mechanical data plots for deformed experiments from this study. Samples are color coded based on the spectrum at right, with pink representing ilm40 and green representing SCO. For samples with the same proportions of ilm40:SCO, sample hue is lighter for low total strain and darker for high accumulated strain. Mechanical data are cropped to begin at the hit point as calculated in MATLAB and end at initial pressure decrease at time of thermocouple failure and/or experiment completion.

001, LMO-002, LMO-003, LMO-004, LMO-005, LMO-010, LMO-011. Corrections to raw mechanical data were made using general shear assumptions in MATLAB which assume a constant shortening rate in the vertical direction and offset of the pistons during deformation (Paterson & Olgaard, 2000).

#### *4.1.1 Dormant Rig complications in runs from July 2021 and January 2022*

Samples LMO-006, LMO-007, LMO-008 and the first run of LMO-009, experienced power failures during the pressurization and heating process of the experiment and were therefore undeformed. Troubleshooting of the sample assembly revealed minor microstructural differences in mullite between manufacturers that caused shearing in the small arm of the thermocouple, near the interface between the outer salt and graphite can. This process of troubleshooting highlighted the sensitivity of the experimental design to all assembly components. Sample LMO-007 was used to determine compression of sample materials pre-deformation, as it was able to dwell at the same pressure and temperature conditions as deformed samples for approximately 4 hours prior to failure. This hydrostatic experiment provided the data used to calculate percent compaction during pressurization and temperature increases.

#### *4.1.2 Correcting for fast run-ins*

Experimental runs when the motor speed at time of sample hit was faster than the deformation conditions (W2559 (LMO-010), W2560 (LMO-011), W2562 (LMO-009)) were corrected in MATLAB by shifting the accelerated compression portion by the average of the load change at acceleration and at deceleration, over the entire time interval of stable compression at the higher motor speed. The change in load seen at different motor speeds can be attributed to friction in the rig that varies with axial compression rates. The portions of the record where the run in was stabilizing were then removed and replaced by a linear regression of the values at the starting and ending times of the segment removed. This approach enabled calculation of a corrected hit point.

## **4.2 Microstructures**

Crystallographic preferred orientations (CPOs) for ilmenite (0001) are shown in the left-hand column of Figure 2.3 for LMO-001, LMO-002, LMO-003, LMO-004 and

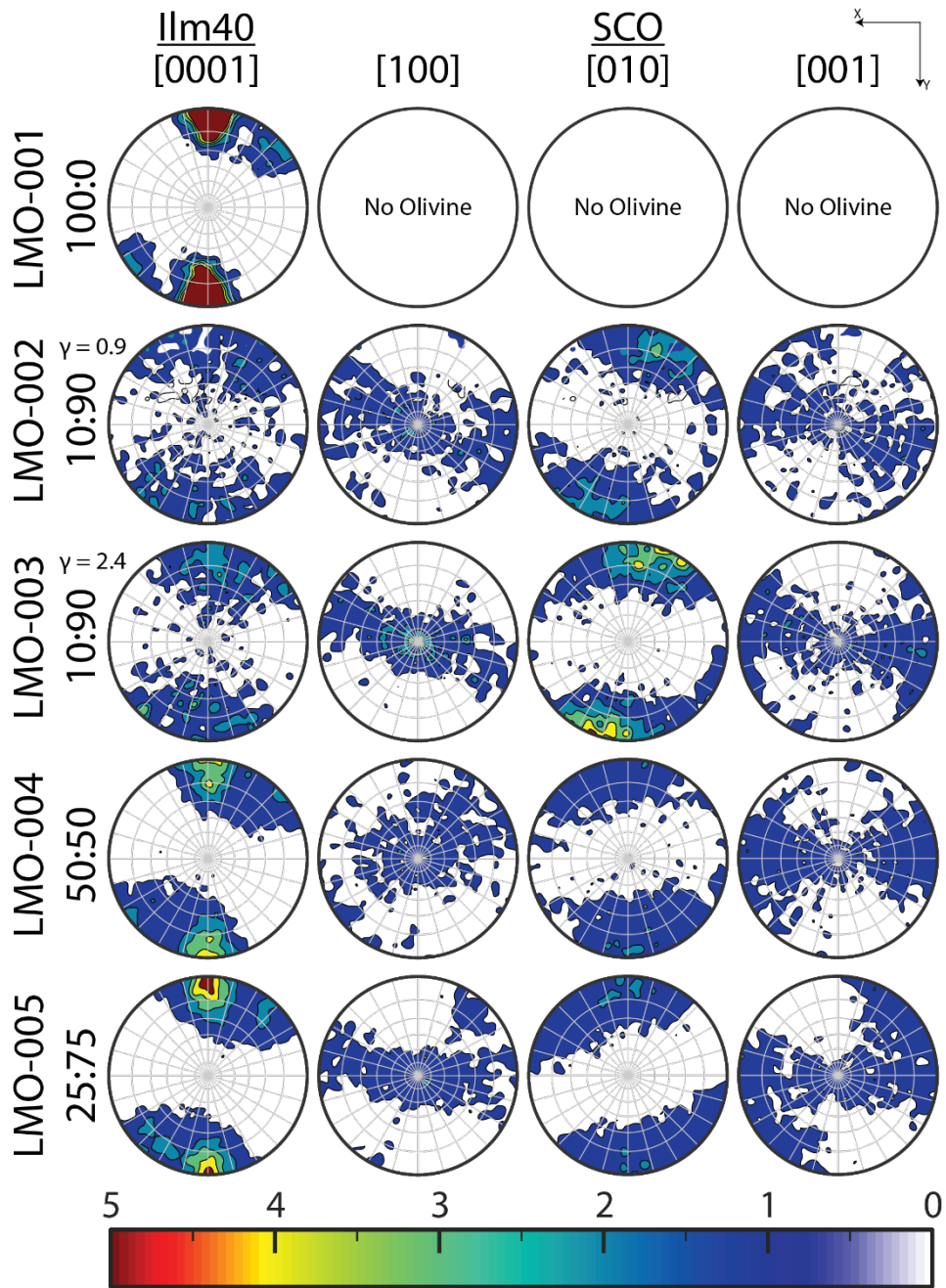


Figure 2.13. Ilmenite (0001) CPOs and Forsterite (001), (010) and (100) CPOs for samples LMO-001, -002, -003, -004, & -005, with ilm40:SCO ratios and total accumulated shear strain and axial equivalent strain. All sample MUD scales are set to the color scale at the bottom of the figure.

LMO-005 (top to bottom). In the 3 right-hand columns of Figure 2.3, CPOs for Forsterite (olivine) (100), (010), and (001) are shown for LMO-002, LMO-003, LMO-004, and LMO-005. M-index values for ilmenite and olivine are provided in Table 2.3 based on the orientation distribution function generated by MTEX.

Grain area and aspect ratio maps for each indexed phase are shown in the supplement, along with representative BSE images (Supplementary Figure 2.6) for LMO-001, LMO-002, LMO-003, LMO-004 and LMO-005. The BSE images show ilmenite as the bright phase and olivine as the gray phase. Pistons are visible in the corners of all images for reference to the plane of deformation and appear as dark gray-to-black in color. The aspect ratio data attained from building the aspect ratio and grain area maps are plotted as histograms in Figure 2.4 for all samples analyzed by EBSD.

## 5. Discussion

### 5.1 Flow Law

The rheological behavior of the individual phases in this study are both best described by a power law dependence of strain rate ( $\dot{\epsilon}$ ) on differential stress ( $\sigma$ ). The power law form

$$\dot{\epsilon} = A * \sigma^n \exp\left(-\frac{E+PV}{RT}\right) \quad (1)$$

is applied to both materials, with the addition of a variable for water content in the olivine flow law (Hirth & Kohlstedt, 2003; Tokle et al., 2021).

#### 5.1.1 Olivine Flow Laws

Based on the experimental conditions and materials employed, we apply the olivine flow law of Hirth & Kohlstedt (2003) for wet dislocation creep with a constant water content ( $C_{OH}$ ):

$$\dot{\epsilon} = A * C_{OH}^r * \sigma^n \exp\left(-\frac{E+PV}{RT}\right) \quad (2)$$

where constant (A) = 90 MPa<sup>-n</sup>s<sup>-1</sup>, the water fugacity exponent (r) = 1.2, the stress exponent (n) = 3.5, the strain rate ( $\dot{\epsilon}$ ) = 1.3x10<sup>-5</sup>/s, activation energy (E) = 480 kJ/mol, pressure for all experiments (P) = 1x10<sup>9</sup> MPa, activation volume (V) = 11x10<sup>-6</sup> m<sup>3</sup>/mol, the gas constant (R) = 8.3145 J·mol<sup>-1</sup>·K<sup>-1</sup>, and the temperature for all experiments (T) = 1373 Kelvin. Samples were conditioned in their sealed assembly at atmospheric

**Table 2.5. Sample results from mechanical data and EBSD analysis data processing.**

Sample Name (%ilm40:%SCO)	$\gamma$	$\sigma_{\text{shear}}$ (MPa)	$\epsilon$	$\sigma_{\text{axial}}$ equivalent (MPa)	Viscosity	Multiples of Uniform Distribution (MUD) range								M-Index Ilm40	M-Index SCO
						Ilm40 (0001)	SCO (100)	SCO (010)	SCO (001)						
<b>LMO-001</b> (100:0)	3.11	45.91	1.41	79.52	6.08E+12	19	0.0055	--	--	--	--	--	--	0.3386	--
<b>LMO-002</b> (10:90)	0.9	64.55	0.53	111.81	8.62E+12	2.1	0.35	2.2	0.38	2.9	0.4	1.6	0.4	0.0128	0.0208
<b>LMO-003</b> (10:90)	2.38	55.87	1.39	96.77	7.38E+12	2.6	0.25	3.2	0.2	4.3	0.17	1.9	0.33	0.031	0.0551
<b>LMO-004</b> (50:50)	2.24	59.32	1.29	102.75	7.85E+12	4.1	0.28	1.8	0.61	2	0.54	1.5	0.52	0.0623	0.01
<b>LMO-005</b> (25:75)	2.24	94.11	1.15	163	1.25E+13	5	0.21	2	0.5	2	0.48	1.5	0.57	0.0865	0.0162
<b>LMO-010</b> (25:75)	1.05	13.45	0.47	23.3	1.77E+12	--	--	--	--	--	--	--	--	--	--
<b>LMO-011</b> (25:75)	1.2	1.98	0.41	3.34	2.31E+11	--	--	--	--	--	--	--	--	--	--

$\gamma$  = total accumulated shear strain  
 $\epsilon$  = total accumulated axial equivalent strain

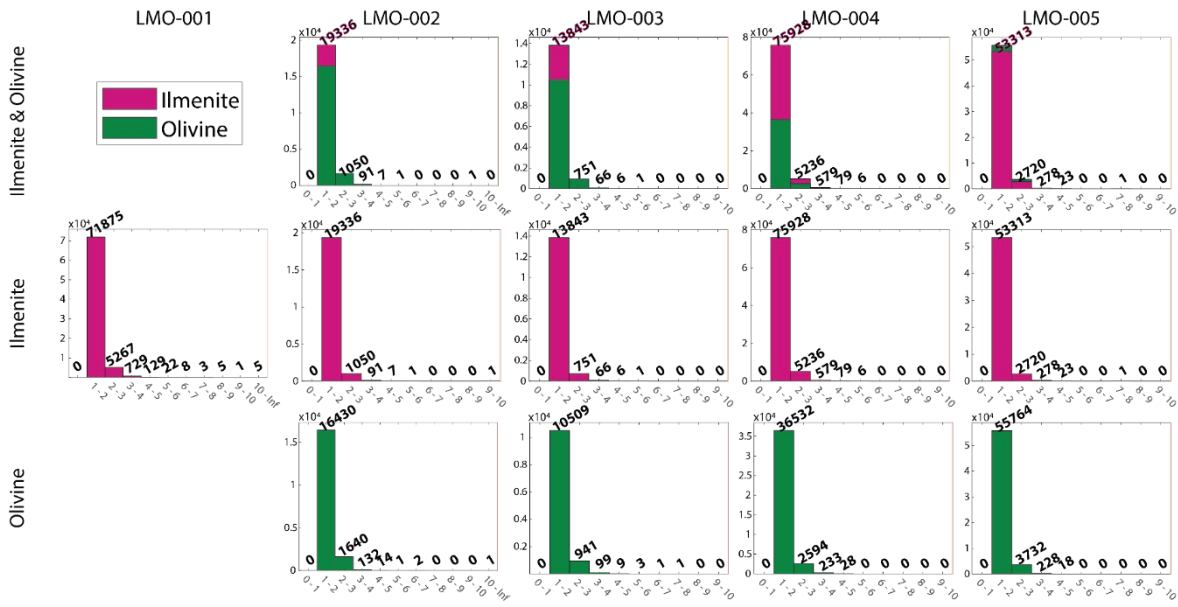


Figure 2.14. Histograms of aspect ratio for samples analyzed with EBSD. The top row of histograms show both minerals in aggregate samples, with comparison of total grains. Individual mineral aspect ratio histograms are shown the combined plot for each sample, with pink histogram bars representing ilmenite and green bars representing olivine. Grains were defined using an angle of 10 degrees.



pressure at 1000°C and a  $P_{O_2} \sim 10^{-11}$  atm. The starting  $C_{OH}$  of SCO was not measured prior to deformation and therefore, to initially calculate predicted viscosities of 100% SCO from published flow laws, we use a lower bound estimate of 50 H/10<sup>6</sup>Si and an upper bound estimate of 600 H/10<sup>6</sup>Si based on FTIR measurements of SCO pre- and post-deformation in other Griggs-style apparatus studies from the same lab (Holyoke-III, 2005; N. Zhao et al., 2019).

The calculated effective viscosity is:

$$\mu_{eff} = \frac{\sigma}{\dot{\epsilon}} \quad (3)$$

at experimental conditions for a low-water ( $C_{OH}=50$  ppm H/Si) olivine estimate sample is  $4.87 \times 10^{13}$  Pa\*s and  $2.08 \times 10^{13}$  Pa\*s for high-water ( $C_{OH}=600$  ppm H/Si) olivine estimates.

### 5.1.2 Ilmenite Flow Laws

Tokle et al. (2021) used Griggs apparatus and deformation-DIA apparatus axial compression experiments on varying Mg-content ilmenites to calibrate a pressure-dependent flow law for ilmenite 100 (ilm100; FeTiO<sub>3</sub>) using new observations and data from Dygert et al. (2016), and to establish a pressure-dependent flow law for ilm40 in axial compression. Using equation 1, the flow law for ilm40, the species used in this study, has the following parameters:  $A = 3.936 \times 10^{-7}$  MPa<sup>-n</sup>s<sup>-1</sup>,  $n = 5.7$ ,  $E = 283$  kJ/mol and  $V = 26 \times 10^{-6}$  m<sup>3</sup>/mol. With  $\epsilon$ ,  $P$ ,  $R$ , and  $T$  as defined for the olivine flow law, the bounding flow-law values can be calculated for a sample of 100% ilm40. The calculated effective viscosity at experimental conditions for a 100% ilm40 sample is  $\mu_{eff} = 1.24 \times 10^{13}$  Pa\*s.

### 5.2 Stress and strain comparisons to published flow laws

By comparing observed stresses and strains of samples in this study to the wet olivine flow law (Hirth & Kohlstedt (2003),  $C_{OH} = 50$  ppm H/Si &  $C_{OH} = 600$  ppm H/Si), ilm100 (Dygert et al., 2016; Tokle et al., 2021) and ilm40 (Tokle et al., 2021) flow law in Figure 2.5a, we see decreased strength in all samples run for this study than those predicted by the individual mineral flow laws. When interpreting these results, it is important to consider that the flow laws are calibrated from axial compression experiments in all individual mineral cases, whereas samples in this study were ran in

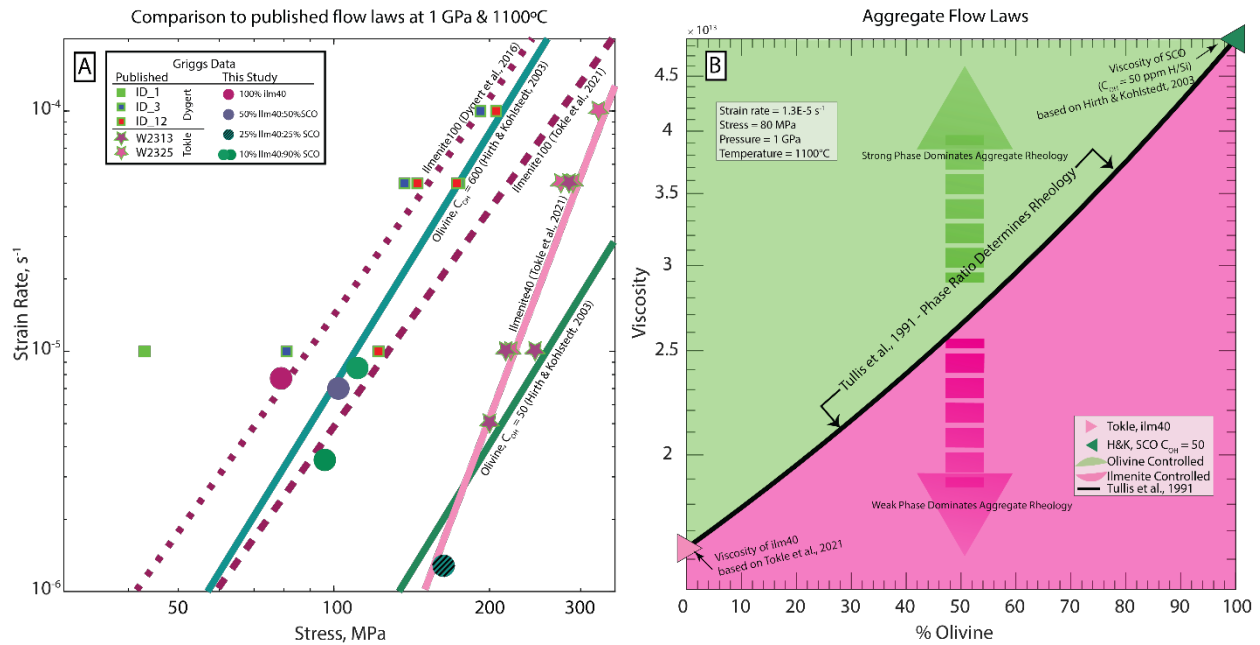


Figure 2.15. (A) Stress versus strain rate plot of published flow laws for ilm100 (Dygart et al., 2016; Tokle et al., 2021), ilm40 (Tokle et al., 2021) and wet olivine (Hirth & Kohlstedt, 2003), plotted with individual experiment data from past studies and this study. Squares represent data for ilm100 from Dygart et al. (2016), stars are ilm40 data from Tokle et al. (2021) and circles are this study. (B) Percent olivine on the x-axis versus logarithmic scale of viscosity on the y-axis. This plot shows the predicted viscosities for samples of 100% ilm40 on the left and 100% SCO on the right edges of the plot based on published flow laws (Hirth & Kohlstedt, 2003; Tokle et al., 2021). The black line shows the mixing model of the two phases as calculated by Tullis et al. 1991. Any sample data that plots in the pink region of the graph has a rheology controlled by the weak phase, ilmenite. If data plots in the green region of the graph, its rheology is controlled by the strong phase, olivine.

general shear. Previous studies on olivine in general shear, performed on Griggs-type apparatus have shown decreased differential stresses, especially in cases of high strain (Holyoke-III, 2005; Post, 1977). While this weakening has been observed and published in experimental data, no flow law exists for olivine or ilmenite deformed in shear.

Figure 2.5b shows the predicted range of aggregate viscosities from the published ilm40 and olivine flow laws, as triangles on the left and right y-axes of the plot, respectively. Among published models of aggregate flow laws, the empirical Tullis et al. (1991) two-phase mixing model represents an aggregate flow law that is a function of by the volume-weighted averages of the endmember phase components. We show the Tullis et al. (1991) mixing model as dividing two regimes for aggregate rheology. In cases where the strength of the aggregate is controlled by the stronger material, olivine in this case, experimental observations would fall above the Tullis et al. (1991) line in the green region, and viscosities predicted if the strength of the aggregate is controlled by the weaker phase of the two, ilmenite in this case, which would plot beneath the Tullis et al. (1991) line, in the pink field. The figure is schematic. Because ilm40 has a very different rheology in shear than in axial compression (Fig. 2.5a), and olivine water contents are unknown, it is not possible to determine where the aggregate experiments plot in relation to the Tullis et al (1991) or other aggregate mixing models.

### *5.2.1 Uncertainty in water content of experimental materials*

All samples were prepared and conditioned at reducing conditions and stored in a low temperature ( $\sim 100^\circ\text{C}$ ) vacuum oven between packing and experimental assembly. While best efforts were made to keep samples free of absorbed water,  $C_{\text{OH}}$  values are unknown, and they would affect the flow law and aggregate mixing model predictions. To account for the uncertainty in these values, aggregate flow laws were calculated for a range of  $C_{\text{OH}}$  in olivine between  $50 \text{ H}/10^6 \text{ Si}$  and  $600 \text{ H}/10^6 \text{ Si}$ . These values are an expanded range from the values measured in SCO using FTIR in other studies from the Brown University Rock Deformation Lab (Holyoke-III, 2005; N. Zhao et al., 2019). Using the EBSD data from olivine, water contents were also estimated from Bernard et al. (2019), which employs a water content correction from previously preferred calibrations made by Bell et al. (2003), and the proposed olivine fabric-type

transitions from Jung & Karato (2001). At highest total accumulated strain, CPOs appear to follow a B-type pattern. While this type covers a wide range of possible ppm H/Si, lower stress samples appear to show some A-type behavior, leading to us to estimate  $C_{OH}$  values no higher than 1000, although CPOs do not match A-type for all three orientations. Because of the preparation in reducing conditions and lack of any external hydrating materials, 1000 ppm H/Si can be considered in excess of experimental values.

### *5.2.2 Anomalous strength/weakness in 25% ilm40:75% SCO samples not reproducible*

The 25:75 sample, LMO-005, sustained anomalously high differential stresses in comparison to all other shear experiments run in the same session. Nearly two years later, repeat attempts to measure the strength of the same phase proportions in samples LMO-010 and LMO-011 returned anomalously low stress and viscosity values, all shown by blue dots in Figure 2.5b. There is no indication that the strength variations in this specific phase proportion are significant, but because of the variation, especially in comparison to the values from other experiments, this ratio of ilm40:SCO should be further investigated in future studies. Compositional mapping of the anomalous samples could tell us if the samples experienced a salt leak, or some other form of mechanical weakening during experimental deformation.

### **5.3 Post-deformation fabrics**

Post-deformation analysis of samples in photomicrograph and via BSE from SEM data collection show changes in fabric strength with increased total strain. Total strain ( $\gamma$  and  $\epsilon$ ) and stress ( $\sigma$ ) for all experiments are presented in Table 2.3, along with the calculated viscosity based on the axial equivalent differential stresses and strain rates (Paterson & Olgaard, 2000), and the multiples of uniform distribution (MUD) range for each pole figure shown in Figure 2.3, and M-index values relevant to each experiment that was analyzed by EBSD.

#### *5.3.1 Olivine*

Olivine CPOs for (100), (010), and (001) were used to compare to the fabric-types outlined in Figure 1 of Bernard et al. (2019). In the low strain 10:90 ilm40:SCO sample, LMO-002, fabric development is weak in all planes, but most pronounced in the

(010). In the high strain 10:90 ilm40:SCO sample, LMO-003, fabric development is strongest in the (010) plane parallel to the shear direction and is also evident in (100) normal to the shear direction. The grain geometry of both 10:90 samples is shown in grain area and aspect ratio maps in Supplementary Figure 2.6, with ilmenite and olivine in separate maps, along with backscatter micrographs for representative sections of the samples. The higher strain sample appears to show more grain elongation in the direction of shear for ilmenite, while grain shape is less elongate in the low strain sample. This visual interpretation is not supported by MTEX aspect ratio analysis (Figure 2.4). According to the M-index for both 10:90 samples, fabric development is stronger in SCO with higher accumulated strain, and in samples with higher percentages of SCO.

Based on total accumulated strain ( $\gamma$ ), the olivine containing samples run on EBSD show increasingly defined CPOs with increasing strain, especially along the [010] axes. Girdling can also be seen in the [100] and [001] axes CPO, as shown in Figure 2.3. Between the 10:90 ilm40:SCO and lower proportion SCO samples, the (010) plane rotates around the C-axis by approximately 45° to 90°.

### 5.3.2 Ilmenite

To compare the orientation trends of ilmenite, c-axis, basal-plane was plotted in CPOs based on recent studies of ilmenite inclusions and single crystals (Griffiths et al., 2016; J. L. Till & Rybacki, 2020). Comparison of the basal plane orientation (0001) of ilmenite in all samples that were analyzed with EBSD shows CPO strengthening for the samples with 25% - 100% ilmenite. As seen in column one of Figure 2.3, sample LMO-001 shows well defined poles in the (0001) plane. For comparison between samples, the same multiples of uniform distribution (MUD) color scale was used between 0 and 5, but the maximum for LMO-001 was much greater than all other samples when plotted individually, at 19. The MUD values for all sample pole figures are reported in Table 2.3.

A decrease is seen in the ilm40 M-index between 100% ilm40 and all samples containing both ilm40 and SCO. While no trend occurs between 50:50, 25:75 and 10:90 ilm40:SCO ilm40 M-index values (final columns of Table 2.3), the two samples with 10% ilm40 have lower M-index values than the 50% and 25% ilm40 samples which could

signify a shift in the phase that dominates the rheology of the system from ilm40 to SCO between those values. Increased experimental density would allow for the quantification of the magnitude change in M-index with decreasing ilm40 content and could imply that deformation transitions to being predominantly accommodated by the stronger phase.

## 6. Summary and Conclusions

Through a series of general shear molten salt cell experiments on varied ratios of ilm40 and SCO in a Griggs-type deformation apparatus, we investigated the deformation of two-phase aggregate rocks analogous to the lunar mantle. Ilm40 to SCO ratios of 100:0, 50:50, 75:25, and 10:90 were used in this study. Based on the mechanical data results of samples LMO-001, LMO-002, LMO-003, LMO-004, LMO-005, LMO-010, and LMO-011, combined with the EBSD data from LMO-001, LMO-002, LMO-003, LMO-004 and LMO-005, there is no clear quantifiable trend for refining an ilm40:SCO aggregate flow law to represent the rheology of the system, but measurement of the  $C_{OH}$  of the SCO and establishing the behavior of the two minerals in shear as compared to their axial compression constrained flow laws would be useful in this process. With an increased density of mechanical data at ilm40:SCO ratios between 50:50 and 0:100, it should be possible to move towards determining the dominant phase controlling deformation, and possibly parameterizing an aggregate flow law. Future work, including analyses the  $C_{OH}$  of SCO used in these experiments using FTIR and refinement of the experimental setup to allow for longer deformation without thermocouple failure, would provide better resolution about the trend of the mixing rheology.

The results of the Griggs-apparatus experiments and corresponding microstructural analysis of select samples in this study lead us to conclude that shear deformation of samples causes weakening compared to axial compression constrained flow laws ilm40 and confirms findings by previous studies that SCO is weakened by deformation in shear. Fabric seen in the ilm40 suggest this occurs when slip can be facilitated along the basal plane, in agreement with Till & Rybacki (2020) and SCO fabric strengthens with strain and weakens with added ilm40 percentages. Further

experiments in the aggregate ratios of 50:50 to 0:100 could help to constrain a robust aggregate flow law and inform future work on the overturn in the lunar mantle.

## **7. Acknowledgments, Samples, and Data**

This project was funded by a Solar Systems Workings NASA Grant 80NSSC18K0249 to GH (PI), ND (Co-PI) & YL (Co-PI). We would like to acknowledge the invaluable assistance of Eric Burdette and Ningli Zhao during experimental work at Brown University.

## References

- Andersen, D. J., & Lindsley, D. H. (1979). The olivine-ilmenite thermometer. *Lunar Planetary Science Conference, 10*, 493–507. <https://doi.org/1979LPSC...10..493A>
- Bachmann, F., Hielscher, R., & Schaeben, H. (2011). Grain detection from 2d and 3d EBSD data-Specification of the MTEX algorithm. *Ultramicroscopy, 111*(12), 1720–1733. <https://doi.org/10.1016/j.ultramic.2011.08.002>
- Bell, D. R., Rossman, G. R., Maldener, J., Endisch, D., & Rauch, F. (2003). Hydroxide in olivine: A quantitative determination of the absolute amount and calibration of the IR spectrum. *Journal of Geophysical Research: Solid Earth, 108*(B2), 1–9. <https://doi.org/10.1029/2001jb000679>
- Bernard, R. E., Behr, W. M., Becker, T. W., & Young, D. J. (2019). Relationships Between Olivine CPO and Deformation Parameters in Naturally Deformed Rocks and Implications for Mantle Seismic Anisotropy. *Geochemistry, Geophysics, Geosystems*. <https://doi.org/10.1029/2019gc008289>
- Bevillard, B., Richard, G., & Raimbourg, H. (2019). Rock Strength and Texture Evolution During Deformation in the Earth's Ductile Lithosphere: A Two-Phase Thermodynamics Model. *Geochemistry, Geophysics, Geosystems, 20*(2), 1095–1137. <https://doi.org/10.1029/2018GC007881>
- Charlier, B., Grove, T. L., Namur, O., & Holtz, F. (2018). Crystallization of the lunar magma ocean and the primordial mantle-crust differentiation of the Moon. *Geochimica et Cosmochimica Acta, 234*, 50–69. <https://doi.org/10.1016/j.gca.2018.05.006>
- Dimanov, A., & Dresen, G. (2005). Rheology of synthetic anorthite-diopside aggregates: Implications for ductile shear zones. *Journal of Geophysical Research: Solid Earth, 110*(7), 1–24. <https://doi.org/10.1029/2004JB003431>
- Dygert, N., Hirth, G., & Liang, Y. (2016). A flow law for ilmenite in dislocation creep: Implications for lunar cumulate mantle overturn. *Geophysical Research Letters, 43*(2), 532–540. <https://doi.org/10.1002/2015GL066546>
- Elardo, S. M., Draper, D. S., & Shearer, C. K. (2011). Lunar Magma Ocean crystallization revisited: Bulk composition, early cumulate mineralogy, and the source regions of the highlands Mg-suite. *Geochimica et Cosmochimica Acta, 75*(11), 3024–3045. <https://doi.org/10.1016/j.gca.2011.02.033>
- Elkins-Tanton, L. T., Burgess, S., & Yin, Q. Z. (2011). The lunar magma ocean: Reconciling the solidification process with lunar petrology and geochronology. *Earth and Planetary Science Letters, 304*(3–4), 326–336. <https://doi.org/10.1016/j.epsl.2011.02.004>
- Faul, U. H., Cline, C. J., David, E. C., Berry, A. J., & Jackson, I. (2016). Titanium-hydroxyl defect-controlled rheology of the Earth's upper mantle. *Earth and Planetary Science Letters, 452*, 227–237. <https://doi.org/10.1016/j.epsl.2016.07.016>



- Goetze, C., & Poirier, J. P. (1978). The mechanisms of creep in olivine. *Philosophical Transactions of the Royal Society of London. Series A, Mathematical and Physical Sciences*, 288(1350), 99–119. <https://doi.org/10.1098/rsta.1978.0008>
- Gonçalves, C. C., Gonçalves, L., & Hirth, G. (2015). The effects of quartz recrystallization and reaction on weak phase interconnection, strain localization and evolution of microstructure. *Journal of Structural Geology*, 71, 24–40. <https://doi.org/10.1016/j.jsg.2014.11.010>
- Griffiths, T. A., Habler, G., & Abart, R. (2016). Crystallographic orientation relationships in host-inclusion systems: New insights from large EBSD data sets. *American Mineralogist*, 101(3), 690–705. <https://doi.org/10.2138/am-2016-5442>
- Handy, M. R. (1990). The solid-state flow of polymineralic rocks. *Journal of Geophysical Research*, 95(B6), 8647. <https://doi.org/10.1029/JB095iB06p08647>
- Handy, M. R. (1994). Flow laws for rocks containing two non-linear viscous phases: A phenomenological approach. *Journal of Structural Geology*, 16(3), 287–301. [https://doi.org/10.1016/0191-8141\(94\)90035-3](https://doi.org/10.1016/0191-8141(94)90035-3)
- Hansen, L. N., Zimmerman, M. E., & Kohlstedt, D. L. (2011). Grain boundary sliding in San Carlos olivine: Flow law parameters and crystallographic-preferred orientation. *Journal of Geophysical Research: Solid Earth*, 116(8), 1–16. <https://doi.org/10.1029/2011JB008220>
- Herwegh, M., Linckens, J., Ebert, A., Berger, A., & Brodhag, S. H. (2011). The role of second phases for controlling microstructural evolution in polymineralic rocks: A review. *Journal of Structural Geology*, 33(12), 1728–1750. <https://doi.org/10.1016/j.jsg.2011.08.011>
- Hess, P., & Parmentier, E. M. (1995). A model for the thermal and chemical evolution of the Moon's interior: implications for the onset of mare volcanism. *Earth and Planetary Science Letters*, 134(3–4), 501–514. [https://doi.org/10.1016/0012-821X\(95\)00138-3](https://doi.org/10.1016/0012-821X(95)00138-3)
- Hirth, G., & Kohlstedt, D. L. (2003). Rheology of the upper mantle and the mantle wedge: A view from the experimentalists. In J. M. Eiler (Ed.), *Inside the Subduction Factory, Volume 138* (pp. 83–105). American Geophysical Union. <https://doi.org/10.1029/138GM06>
- Holyoke-III, C. W. (2005). Strain weakening in crustal and upper mantle lithologies: processes and consequences. *Ph.D. Dissertation*, (May), 1–243. Retrieved from <http://proquest.umi.com/pdf/ed318d8c64123dcc26a142066ba3e138/1314663180//share4/pqimage/pqirs101v/201108291942/40887/26838/out.pdf%5Cnpapers3://publication/uuid/CBCF8467-87D4-4C90-A046-0B6521715B07>
- Huet, B., Yamato, P., & Grasemann, B. (2014). The Minimized Power Geometric model: An analytical mixing model for calculating polyphase rock viscosities consistent with experimental data. *Journal of Geophysical Research: Solid Earth*, 119(4), 3897–3924. <https://doi.org/10.1002/2013JB010453>
- Jordan, P. G. (1987). The deformational behaviour of bimineralic limestone-halite aggregates. *Tectonophysics*, 135(1–3), 185–197. [https://doi.org/10.1016/0040-1951\(87\)90160-0](https://doi.org/10.1016/0040-1951(87)90160-0)
- Jung, H., & Karato S. (2001). Water-Induced Fabric Transitions in Olivine. *Science*, 293(5534), 1460–1463. <https://doi.org/10.1126/science.1062235>

- Kohlstedt, D. L., & Goetze, C. (1974). Low-stress high-temperature creep in olivine single crystals. *Journal of Geophysical Research*, 79(14), 2045–2051. <https://doi.org/10.1029/jb079i014p02045>
- Maurice, M., Tosi, N., Schwinger, S., Breuer, D., & Kleine, T. (2020). A long-lived magma ocean on a young Moon. *Science Advances*, 6(28). <https://doi.org/10.1126/sciadv.aba8949>
- Michaut, C., & Neufeld, J. A. (2022). Formation of the Lunar Primary Crust From a Long-Lived Slushy Magma Ocean. *Geophysical Research Letters*, 49(2). <https://doi.org/10.1029/2021GL095408>
- Paterson, M. S., & Olgaard, D. L. (2000). Rock deformation tests to large shear strains in torsion. *Journal of Structural Geology*, 22(9), 1341–1358. [https://doi.org/10.1016/S0191-8141\(00\)00042-0](https://doi.org/10.1016/S0191-8141(00)00042-0)
- Peč, M. (2010). RIG : a MATLAB TM program for evaluation of mechanical data from experimental apparatuses.
- Platt, J. P. (2015). Rheology of two-phase systems: A microphysical and observational approach. *Journal of Structural Geology*, 77, 213–227. <https://doi.org/10.1016/j.jsg.2015.05.003>
- Post, R. L. (1977). High-temperature creep of Mt. Burnet Dunite. *Tectonophysics*, 42(2–4), 75–110. [https://doi.org/10.1016/0040-1951\(77\)90162-7](https://doi.org/10.1016/0040-1951(77)90162-7)
- Shearer, C. K., Hess, P., Wiczorek, M. A., Pritchard, M. E., Parmentier, E. M., Borg, L. E., et al. (2006). Thermal and Magmatic Evolution of the Moon. *Reviews in Mineralogy and Geochemistry*, 60(1), 365–518. <https://doi.org/10.2138/rmg.2006.60.4>
- Skemer, P., Katayama, I., Jiang, Z., & Karato, S. I. (2005). The misorientation index: Development of a new method for calculating the strength of lattice-preferred orientation. *Tectonophysics*, 411(1–4), 157–167. <https://doi.org/10.1016/j.tecto.2005.08.023>
- Snyder, G. A., Taylor, L. A., & Neal, C. R. (1992). A chemical model for generating the sources of mare basalts: Combined equilibrium and fractional crystallization of the lunar magmasphere. *Geochimica et Cosmochimica Acta*, 56(10), 3809–3823. [https://doi.org/10.1016/0016-7037\(92\)90172-F](https://doi.org/10.1016/0016-7037(92)90172-F)
- Stipp, M., Stünitz, H., Heilbronner, R., & Schmid, S. M. (2002). Dynamic recrystallization of quartz: Correlation between natural and experimental conditions. *Geological Society Special Publication*, 200(October 2002), 171–190. <https://doi.org/10.1144/GSL.SP.2001.200.01.11>
- Thacker, C., Liang, Y., Peng, Q., & Hess, P. (2009). The stability and major element partitioning of ilmenite and armalcolite during lunar cumulate mantle overturn. *Geochimica et Cosmochimica Acta*, 73(3), 820–836. <https://doi.org/10.1016/j.gca.2008.10.038>
- Till, J., & Moskowitz, B. (2013). Magnetite deformation mechanism maps for better prediction of strain partitioning. *Geophysical Research Letters*, 40(4), 697–702. <https://doi.org/10.1002/grl.50170>
- Till, J. L., & Rybacki, E. (2020). High-temperature creep of magnetite and ilmenite single

crystals. *Physics and Chemistry of Minerals*, 47(12), 1–16. <https://doi.org/10.1007/s00269-020-01122-6>

Tokle, L., Hirth, G., & Behr, W. M. (2019). Flow laws and fabric transitions in wet quartzite. *Earth and Planetary Science Letters*, 505, 152–161. <https://doi.org/10.1016/j.epsl.2018.10.017>

Tokle, L., Hirth, G., Liang, Y., Raterron, P., & Dygert, N. (2021). The Effect of Pressure and Mg-Content on Ilmenite Rheology: Implications for Lunar Cumulate Mantle Overtum. *Journal of Geophysical Research: Planets*, 126(1), 1–21. <https://doi.org/10.1029/2020JE006494>

Tullis, J., & Wenk, H. R. (1994). Effect of muscovite on the strength and lattice preferred orientations of experimentally deformed quartz aggregates. *Materials Science and Engineering A*, 175(1–2), 209–220. [https://doi.org/10.1016/0921-5093\(94\)91060-X](https://doi.org/10.1016/0921-5093(94)91060-X)

Tullis, T. E., Horowitz, F. G., & Tullis, J. (1991). Flow laws of polyphase aggregates from end-member flow laws. *Journal of Geophysical Research*, 96(B5), 8081–8096. <https://doi.org/10.1029/90JB02491>

Zhao, N., Hirth, G., Cooper, R. F., Kruckenberg, S. C., & Cukjati, J. (2019). Low viscosity of mantle rocks linked to phase boundary sliding. *Earth and Planetary Science Letters*, 517, 83–94. <https://doi.org/10.1016/j.epsl.2019.04.019>

Zhao, Y. H., Zimmerman, M. E., & Kohlstedt, D. L. (2009). Effect of iron content on the creep behavior of olivine: 1. Anhydrous conditions. *Earth and Planetary Science Letters*, 287(1–2), 229–240. <https://doi.org/10.1016/j.epsl.2009.08.006>

## Appendix

### Appendix 1. Supplemental Figure

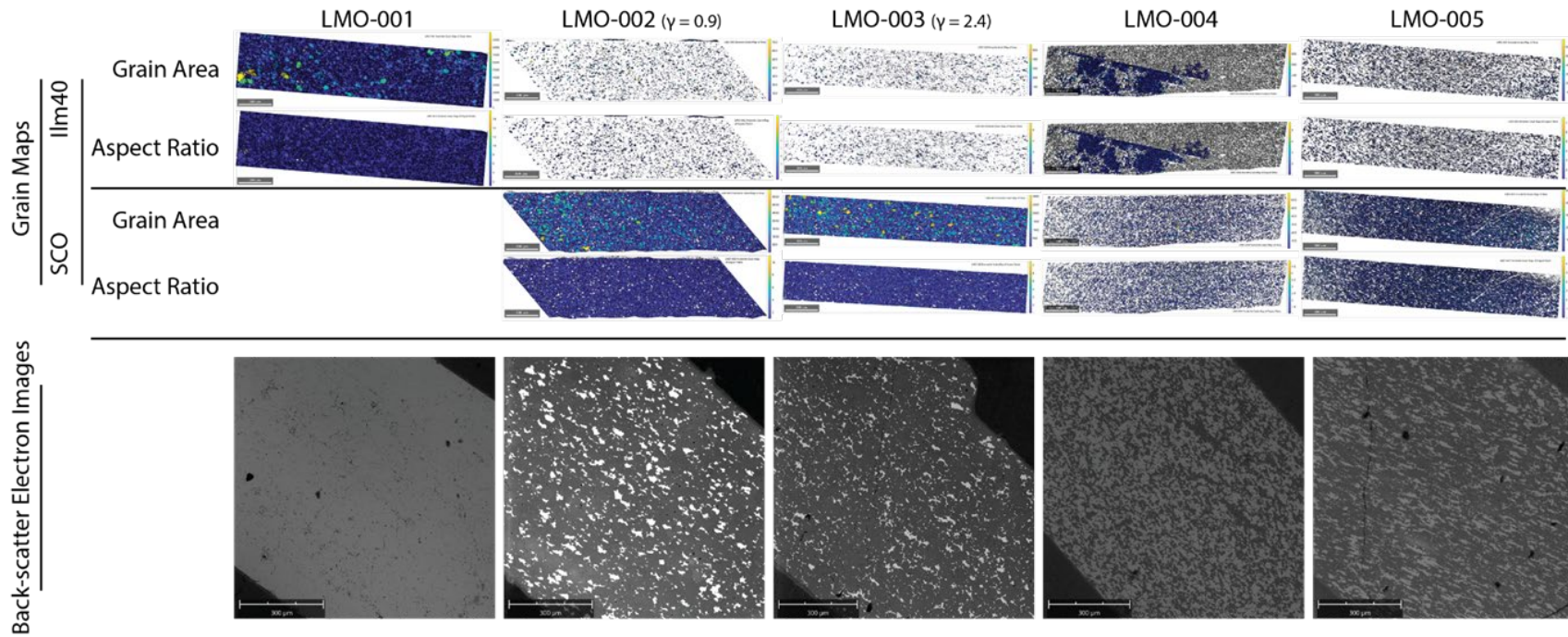


Figure 2.6. Grain maps for ilm40 and SCO for samples LMO-001, LMO-002, LMO-003, LMO-004, & LMO-005, with color scaling for grain area (top) and aspect ratio (middle) based on a 10-degree misorientation in grain data from EBSD. Back-scatter electron images of samples (bottom). Bright phase is ilm40, gray phase is SCO. Dark corners are  $\text{Al}_2\text{O}_3$  piston.

**Chapter 3: Building Carbon minerals: Application of geoscience learning materials to the Tennessee Academic Standards for Science for Chemistry I for use in public school classrooms**

A version of this chapter is in the final stages of preparation for submission to the journal *The Science Teacher* by Nadine Lynne Grambling, Stephanie K. Drumheller, and Kristin T. Rearden.

Nadine Lynne Grambling led conceptualization, writing, and development of this article. Stephanie K. Drumheller supervised the direction of this article and led revisions. Kristin T. Rearden assured the content aligned with State of Tennessee education standards and assisted in revisions.

## **Abstract**

Native minerals refer to natural materials that form repeating crystalline structures from a single element of the periodic table. One element with two widely known native minerals is carbon, forming the mineral graphite at relatively low temperatures and pressures, and diamond at much higher temperatures and pressures, such as those seen deep in the Earth. Most secondary school students will be aware of both minerals, which provides a fantastic opportunity to discuss the relationships between crystal structure, atomic bonds, phase changes, physical properties of materials and the interior structure of the Earth.

## **1. Introduction**

The Tennessee Academic Standards for Science (referred to henceforth as “the standards”) were published in 2018, based on the Next Generation Science Standards (NGSS) which integrate the concepts set forth in A Framework for K-12 Science Education from the National Research Council (“A Framework for K-12 Science Education: Practices, Crosscutting Concepts, and Core Ideas,” 2012; NGSS Lead States, 2017; Tennessee Department of Education, 2018). The Tennessee standards are split in to four disciplinary core ideas (DCIs): Physical Sciences (PS), Life Sciences (LS), Earth and Space Sciences (ESS) and Engineering, Technology, and Applications of Science (ETS). They also integrate seven crosscutting concepts of: patterns; cause and effect; scale, proportion, and quantity; systems and system models; energy and matter; structure and function of systems; and stability and change of systems. These

crosscutting relationships are written to connect between the sciences across all grade levels.

At the high school level, students are required to take three years of science courses: 1 biology credit, 1 physics or chemistry credit, and 1 additional credit of lab science from LS, PS, or ESS. The final required ESS coursework in the standards is in grade 8, with eight total across ESS1, ESS2, & ESS3. While students have the option to choose ESS classes in high school, this depends on course availability, and teaching expertise of educators. To integrate ESS concepts into the high school curriculum, a group of investigators at the University of Tennessee Knoxville have been awarded funds to create lesson plans with materials for distribution, “Lessons-In-A-Box”, through the Knox County Public Library System. These lesson plans use the standards for physics, chemistry and/or biology to aid educators in teaching Earth sciences concepts as they relate to their courses specific DCIs.

The following lesson plan write up is aimed at CHEM1 or CHEM2 classrooms, covering the standards listed in Table 3.1. CHEM1.PS3.2 and CHEM2.PS1.3 are highlighted with bold and italic formatting in Table 3.1 to signify that they are the two most relevant standards covered in the lesson.

## **2. Background**

When asked where diamonds come from, most of the population will think of coal being buried deep in the Earth to become the gems that are popular in jewelry and industrial applications. While the idea of dinosaurs becoming diamonds can be fun in concept, the youngest diamonds we see on Earth’s surface today are almost 1 billion years old, an age older than the appearance of terrestrial plants and animals in the fossil record (Harris, 1993). It is much more likely that diamonds originate from carbon that has spent its entire history deep within the Earth, first seeing the surface in the form we see now (Harris, 1993). The more likely product of coal being heated and confined is another well known mineral: graphite.

This activity asks students to think about what happens to materials as they move through the layers of the Earth, from the surface to the core. Students will compare the

Table 3.1. Standards relevant to "Building Carbon Minerals" lesson plan

Course	DCI	Standard	
CHEM1	PS1	12	Explain the origin and organization of the Periodic Table. Predict chemical and physical properties of main group elements (reactivity, number of subatomic particles, ion charge, ionization energy, atomic radius, and electronegativity) based on location on the periodic table. Construct an argument to describe how the quantum mechanical model of the atom (e.g., patterns of valence and inner electrons) defines periodic properties. Use the periodic table to draw Lewis dot structures and show understanding of orbital notations through drawing and interpreting graphical representations (i.e., arrows representing electrons in an orbital).
			PS2
	PS3	1	Contrast the concepts of temperature and heat in macroscopic and microscopic terms. Understand that thermal energy is a form of energy and temperature is a measure of average kinetic energy of a group of particles.
		2	<b><i>Draw and interpret heating and cooling curves and phase diagrams. Analyze the energy changes involved in calorimetry by using the law of conservation of energy quantitatively (use of <math>q = mc\Delta T</math>) and qualitatively.</i></b>
CHEM2	PS1	3	<b><i>Compare and contrast crystalline and amorphous solids with respect to particle arrangement, strength of bonds, melting and boiling points, bulk density, and conductivity; provide examples of each type. 10. Obtain, evaluate, and communicate information about how carbon's structure and function are used and have influenced society.</i></b>
	PS2	1	Plan and conduct an investigation to compare the properties of the different types of intermolecular forces in pure substances and in components of a mixture.
		2	Make predictions regarding the relative magnitudes of the forces acting within collections of interacting molecules based on the distribution of electrons within the molecules and types of intermolecular forces through which the molecules interact.



pressures and temperatures seen at different depths below Earth's surface to a phase diagram for carbon, which shows solid-solid phase transitions. After making conceptual assessments of available data, students can use materials to build 3-dimensional representations of the crystal lattices for graphite and diamond. These models allow students to visualize the changes in bond angles between the two minerals, helping to physically connect the nanoscopic effects of pressure and temperature on atomic arrangements and geometries in crystal lattices.

### 3. Layering the Earth

Start the lesson by discussing the interior structure of the Earth. Depending on their backgrounds, students may know the layers based on the chemical structure [*Crust > Mantle > Outer Core > Inner Core*] or physical structure [*Lithosphere > Asthenosphere > Mantle > Outer Core > Inner Core*] but their familiarity with the names of layers may range widely depending on the interpretation of the middle school Earth's Systems Performance Expectation Code (MS-ESS2-1, MS-ESS2-2 & MS-ESS2-3, (NGSS Lead States, 2017)). For this lesson, I have written materials using the chemical structure [*Crust > Mantle > Outer Core > Inner Core*] with the aim of distribution of materials to secondary chemistry classrooms where physical properties are not the focus.

Scientists can estimate the pressure and temperature values deep in the Earth based on many previous studies, such as changes in seismic waves from earthquakes through different layers (e.g. Herak & Herak, 2007), attempts at deep drilling into the crust (e.g. Bascom, 1959) and lab experiments on rocks and minerals (e.g. Sarafian et al., 2017). Table 3.1 provides useful numerical values to view in comparison to visual relationships in Figure 3.1, which plots ranges of temperatures and pressures with depth from the surface (based on Carlson et al., 2010).

After discussing Earth's layers and their range of physical parameters, you can discuss the major chemical composition of each layer using Table 3.2. This compares the major minerals and materials of each layer of the Earth, including the chemical

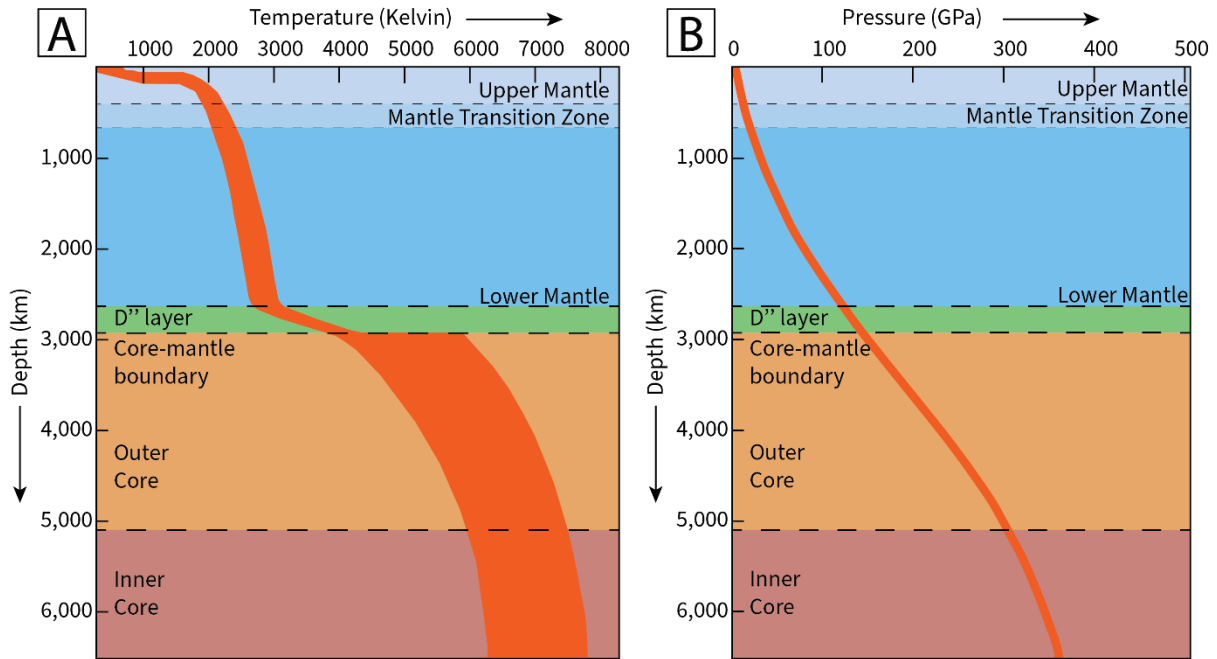


Figure 3.1. Depth into the Earth in kilometers (km) versus Temperature in Kelvin (A) and Pressure in gigapascals (GPa) (B). The average boundary thickness of the Upper Mantle, Mantle Transition Zone, Lower Mantle, D double prime (D'') layer, Outer Core and Inner Core are shown by dashed lines.

Table 3.2. Layers of the Earth, depths from the surface, and their major mineralogy.

<b>Region (depths)</b>	<b>Mineralogy</b>
<b>Crust (average depth 40 km)</b>	<ul style="list-style-type: none"> <li>✓ Feldspar [<math>\text{KAlSi}_3\text{O}_8</math> – <math>\text{NaAlSi}_3\text{O}_8</math> – <math>\text{CaAl}_2\text{Si}_2\text{O}_8</math>],</li> <li>✓ Quartz [<math>\text{SiO}_2</math>]</li> </ul>
<b>Upper mantle (410-40 km)</b>	<ul style="list-style-type: none"> <li>✓ Olivine [<math>\text{Fe}_2\text{SiO}_4</math>],</li> <li>✓ Pyroxene [(Ca,Na,Fe,Mg)(Cr,Al,Fe,Mg,Co,Mn,Sc,Ti,V,Fe)(Si,Al)<math>_2\text{O}_6</math>],</li> <li>✓ Garnet [<math>\text{Fe}_3\text{Al}_2\text{Si}_3\text{O}_{12}</math>],</li> <li>✓ Spinel [<math>\text{MgAl}_2\text{O}_4</math>]</li> </ul>
<b>Transition zone (670-410 km)</b>	<ul style="list-style-type: none"> <li>✓ Structures with both <math>\text{SiO}_4</math> and <math>\text{SiO}_6</math> groups, <ul style="list-style-type: none"> <li>• e.g., majorite garnet [<math>\text{Mg}_3(\text{MgSi})(\text{SiO}_4)_3</math>]</li> </ul> </li> </ul>
<b>Lower mantle (2891-670 km)</b>	<ul style="list-style-type: none"> <li>✓ Magnesio-wüstite [(Mg,Fe)O],</li> <li>✓ Magnesium silicate perovskite [(Mg,Fe)<math>\text{SiO}_3</math>],</li> <li>✓ Stishovite [(SiO<math>_2</math>)]</li> </ul>
<b>Outer core (5150- 2891 km)</b>	<ul style="list-style-type: none"> <li>✓ Liquid iron</li> </ul>
<b>Inner core (6371-5150 km)</b>	<ul style="list-style-type: none"> <li>✓ Hexagonal Close-Packed (HCP) iron</li> </ul>

formulas and phase information when relevant. One interesting point that might be brought up by students is that Carbon is not a major element in any layer within the Earth, and this is true, but it is also very important to the history of the Earth and the existence of life!

#### **4. Carbon: Phases with Relation to Earth**

Now is a great time to introduce the carbon phase diagram (Figure 3.2). I have included two versions here, one with an overlay of relevant pressure and temperature values of different depths into the Earth, as given in Table 3.3. If students have a copy of Table 3.3 available to them, providing Figure 3.2a can give them the chance to think through the change of physical properties with depth. If Table 3.3 is not simultaneously available, such as being used in a slideshow presentation when handouts are unavailable, Figure 3.2b will be helpful for group discussion. It may be important to note that the Y axis of the plot is in logarithmic scale, which makes the depth points seem to get closer and closer together as you get closer to the core of the Earth.

Either as small groups, or a whole class, ask students to name which phases of elemental carbon we should find in the Earth. Have them predict, in combination with Figure 3.1, which layers of the Earth would contain which phases, based solely on the pressures and temperatures at those depths.

Now you can reintroduce Table 3.2, which shows the major phases present in the different layers of the Earth. While we have already acknowledged that carbon is not a constituent element in any of the layers, we can consider the properties of the other phases to rule out the presence of elemental carbon minerals, specifically in the inner and outer core. While the pressures and temperatures predicted for those layers of the Earth fall within the phase diagram for carbon, the composition of the inner and outer core are unlikely to provide a hospitable environment to a crystalline carbon phase. Some relevant information on Earth System's concepts, along with their prompting questions are contained in the Pre-Activity rows of Table 3.4. It is important to review the qualifications of a mineral and native mineral with students when thinking about the chemical layers of the Earth in relation to diamond and graphite. Figure 3.3, based on Figure 4.6 from *Deep Carbon*, shows different areas of diamond formation, along with

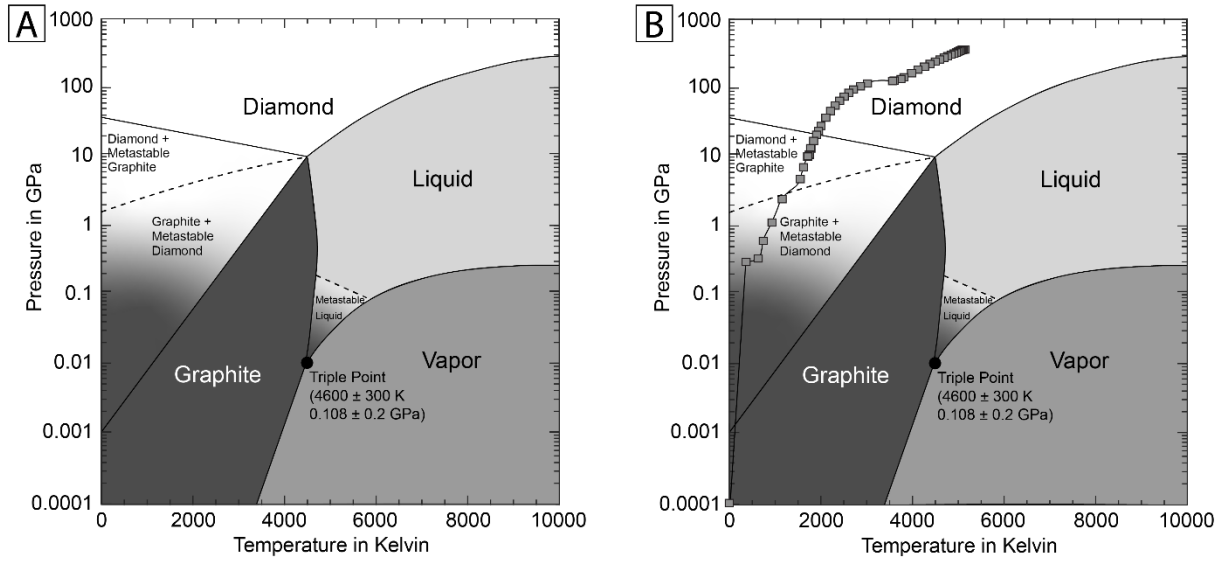


Figure 3.2. Carbon phase diagram for Earth-relevant conditions. Plot A shows just the phase diagram while plot B has an overlay of the pressure-temperature path through the Earth based on Table 3.1.

Table 3.3. Pressure and temperature at different locations within the Earth with distance from the center of Earth and distance from the surface of Earth.

The Geotherm			
Distance from the center of the Earth (km)	Distance from the surface of the Earth (km)	Pressure (GPa)	Temperature (K)
6371	0	0.0	300
6368	3	0.3	366
6356	15	0.3	630
6347	24	0.6	743
6331	40	1.1	930
6291	80	2.5	1155
6221	150	4.8	1550
6151	220	7.1	1622
6061	310	10.2	1714
6016	355	10.8	1750
5971	400	13.4	1779
5871	500	17.1	1842
5771	600	21.0	1906
5701	670	23.8	1950
5600	771	28.3	2003
5400	971	37.3	2109
5200	1171	46.5	2211
5000	1371	55.9	2313
4800	1571	65.5	2411
4600	1771	75.4	2509
4400	1971	85.4	2610
4200	2171	95.8	2712
4000	2371	106.4	2865
3800	2571	117.4	3018
3630	2741	127.0	3564
3600	2771	128.7	3601
3480	2891	135.8	3750
3400	2971	144.2	3816
3200	3171	165.1	3981
3000	3371	185.6	4123
2800	3571	205.6	4265
2600	3771	224.9	4383
2400	3971	243.3	4501
2200	4171	260.7	4597
2000	4371	277.0	4693

Table 3.3 Continued

Distance from the center of the Earth (km)	Distance from the surface of the Earth (km)	Pressure (GPa)	Temperature (K)
1800	4571	292.2	4769
1600	4771	306.2	4846
1400	4971	318.8	4907
1222	5150	328.9	4961
1200	5171	330.1	4965
1000	5371	340.2	5003
800	5571	348.7	5041
600	5771	355.3	5064
400	5971	360.0	5087
200	6171	362.9	5119
0	6371	363.9	5151

Table 3.4. Possible discussion questions for different portions of classroom activity, with important discussion points listed in the right column.

Step	Question	Possible discussion points
Pre-Activity	What is a mineral?	Minerals are materials that meet five requirements. They are: 1) naturally occurring, 2) inorganic, 3) solids, 4) with a definite chemical composition, and 5) an ordered internal structure.
	What is a native mineral?	A mineral composed of a single element
	What happens when solids experience a change in pressures and temperatures from those they formed at?	The solid reorders to a different solid. Bond lengths and geometry of the element(s) change.
Group hypotheses	Discuss with your team which phases of carbon you would expect to form in the Earth (below the surface) based on Figure 2 and the pressures and temperatures listed in Table 3.1 or shown in Figure 3.1?	Figure 3.2b shows the P-T path of the Earth overlain on the phase diagram, which can aid in visualizing the phases of carbon that could be found in Earth.
	Would you expect carbon minerals, graphite or diamond, to form in the inner or outer core?	Use Table 3.2 to discuss the phases present there and whether it would make sense to see any minerals in those layers.
	Which layer(s) of Earth would you expect to find graphite forming in?	Using Figures 3.1 & 3.2 combined with Table 3.1, students should predict surface to the transition zone in the mantle, but most stable in the upper mantle.
	Which layer(s) of Earth would you expect to find diamond forming in?	Using Figures 3.1 & 3.2 combined with Table 3.1, students should predict anywhere in the mantle, but more stable deeper.
Follow up	Do you see any similarities between the molecular model for graphite and the molecular model for diamond?	When you rotate the diamond model around you should see that it also forms hexagons when viewed in 2 dimensions
	Which carbon mineral would you expect to be stronger against outside forces?	If time permits, you can talk about Moh's Hardness Scale and the relative strength of the minerals.
	What are some uses for each carbon mineral? How does their strength relate to their use in that application?	<u>Graphite</u> : <b>Pencil cores ('leads')</b> because it is softer than paper and the hexagons ( <i>graphenes</i> ) will flake off and be left on the paper because the vertical bonds are weak. <b>Lubricants</b> because they can form a thin film and withstand very high temperatures without changing chemically. <u>Diamond</u> : <b>Abrasives</b> such as precision sandpapers and files for polishing because it is one of the strongest materials available. <b>Jewelry</b> because it holds up against the elements and will last for a lifetime even when worn every day.



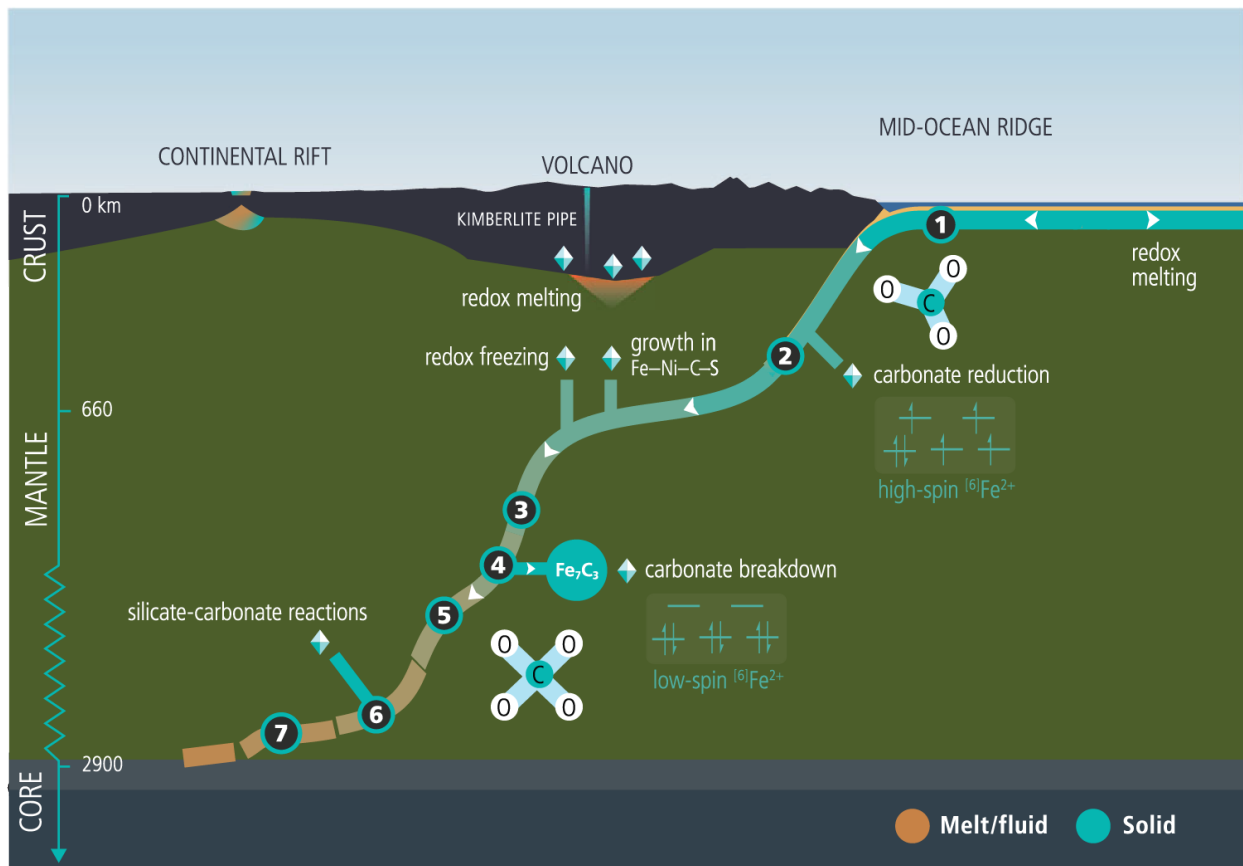


Figure 3.3. Based on figure 4.6 from *Deep Carbon* chapter 4 “Carbon-Bearing Phases throughout Earth’s Interior”, showing simplified distribution and forms of carbon inside the Earth. The thickness of the oceanic crust and subducting slab are vertically exaggerated for clarity in comparison to values in Table 3.3.

the reaction type that occurs in order to crystallize diamonds in those regions (Orcutt et al., 2019).

## **5. Hands On: Molecular Models of Solid Phases of Elemental Carbon**

For the activity portion of this lesson, students work in groups to build molecular models of graphite and diamond to compare the geometries of the molecular structure between the two minerals. Classroom kits distributed through our program to local public libraries contain molecular model sets as outlined in Table 3.5 based on the components from Indigo Instruments (*Indigo Instruments, 2022*). With time constraints in mind, student groups can be directed on constructing models in two different ways: with or without visual instruction prompts shown as Figure 3.4. If students are not provided cues, the goal is to encourage them to think about bond angles and overall geometry of structure, while keeping in mind that minerals are repetitive. It is worth noting that in the diamond structure, the carbon atoms alternate orientation to efficiently form the repetitive structure.

## **6. Lesson Wrap-Up: Same Element, Same Phase, Different Structure**

After students have had time to construct their models, check groups for correct construction if no cues were provided, or completion, before reconvening a class discussion. Thanks to the nature of minerals as repeating patterns, each group's individual model can be compiled into one large whole-class mineral model during the class summary discussion.

Some recommendations for follow-up questions can be found in Table 3.2 if students are unsure of where to begin. Some different classifications of conversations can be visual differences in the two forms of native carbon minerals, how the minerals might react to different things, such as forces and other elements, and how the structure might relate to the industrial applications of the mineral.

For further information on mineral properties, each mineral can be found on [mindat.org](http://mindat.org). If specimens of each mineral are available, discussion on the Moh's hardness scale can be combined with the molecular models. Moh's hardness is a relative (qualitative) scale based on common minerals where 1 is the softest material

Table 3.5. Information on parts per set for group classroom activity based on Indigo Instruments molecular models.

Mineral	Piece	Number of pieces per set	Indigo® Instruments SKU	Indigo® Instruments name
Diamond	Black K atoms	30	68244C	Black Tetrahedral sp <sup>3</sup> Atom
	35 mm bonds	40	68186-35	117 pm Wobbly Bond
Graphite	Black M atoms	26	68259C	Black 5 Prong dsp <sup>3</sup> Atom
	30 mm bonds	30	68186-30	100 pm Wobbly Bond
	50 mm bonds	4	68186-50	167 pm Wobbly Bond

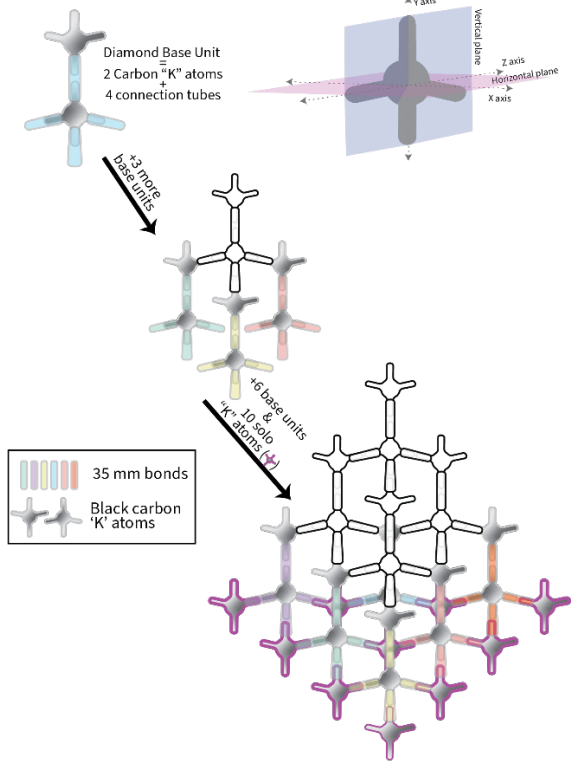
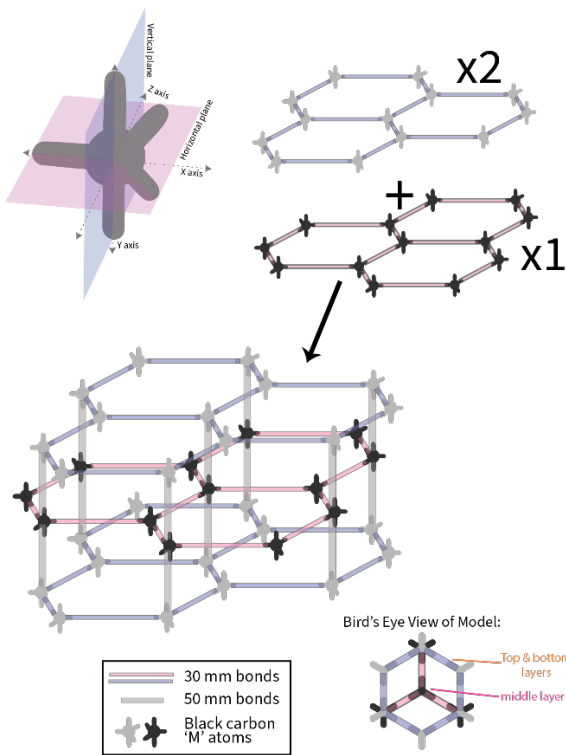


Figure 3.4. Guidance for building atomic structures of graphite (A) and diamond (B) based on materials from indigostruments.com.

and 10 is the hardest. On this scale, graphite has a hardness of 1-2 and diamond has a hardness of 10. Ask students to consider the difference in bond angles and how that might affect the strength of the material. How might the conditions that each is formed in affect the bond angles?

## References

- Bascom, W. (1959). The Mohole. *Scientific American*, 200(4), 41–49.  
<https://doi.org/10.1038/scientificamerican0459-41>
- Carlson, D. H., Plummer, C. C., & Hammersley, L. (2010). *Physical Geology Earth Revealed* (14th ed.). McGraw-Hill.
- Harris, J. W. (1993). The geology of diamond: Time and depth profiles from inclusions. *Diamond and Related Materials*, 2(2–4), 75–79. [https://doi.org/10.1016/0925-9635\(93\)90034-Y](https://doi.org/10.1016/0925-9635(93)90034-Y)
- Herak, D., & Herak, M. (2007). Andrija Mohorovicic (1857-1936)--On the occasion of the 150th anniversary of his birth. *Seismological Research Letters*, 78(6), 671–674.  
<https://doi.org/10.1785/gssrl.78.6.671>
- Indigo Instruments. (2022). [indigo-instruments.com](https://indigo-instruments.com)
- NGSS Lead States. (2017). DCI Arrangements of the Next Generation Science Standards Table of Contents. September, 1–103.
- Orcutt, B. N., Daniel, I., & Dasgupta, R. (Eds.). (2019). *Deep Carbon* (Issue 8.5.2017). Cambridge University Press. <https://doi.org/10.1017/9781108677950>
- Sarafian, E., Gaetani, G. A., Hauri, E. H., & Sarafian, A. R. (2017). Experimental constraints on the damp peridotite solidus and oceanic mantle potential temperature. *Science*, 355(6328), 942–945.  
<https://doi.org/10.1126/science.aaj2165>

## Conclusions

Through natural samples from Earth's oceanic lithosphere and experimental analogs of the Moon, we can model the behavior of rocks at depth to develop four-dimensional models of geologic systems in terrestrial mantles.

Geothermometry and geospeedometry of samples at fast-spreading mid-ocean ridges lends credence to the Sheeted Sill model of crustal accretion, with fast cooling rates calculated near the crust-mantle transition zone that would require deep circulation of cold ocean water, a process incompatible with the Gabbro Glacier model.

Mechanical data and microstructural analysis of experimentally deformed analogs to portions of the lunar mantle suggest that aggregate rheology would be controlled by ilmenite at ratios greater than 25:75 ilm:ol, with more work needed to constrain the transition to olivine dominated between 25:75 and 10:90 ilm:ol. The contrast in material strength with changing volume percentages in the constituent phases needs to be compared to future shear experiments in monomineralic compositions to determine which theoretical aggregate flow law would best explain the system.

Based on state and national standards for science in secondary education settings, lesson plans integrating Earth science concepts can bring the depths of the Earth to the hands of high school students, while relieving the lesson planning burden and needed expertise of classroom educators through partnerships such as the one outlined in Chapter 3.

## Vita

Nadine was born to Dr. James A. Warneke, MD, FACS and Lisa F. Warneke, MS, in Buffalo, NY. At a young age she moved to Tucson, AZ, where she attended primary and secondary school before continuing to her Bachelor of Science at the University of Arizona. While at the University of Arizona, she participated in Tau Beta Sigma – Omega, Pride of Arizona, Honor Choir, Symphonic Band, World Music Gang, and the Society of Earth Sciences Students, finishing with a BS in Geology and a minor in Music. During her time at the University of Arizona, she was a member of the Arizona Accelerator Mass Spectrometry Lab, preparing  $C^{14}$  samples for analysis, then later joined the USGS Water Resources Division, working with Dr. Julio Betancourt on digitizing over 100 years of paleo-rodent midden data to examine climatic changes in the American Southwest. After graduating from UArizona, she began her Master of Science at the University of New Mexico in Albuquerque, working with Dr. Karl Karlstrom on the incisional history of the Eastern Grand Canyon and Vermillion Cliffs using low-temperature AHe thermochronology. After defending her thesis, she worked in the environmental industry on contaminant remediation at Fort Wingate, Gallup, NM, before switching paths to work in K-12 education, teaching in informal settings and managing grant funds for a non-profit childcare program. Her desire to continue with laboratory studies led her to her work at the University of Tennessee where she has combined hands-on research with her interests in teaching and education. After UTK, Nadine plans on accepting a postdoctoral position investigating type-E olivine through Griggs-type deformation experiments.